

---

---

Collisional stability of  
localized metastable ytterbium atoms  
immersed in a Fermi sea of lithium

---

---

by

**Hideki Konishi**



Division of Physics and Astronomy,  
Graduate School of Science, Kyoto University

*A dissertation submitted for the degree of  
Doctor of Science*

JANUARY 2017



# Abstract

An ultracold atomic gas mixture composed of a pair of different species offers attractive research fields such as polar molecules, heteronuclear Efimov trimers, and ultracold chemistry. In particular, a mass-imbalanced atomic mixture in an optical lattice can be a quantum simulator for impurity problems such as Anderson localization, the Kondo effect, and Anderson's orthogonality catastrophe. An ultracold atomic mixture of ytterbium (Yb) and lithium (Li), which has an extreme mass imbalance of about 29, is one of the promising systems to realize an atomic impurity system. Loaded in a suitable optical lattice, Yb atoms are deeply localized in lattice sites while Li atoms remain itinerant over the whole system.

An experimental challenge to realize a quantum simulator for impurity problems using Yb–Li mixtures lies in the control of inter-species collisional properties. Inter-atomic interactions can be tuned by means of Feshbach resonances. However Feshbach resonances between Yb and Li in their respective ground states are theoretically predicted to be too narrow to precisely tune their interactions. Instead, the metastable  $^3P_2$  state of Yb offers an interesting possibility to tune interactions between Yb( $^3P_2$ ) and Li through magnetic Feshbach resonances. To establish an Yb( $^3P_2$ )–Li interaction control method via Feshbach resonances, detailed investigations of their collisional properties are needed.

In this thesis the realization of a system of localized Yb atoms with controllable internal states immersed in a Fermi sea of Li in a three-dimensional optical lattice and the determination of inelastic loss coefficients in collisions between Yb atoms in the metastable excited  $^3P_2$  state and ground state Li atoms are reported. An Yb–Li quantum degenerate mixture loaded in an optical lattice has already been achieved in a previous work. However the produced mixture suffered from a reduced spatial overlap due to their different gravitational sags and we found difficulties in the adiabatic loading of Yb atoms into this optical lattice with a wavelength of 1064 nm. In the present work we first developed a method to compensate for the reduced spatial overlap between Yb and Li atomic clouds. Also we constructed a three-dimensional optical lattice with a

---

wavelength of 532 nm and succeeded in forming an Yb Mott insulator immersed in a Fermi degenerate gas of Li.

Next we studied inelastic collisional properties between Yb( $^3P_2$ ) and ground state Li. By combining a deep optical lattice and a direct excitation from the Yb ground state to the excited  $^3P_2$  state, we achieved high selectivity on the collisional partners and high flexibility in the target state preparation. Using this method we determined inelastic loss coefficients in Yb( $^3P_2$ )-Li collisions in the absence of Feshbach resonances. Absence of spin changing processes at low magnetic fields was confirmed by inelastic loss measurements on the magnetic sublevel of  $m_J = 0$ . We also demonstrated that our method allows us to look into loss processes in few-body systems separately.

# Table of Contents

<b>1</b>	<b>Introduction</b>	<b>1</b>
<b>2</b>	<b>Basics of ultracold atoms</b>	<b>7</b>
2.1	Classical gases . . . . .	7
2.2	Quantum gases . . . . .	8
2.2.1	Bose gases . . . . .	9
2.2.2	Fermi gases . . . . .	10
2.3	Ultracold atoms in an optical lattice . . . . .	11
2.3.1	Bloch bands . . . . .	12
2.3.2	Wannier functions . . . . .	14
2.3.3	Mott shell structure . . . . .	15
2.4	Feshbach resonances . . . . .	17
2.4.1	Resonances in the absence of inelastic scattering . . . . .	17
2.4.2	Resonances in the presence of inelastic scattering . . . . .	18
<b>3</b>	<b>Atomic properties</b>	<b>21</b>
3.1	Lithium . . . . .	21
3.1.1	Energy level structure and optical properties . . . . .	22
3.1.2	Feshbach resonances . . . . .	26
3.2	Ytterbium . . . . .	27
3.2.1	Energy level structure and optical properties . . . . .	27
3.2.2	Collisional properties . . . . .	29
3.3	Yb–Li mixture . . . . .	30
3.3.1	Large mass imbalance . . . . .	30
3.3.2	Collisional properties . . . . .	31
<b>4</b>	<b>Experimental setup</b>	<b>33</b>
4.1	Vacuum system . . . . .	33

TABLE OF CONTENTS

---

4.1.1	Overview of the vacuum apparatus . . . . .	33
4.1.2	Dual species oven . . . . .	34
4.2	Laser systems . . . . .	37
4.3	Gravitational-sag compensation beam . . . . .	40
4.4	Optical lattice . . . . .	41
4.5	Setup for $^3\text{P}_2$ state preparation and detection . . . . .	43
4.5.1	Excitation laser . . . . .	44
4.5.2	Repumping lasers . . . . .	51
4.5.3	Fluorescence imaging . . . . .	52
<b>5</b>	<b>Quantum degenerate mixture of Yb and Li in an optical lattice</b>	<b>55</b>
5.1	Absorption imaging . . . . .	55
5.2	Quantum degenerate Yb–Li mixture . . . . .	58
5.2.1	Zeeman slowing and magneto-optical trapping . . . . .	58
5.2.2	Evaporative and sympathetic cooling . . . . .	60
5.3	Gravitational-sag compensation . . . . .	63
5.4	Optical lattice . . . . .	65
<b>6</b>	<b>Collisional stability of localized Yb(<math>^3\text{P}_2</math>) atoms immersed in a Fermi sea of Li</b>	<b>69</b>
6.1	$^3\text{P}_2$ state preparation and detection . . . . .	69
6.2	Yb( $^3\text{P}_2$ )–Li inelastic collisions . . . . .	73
6.3	Site-occupancy selective loss measurements . . . . .	77
<b>7</b>	<b>Conclusions and outlook</b>	<b>81</b>
<b>A</b>	<b>Optical pumping of <math>^6\text{Li}</math></b>	<b>85</b>
<b>B</b>	<b>Feshbach resonance search</b>	<b>89</b>
B.1	Inelastic loss coefficients . . . . .	89
B.2	Spectroscopy at high magnetic fields . . . . .	91
	<b>Bibliography</b>	<b>95</b>
	<b>Acknowledgements</b>	<b>109</b>

## Introduction

### Studying impurity problems with ultracold atoms

Impurities play crucial roles in condensed-matter physics. The Kondo effect [1], a resistance minimum at a non-zero temperature in a metal, occurs due to magnetic impurities. When impurities act as disorder for waves, Anderson localization [2] takes place. Anderson's orthogonality catastrophe [3] arises when a many-body fermionic system reacts to a sudden perturbation. Experimental studies on these phenomena have been mainly done in solid state systems. However there the number of controllable parameters are limited. Especially the controllability of impurities including their density and interaction strength with conduction electrons is poor. This limits our current understanding of these phenomena. Experiments using other systems that have more flexibility and tunability of experimental parameters, i.e. quantum simulations, will give further insight into the nature of them.

The concept of quantum simulations, to solve a model describing a quantum system that is hard to solve with classical computers by a quantum system with high controllability, was first proposed by R. P. Feynman [4]. Ultracold atoms are a promising system to realize a quantum simulator for quantum many-body physics [5–8] because of simplicity of the system and excellent controllability of the experimental parameters. One of the important techniques in ultracold atomic systems is Feshbach resonances (FRs) [9]. Inter-atomic interactions can be tuned by magnetic fields from non-interacting

to strongly-interacting both attractively and repulsively. This enabled, for example, to observe BCS–BEC crossover [10–12]. Another useful tool is optical lattices, defect-free periodic potentials created by interference of light. An optical lattice dynamically controls atomic mobility and system dimensionality. Also lattice structures can be arbitrarily designed such as triangular [13], honeycomb [14], and Lieb [15] lattices as well as simple cubic lattices [16]. The high degree of controllability and the extreme physical parameter regimes achieved by these techniques offer a unique setting to study quantum many-body systems. Especially a quantum gas in a cubic optical lattice is a quantum simulator for the Hubbard model [17].

Ultracold atomic gases in optical lattices can also provide outstanding opportunities to study impurity problems with excellent controllability. There, even the impurities are introduced in controlled ways. One way is to use optical fields such as incommensurate optical lattices [18, 19] and optical speckles [20, 21]. Anderson localization of matter waves have been observed with these methods [19–21]. Another way is to use atomic impurities [22–26]. Using two different atomic species or spin states and choosing a suitable optical lattice, one can realize a mixture of deeply localized impurity atoms and mobile atoms. This system is considered to be a quantum simulator for the Anderson–Hubbard model with binary disorder [27].

Atomic impurity systems ever experimentally realized are alkali atom pairs or spin pairs of single alkali atoms and there mobile atoms are all bosons. If one wants to address the problems such as the Kondo effect and Anderson’s orthogonality catastrophe with atomic impurity systems, mobile ones should be fermions. Also due to properties of atoms, wavelengths of optical lattices are strongly limited (species-selective or state-selective) particularly spin pair experiments. By choosing a suitable atomic pair, we can realize more flexible and desirable atomic impurity systems.

## Yb–Li mixtures

An ultracold mixture of ytterbium (Yb) and lithium (Li) is one of the promising systems to realize an atomic impurity system. Loaded in an optical lattice, Yb atoms are deeply localized in lattice sites while Li atoms remain itinerant over the whole system because of their extreme mass imbalance  $m_{\text{Yb}}/m_{\text{Li}} \approx 29$ . Since the mobility of Yb and Li atoms in an optical lattice is mostly determined by the large mass imbalance, the system of localized Yb and mobile Li can be realized by any lattices with far-detuned wavelengths. Also both species have selectivity on the bose- and fermi-isotopes. An experimental challenge

---

to study impurity problems with Yb–Li mixtures lies in the control of their collisional properties.

It is theoretically predicted that FRs between Yb and Li in their respective ground states are too narrow to precisely tune the inter-species interaction [28]. On the other hand, the metastable excited  $^3P_2$  state of Yb offers an interesting possibility to control interactions between Yb and Li. FRs between ground and excited  $^3P_2$  state Yb atoms have been observed in several isotopes recently [29, 30], demonstrating the feasibility of working with FRs between different orbitals. In addition to usual mechanisms of FRs as in alkali atoms [9], the observed resonances arise from anisotropy effects in their interactions [31]. In consideration of these recent results, it is reasonable to also expect some useful FRs in the Yb( $^3P_2$ )–Li system.

There is an application to control interactions between mobile atoms and an excited state of impurity atoms. Impurities for Li can be optically switched by the excitation from the Yb ground state to the  $^3P_2$  state, which allows us to address Anderson’s orthogonality catastrophe. The response of the Li Fermi sea against a sudden perturbation by switched localized impurities can be seen by singularity feature on a spectrum (frequency-domain) and a power-law decay of a spin-echo response (time-domain) of the impurity atoms [32]. This problem, as mentioned above, has been studied in solid state systems by frequency-domain measurements [33], but tunability of interaction strengths of impurities is poor and frequency-domain measurements are only available. In contrast atomic impurity systems can investigate this phenomena more quantitatively and systematically and have another observable in frequency-domain. Also this problem is inaccessible with impurity systems realized by optical fields.

The feasibility of Yb( $^3P_2$ )–Li FRs are reported by several theoretical investigations of FRs in  $^{174}\text{Yb}(^3P_2)$ – $^6\text{Li}$  [34] and  $^{171}\text{Yb}(^3P_2)$ – $^6\text{Li}$  systems [35]. The existence of several FRs is predicted. Considering the complexity of the calculations involved, together with uncertainty of the constructed inter-atomic potentials, experimental feedback is indispensable to refine quantitative predictions of resonance positions and inelastic loss rates. On the experimental side, a mixture of  $^{174}\text{Yb}(^3P_2, m_J = -1)$  and  $^6\text{Li}$  was realized at a few  $\mu\text{K}$  [36], and variations of the inelastic loss rate of the  $^{174}\text{Yb}(^3P_2, m_J = -1)$ – $^6\text{Li}$  collisions for 100–520 G were observed, providing in conjunction with theoretical considerations evidence for FRs between them [37]. Further experimental investigations of inelastic collisions at a low temperature regime at other magnetic fields and with other magnetic substates should give further insight into Yb( $^3P_2$ )–Li collisions. Especially, FRs in a  $^{174}\text{Yb}(^3P_2, m_J = -2)$ – $^6\text{Li}$  system are theoretically predicted [38] based on optimized

potentials obtained from the  $m_J = -1$  experimental results. Experimental confirmation of those predictions are as of yet lacking.

In the present thesis, we report on the realization of a system of localized Yb atoms with controllable internal states immersed in a Fermi sea of Li in a three-dimensional optical lattice. We develop a method to compensate for a reduced spatial overlap between ultracold Yb and Li clouds. With help of this we form an Yb Mott insulator immersed in a Fermi degenerate gas of Li. Using this system we investigate inelastic losses in collisions of Yb( $^3P_2$ ) and Li in detail. Performing the experiments in a deep optical lattice and using direct excitation from the Yb ground to the excited  $^3P_2$  state, we achieve high selectivity on the collisional partners and high flexibility in the target state preparation. We also demonstrate that the developed method allows us to look into loss processes of one- or few-atoms in single lattice sites.

## Outline of this thesis

- Chapter 2 provides an overview on the basics of ultracold gases. Theoretical descriptions of ultracold Bose and Fermi gases trapped in harmonic and periodic potentials are presented. Properties of Feshbach resonances in the absence and presence of inelastic scattering are also briefly summarized.
- Chapter 3 presents basic properties of Yb and Li atoms. Especially their optical and scattering properties relevant for the experiments are summarized. Also unique features of Yb–Li mixtures are given.
- Chapter 4 describes our experimental setup. In particular, new components constructed and installed for the present work are detailed.
- Chapter 5 presents the realization of an Yb Mott insulator immersed in a Fermi sea of Li. Production of a quantum degenerate mixture of Yb and Li and compensation for a reduced spatial overlap are described. We show the superfluid to Mott insulator transition of a Bose–Einstein condensate (BEC) of Yb atoms. There, phase coherence properties of an Yb BEC in an optical lattice in the absence and presence of a Fermi gas of Li are compared.
- Chapter 6 reports on the determination of the Yb( $^3P_2$ )–Li inelastic loss coefficient. Measurement of the decay of localized Yb( $^3P_2$ ) atoms by collisions with Li atoms

---

and the evaluation method of the inelastic loss coefficient from the observed decay are explained. It is also shown that this system allows us to investigate loss processes of one- or few-atoms confined in single lattice sites.

- Chapter 7 concludes the present work by giving some final remarks and providing some directions for future studies.



## Basics of ultracold atoms

In this chapter we give basic theoretical descriptions of ultracold atoms. Starting from classical gases governed by classical statistics, properties of the two kinds of quantum gases, Bose and Fermi gases, are reviewed. Treatment of atoms in an optical lattice, i.e. a periodic potential, follows. In the last section, basics of Feshbach resonances in collisions of ultracold atoms are introduced.

### 2.1 Classical gases

In a high-temperature regime where effects of quantum statistics are negligible, the mean occupation number of the single-particle state is given by the Maxwell–Boltzmann distribution,

$$f_{\text{MB}}(\epsilon) = e^{-(\epsilon-\mu)/k_{\text{B}}T}, \quad (2.1)$$

where  $\epsilon$  denotes the energy of the single-particle state,  $\mu$  is the chemical potential, and  $\beta = 1/k_{\text{B}}T$  is the inverse temperature with the Boltzmann constant  $k_{\text{B}}$  and the temperature  $T$ .

Here we consider atoms trapped in a three-dimensional harmonic confinement potential

$$V(\mathbf{r}) = \frac{1}{2}m(\omega_x^2x^2 + \omega_y^2y^2 + \omega_z^2z^2), \quad (2.2)$$

where  $m$  is the atomic mass and  $\omega_x, \omega_y, \omega_z$  are the trap frequencies. The single-particle

energy is quantized as

$$\epsilon = \left(n_x + \frac{1}{2}\right)\hbar\omega_x + \left(n_y + \frac{1}{2}\right)\hbar\omega_y + \left(n_z + \frac{1}{2}\right)\hbar\omega_z, \quad (2.3)$$

where  $n_{x,y,z}$  are non-negative integers and  $\hbar = h/2\pi$  with the Planck constant  $h$ . The occupation of a phase space cell  $\{\mathbf{r}, \mathbf{p}\}$  is given by Eq. (2.1)

$$f_{\text{MB}}(\mathbf{r}, \mathbf{p}) = e^{-(\frac{\mathbf{p}^2}{2m} + V(\mathbf{r}) - \mu)/k_{\text{B}}T}. \quad (2.4)$$

The density distribution of the classical gas is then given by

$$n_{\text{cl}}(\mathbf{r}) = \int \frac{d^3\mathbf{p}}{(2\pi\hbar)^3} f_{\text{MB}}(\mathbf{r}, \mathbf{p}). \quad (2.5)$$

Considering the constraint on the total number of particles

$$N = \int d^3\mathbf{r} n_{\text{cl}}(\mathbf{r}), \quad (2.6)$$

the density distribution Eq. (2.5) is written as a Gaussian distribution

$$n_{\text{cl}}(\mathbf{r}) = \frac{N}{(2\pi)^{3/2}\sigma_x\sigma_y\sigma_z} \exp\left(-\left(\frac{x^2}{2\sigma_x^2} + \frac{y^2}{2\sigma_y^2} + \frac{z^2}{2\sigma_z^2}\right)\right), \quad (2.7)$$

with

$$\sigma_{x,y,z} = \sqrt{\frac{k_{\text{B}}T}{m\omega_{x,y,z}^2}}. \quad (2.8)$$

## 2.2 Quantum gases

In quantum statistics particles are divided into two classes on the basis of the symmetry of the system, bosons and fermions. They obey the Bose–Einstein statistics and the Fermi–Dirac statistics, respectively. Their distribution functions are

$$f(\epsilon) = \frac{1}{\exp((\epsilon - \mu)/k_{\text{B}}T) \mp 1}, \quad (2.9)$$

where the one with the negative sign is the Bose–Einstein distribution and with the positive sign is the Fermi–Dirac distribution. At high temperatures  $k_{\text{B}}T \gg \epsilon - \mu$ , Eq. (2.9) is well approximated by the Maxwell–Boltzmann distribution Eq. (2.1).

In the following, we consider Bose and Fermi gases trapped in a harmonic potential Eq. (2.2). Similarly to the above discussion, the occupation of a phase space cell  $\{\mathbf{r}, \mathbf{p}\}$  is given by

$$f_{\text{B(F)}}(\mathbf{r}, \mathbf{p}) = \frac{1}{\exp((\frac{\mathbf{p}^2}{2m} + V(\mathbf{r}) - \mu)/k_{\text{B}}T) \mp 1}. \quad (2.10)$$

### 2.2.1 Bose gases

Here we first deal with Bose gases. Detailed descriptions can be found in [39, 40]. The density distribution of Bose particles not in the condensate is given by

$$n_{\text{B}}(\mathbf{r}) = \int \frac{d^3\mathbf{p}}{(2\pi\hbar)^3} f_{\text{B}}(\mathbf{r}, \mathbf{p}) = \frac{1}{\lambda_{\text{th}}^3} \text{Li}_{3/2}\left(e^{(\mu-V(\mathbf{r}))/k_{\text{B}}T}\right), \quad (2.11)$$

where  $\lambda_{\text{th}} = \sqrt{\frac{2\pi\hbar^2}{mk_{\text{B}}T}}$  is the thermal de Broglie wavelength and  $\text{Li}_n(z)$  is the polylogarithmic function defined as

$$\text{Li}_n(z) \equiv \frac{1}{\Gamma(n)} \int_0^\infty dx \frac{x^{n-1}}{z^{-1}e^x - 1} = \sum_{k=1}^{\infty} \frac{z^k}{k^n}. \quad (2.12)$$

As the number of condensed bosons grows to be significantly large, the chemical potential  $\mu$  approaches to 0. Therefore the Bose–Einstein phase transition occurs in the center of the trap when the phase space density satisfies

$$\varpi = n_{\text{B}}(0)\lambda_{\text{th}}^3 = \text{Li}_{3/2}(1) = \zeta\left(\frac{3}{2}\right) \approx 2.612, \quad (2.13)$$

where  $\zeta$  is the Riemann zeta function.

In a three-dimensional harmonic trap, the Bose–Einstein condensation (BEC) transition temperature is given by [40]

$$k_{\text{B}}T_{\text{C}} = \hbar\bar{\omega} \left(\frac{N}{\zeta(3)}\right)^{1/3} \approx 0.94\hbar\bar{\omega}N^{1/3} \quad (2.14)$$

where  $\bar{\omega} = (\omega_x\omega_y\omega_z)^{1/3}$  is the geometrical mean of the trap frequencies. For  $T < T_{\text{C}}$  the fraction of the number of particles in the condensate is

$$\frac{N_0}{N} = 1 - \left(\frac{T}{T_{\text{C}}}\right)^3. \quad (2.15)$$

The ground state of a BEC is described by a single order-parameter  $\psi(\mathbf{r})$ . This state and its dynamics are described by the Gross–Pitaevskii equation

$$\left(-\frac{\hbar^2}{2m}\nabla^2 + V(\mathbf{r})\right)\psi(\mathbf{r}) + \tilde{U}|\psi(\mathbf{r})|^2\psi(\mathbf{r}) = \mu\psi(\mathbf{r}), \quad (2.16)$$

where  $\tilde{U} = 4\pi\hbar^2 a/m$  with the  $s$ -wave scattering length  $a$  describing the effect of two-body collisions and  $|\psi(\mathbf{r})|^2$  is the density. When the number of atoms in the condensate is large,

the kinetic energy term in Eq. (2.16) can be neglected (Thomas–Fermi approximation) and therefore the density is given by

$$\begin{aligned} n_c(\mathbf{r}) &= |\psi(\mathbf{r})|^2 = \max\left[\frac{\mu - V(\mathbf{r})}{\tilde{U}}, 0\right] \\ &= \frac{\mu m}{4\pi\hbar^2 a} \max\left[1 - \left(\frac{x^2}{R_x^2} + \frac{y^2}{R_y^2} + \frac{z^2}{R_z^2}\right), 0\right]. \end{aligned} \quad (2.17)$$

The size of the condensate is characterized by the Thomas–Fermi radii

$$R_{x,y,z} = \sqrt{\frac{2\mu}{m\omega_{x,y,z}^2}}. \quad (2.18)$$

From the constraint on the total number of particles  $N = \int d^3\mathbf{r} n_c(\mathbf{r})$ , the chemical potential  $\mu$  is obtained by

$$\mu = \frac{1}{2}(15N\hbar^2 a m^{1/2} \bar{\omega}^3)^{2/5}. \quad (2.19)$$

## 2.2.2 Fermi gases

This section describes trapped Fermi gases. For more details see [41–43]. In the same manner as classical and Bose gases, the density distribution of Fermi particles is given by integrating the Fermi–Dirac distribution Eq. (2.10) over the momentum space

$$n_F(\mathbf{r}) = \int \frac{d^3\mathbf{p}}{(2\pi\hbar)^3} g_s f_F(\mathbf{r}, \mathbf{p}) = -\frac{g_s}{\lambda_{\text{th}}^3} \text{Li}_{3/2}\left(-e^{(\mu - V(\mathbf{r}))/k_B T}\right). \quad (2.20)$$

Here  $g_s$  is the number of spin components of the fermions. The total number of atoms is

$$N = \int d^3\mathbf{r} n_F(\mathbf{r}) = -g_s \left(\frac{k_B T}{\hbar\bar{\omega}}\right)^3 \text{Li}_3(-\mathcal{F}), \quad (2.21)$$

with  $\mathcal{F} = e^{\mu/k_B T}$  as the fugacity.

At  $T = 0$ , the chemical potential  $\mu$  is the energy of the highest occupied state called the Fermi energy  $E_F$  and the Fermi–Dirac distribution becomes a step function  $\theta(E_F - \epsilon)$ . Therefore the density distribution is

$$\begin{aligned} n_F(\mathbf{r}) &= \int \frac{d^3\mathbf{p}}{(2\pi\hbar)^3} g_s \theta\left(E_F - \frac{\mathbf{p}^2}{2m} - V(\mathbf{r})\right) \\ &= g_s \int_{|\mathbf{p}| < \sqrt{2m(E_F - V(\mathbf{r}))}} \frac{d^3\mathbf{p}}{(2\pi\hbar)^3} = \frac{g_s}{6\pi^2} \left(\frac{2m}{\hbar^2}(E_F - V(\mathbf{r}))\right)^{3/2}. \end{aligned} \quad (2.22)$$

The number of fermions  $N$  is

$$N = \int d^3\mathbf{r} n_F(\mathbf{r}) = \frac{g_s}{6} \left(\frac{E_F}{\hbar\bar{\omega}}\right)^3. \quad (2.23)$$

Thus the Fermi energy is obtained by

$$E_F = \hbar\bar{\omega} \left( \frac{6N}{g_s} \right)^{1/3}, \quad (2.24)$$

and equivalently the Fermi temperature  $T_F = E_F/k_B$  is

$$T_F = \frac{\hbar\bar{\omega}}{k_B} \left( \frac{6N}{g_s} \right)^{1/3}. \quad (2.25)$$

Using the Fermi radii defined as

$$R_{F_{x,y,z}} = \sqrt{\frac{2E_F}{m\omega_{x,y,z}^2}}, \quad (2.26)$$

the density distribution Eq. (2.22) can be written as

$$n_F(\mathbf{r}) = \frac{8}{\pi^2} \frac{N}{R_{Fx}R_{Fy}R_{Fz}} \left( \max \left[ 1 - \left( \frac{x^2}{R_{Fx}^2} + \frac{y^2}{R_{Fy}^2} + \frac{z^2}{R_{Fz}^2} \right), 0 \right] \right)^{3/2}. \quad (2.27)$$

By comparing Eqs. (2.21) and (2.23), we obtain a direct relation between the reduced temperature and the fugacity as

$$\frac{T}{T_F} = \left( -\frac{1}{6\text{Li}_3(-\mathcal{F})} \right)^{1/3}. \quad (2.28)$$

## 2.3 Ultracold atoms in an optical lattice

An optical lattice is a periodic potential formed by a standing wave of light. By using a laser far-detuned from atomic resonances, atoms feel an optical dipole force proportional to the optical intensity. The geometry of the intensity pattern created by interference of such a laser light is directly reflected in the geometry of the potential pattern for the atoms.

A standard way to form an optical lattice is to retro-reflect a laser beam. This creates a one-dimensional optical lattice with a periodicity of half a wavelength of the laser  $\lambda/2$ . Three one-dimensional lattices orthogonal to each other create a simple three-dimensional cubic lattice. The total optical lattice potential is

$$V_{\text{lat}}(\mathbf{r}) = V_x \cos^2(kx) + V_y \cos^2(ky) + V_z \cos^2(kz), \quad (2.29)$$

where  $k = 2\pi/\lambda$ . It is convenient to describe a lattice depth  $V_0$  by the reduced lattice depth parameter

$$s = \frac{V_0}{E_R} \quad \text{with} \quad E_R = \frac{\hbar^2 k^2}{2m}. \quad (2.30)$$

Here  $E_R$  is the recoil energy of the lattice laser with the atomic mass  $m$ .

### 2.3.1 Bloch bands

Let us consider a single particle in a one-dimensional periodic potential  $V(x)$  with periodicity  $d = \lambda/2$ . A particle in a periodic potential is described by the Schrödinger equation

$$H\psi_q^{(n)}(x) = E_q^{(n)}\psi_q^{(n)}(x), \quad (2.31)$$

where the Hamiltonian  $H$  is given by

$$H = \frac{\hat{p}^2}{2m} + V(x), \quad (2.32)$$

Here  $n$  and  $q$  denote the energy band index and the quasi-momentum, respectively, and  $\hat{p} = i\hbar \frac{d}{dx}$  is the momentum operator. Values of the quasi-momentum  $q$  are taken within the first Brillouin zone from  $-\hbar k$  to  $\hbar k$ . By Bloch's theorem solutions of Eq. (2.31) can be written as Bloch wave functions, a product of a plane wave  $e^{iqx/\hbar}$  and a function  $u_q^{(n)}(x)$  with the same periodicity as the periodic potential

$$\psi_q^{(n)}(x) = e^{iqx/\hbar} u_q^{(n)}(x). \quad (2.33)$$

Inserting this into Eq. (2.31), we obtain a Schrödinger equation for  $u_q^{(n)}(x)$  as

$$\left( \frac{(\hat{p} + q)^2}{2m} + V(x) \right) u_q^{(n)}(x) = E_q^{(n)} u_q^{(n)}(x). \quad (2.34)$$

Since both the potential  $V(x)$  and the function  $u_q^{(n)}(x)$  are periodic with the same periodicity, they can be written in a form of a Fourier series,

$$V(x) = \sum_l V_l e^{i2klx}, \quad (2.35)$$

$$u_q^{(n)}(x) = \sum_l c_l^{(n,q)} e^{i2klx}. \quad (2.36)$$

The kinetic term in Eq. (2.34) becomes

$$\frac{(\hat{p} + q)^2}{2m} u_q^{(n)} = \sum_l \frac{(2\hbar kl + q)^2}{2m} c_l^{(n,q)} e^{i2klx}, \quad (2.37)$$

and the potential energy term becomes

$$V(x) u_q^{(n)} = \sum_l \sum_{l'} V_l e^{i2kl'x} c_l^{(n,q)} e^{i2klx}. \quad (2.38)$$

The optical lattice potential can be written as

$$V(x) = V_L \cos^2(kx) = \frac{1}{4} V_L (e^{i2kx} + e^{-i2kx}) + \frac{1}{2} V_L. \quad (2.39)$$

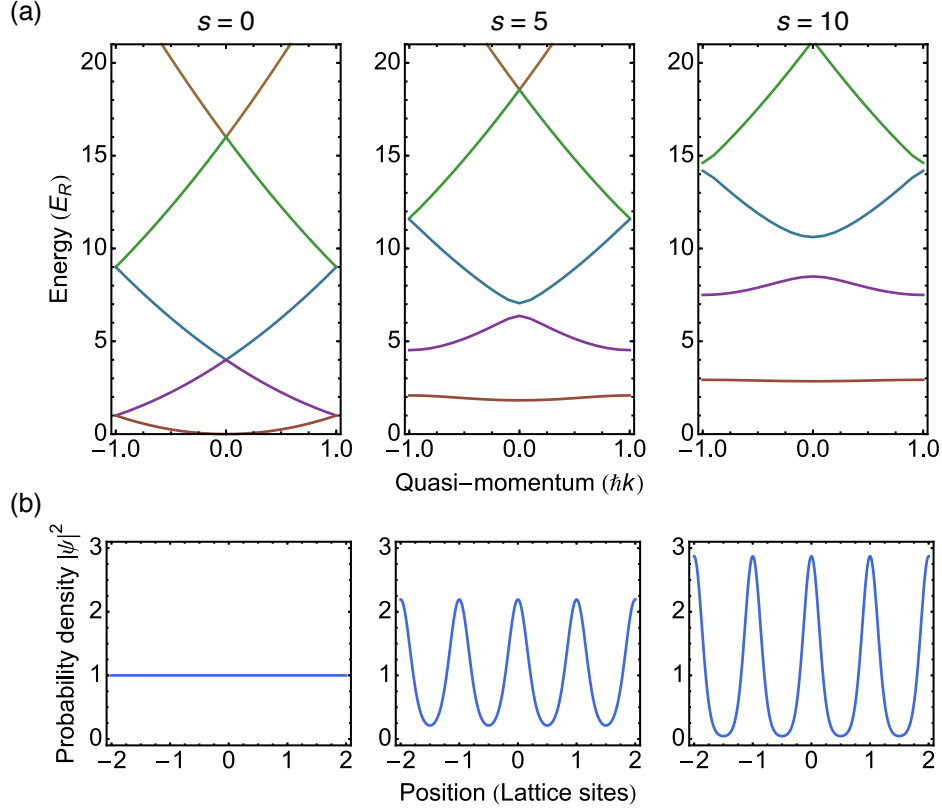


**Figure 2.1.** Energy bands (a) and probability densities for  $q = 0$  in the lowest band (b) for a one-dimensional lattice at lattice depths of  $s = 0, 5, 10$ . In the  $s = 0$  case, the band structure and wave function are equivalent to those of a free-particle. For deeper lattices the band gaps increase and the lowest band becomes flat. Also the probability density in between lattice sites decreases for deeper lattices.

Thus the potential term has as nonzero values only  $V_{-1} = V_1 = V_L/4$  and  $V_0 = V_L/2$ . Using these results we can write the Schrödinger equation (2.34) in matrix form as

$$\sum_l H_{l,l'}^{(q)} c_l^{(n,q)} = E_q^{(n)} c_l^{(n,q)} \quad (2.40)$$

with

$$H_{l,l'}^{(q)} = E_R \times \begin{cases} (2l + q/\hbar k)^2 + s/2 & l = l', \\ s/4 & |l - l'| = 1, \\ 0 & \text{else.} \end{cases} \quad (2.41)$$

Figure 2.1(a) shows the band structures for a one-dimensional lattice for various lattice depths. In the absence of lattice potentials the band structure has no gaps. As the lattice potential increases, the band gaps become larger and the band widths become smaller exponentially. In Fig. 2.1(b) the Bloch states for a one-dimensional lattice for

$q = 0$  in the lowest band for different lattice potential depths are plotted. For deeper lattices the density probability becomes small in between lattice sites.

The Schrödinger equation for a three-dimensional cubic lattice system is fully separable in the three orthogonal directions. Therefore the wave functions and eigenenergies for each axis can be calculated independently and the product of the wave functions and the sum of the eigenenergies of all axes give the wave function and total eigenenergy of the 3D case.

### 2.3.2 Wannier functions

In contrast to Bloch states which are delocalized over the whole system, Wannier functions are localized at lattice sites. The Wannier function for a localized particle in the  $n$ -th energy band is defined by a Fourier transform of the Bloch states:

$$w_n(x - x_i) = \frac{1}{\sqrt{\mathcal{N}}} \sum_q e^{-iqx_i/\hbar} \psi_q^{(n)}(x), \quad (2.42)$$

where  $x_i$  is the lattice index and  $\mathcal{N}$  is a normalization factor. A set of the Wannier functions is an orthonormal system and forms a basis of the Hilbert space.

In Fig. 2.2 densities of the Wannier functions for various lattice depths are shown. For deeper lattice potentials localization of the Wannier state becomes stronger, which corresponds to a smaller tunneling probability.

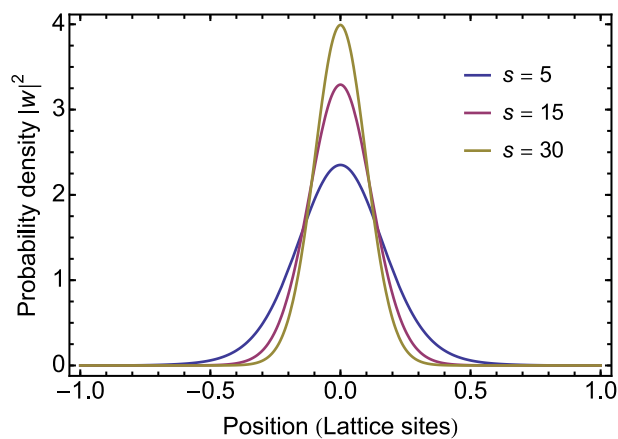


**Figure 2.2.** Probability densities  $|w|^2$  in the lowest band for one-dimensional  $5 E_R$ ,  $15 E_R$ , and  $30 E_R$  deep lattices. As the lattice depth increases, the Wannier state is localized more tightly in a lattice site.

### 2.3.3 Mott shell structure

Bosonic atoms in an optical lattice are well described by the Bose–Hubbard model

$$\hat{H}_{\text{BH}} = -t \sum_{\langle i,j \rangle} \hat{b}_i^\dagger \hat{b}_j + \frac{U}{2} \sum_i \hat{n}_i (\hat{n}_i - 1) + \sum_i (\epsilon_i - \mu) \hat{n}_i, \quad (2.43)$$

where  $\hat{b}_i^\dagger$  ( $\hat{b}_i$ ) is the creation (annihilation) operator,  $\hat{n}_i = \hat{b}_i^\dagger \hat{b}_i$  is the number operator for bosons, and  $\epsilon_i$  is a position-dependent energy offset due to an external confinement. The coefficients  $t$  and  $U$  are the tunneling matrix element and the on-site interaction, respectively, and they are given by [17]

$$t = - \int d^3\mathbf{r} w^*(\mathbf{r} - \mathbf{r}_i) \left( -\frac{\hbar^2}{2m} \nabla^2 + V_{\text{lat}}(\mathbf{r}) \right) w(\mathbf{r} - \mathbf{r}_i), \quad (2.44)$$

$$U = \frac{4\pi\hbar^2 a}{m} \int d^3\mathbf{r} |w(\mathbf{r} - \mathbf{r}_i)|^4, \quad (2.45)$$

with  $a$  as the scattering length. In a deep optical lattice, they can be related to experimental parameters with analytical expressions as [44]

$$\frac{t(s)}{E_{\text{R}}} = \frac{4}{\sqrt{\pi}} s^{3/4} e^{-2\sqrt{s}}, \quad (2.46)$$

$$\frac{U(s)}{E_{\text{R}}} = \sqrt{\frac{8}{\pi}} k_{\text{lat}} a s^{4/3}. \quad (2.47)$$

These expressions, however, deviate from the results obtained by numerical calculations in shallow lattice potentials. It is useful to use another expression accurate within 1% in the range of 8–30  $E_{\text{R}}$  obtained by a fit to numerically calculated curves [45]

$$\frac{t(s)}{E_{\text{R}}} = 1.43s^{0.98} e^{-2.07\sqrt{s}}, \quad (2.48)$$

$$\frac{U(s)}{E_{\text{R}}} = 5.97s^{0.88} \frac{a}{\lambda_{\text{lat}}}. \quad (2.49)$$

When a BEC is loaded in an optical lattice a phase transition from a superfluid state to a Mott-insulator state occurs at a certain lattice depth [16]. By the mean-field approximation the phase transition points satisfies [40]

$$zt \left( \frac{n_c + 1}{n_c U - \mu} + \frac{n_c}{\mu - (n_c - 1)U} \right) = 1, \quad (2.50)$$

where  $z$  is the number of the nearest neighboring sites and  $n_c$  is the maximum number of atoms in a single site. The transition points form Mott lobes as shown in Fig. 2.3. Here

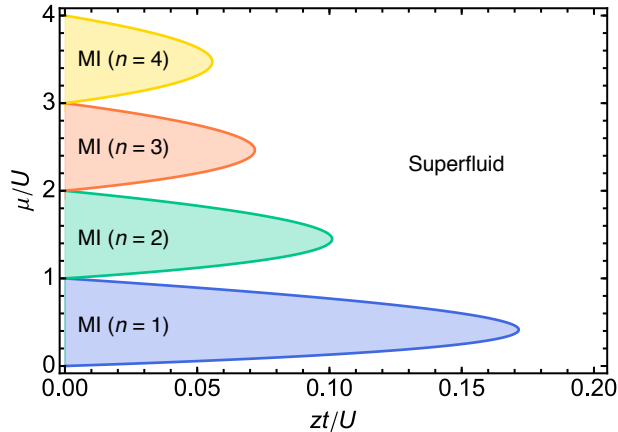


**Figure 2.3.** Phase diagram for the superfluid to Mott-insulator (MI) transition obtained by the mean-field approximation.

we note that the transition point at the tip of the  $n_c = 1$  lobe obtained by quantum Monte Carlo calculations [46] is slightly higher than that obtained by the mean-field approximation.

Since in the experiments an external harmonic confinement Eq. (2.2) is present in addition to the lattice potential Eq. (2.29), the formed Mott-insulator has a spatial shell structure in the occupation number [47, 48]. Here we consider the formation of the Mott shell structure in the atomic limit  $zt/U = 0$ . The lattice sites are decoupled in this limit.

The energy of a state in a site with the occupation number  $n$  is given by

$$E_n = -\tilde{\mu}n + \frac{U}{2}(n^2 - n), \quad (2.51)$$

where  $\tilde{\mu}$  is an effective local chemical potential

$$\tilde{\mu} = \mu - V(\mathbf{r}). \quad (2.52)$$

The occupation number that minimizes the energy  $E_n$  is determined by

$$\frac{\partial E_n}{\partial n} = -\tilde{\mu} + \frac{U}{2}(2n - 1) = 0. \quad (2.53)$$

Since  $n$  takes only integer values, the minimization condition becomes

$$n - 1 < \frac{\tilde{\mu}}{U} < n. \quad (2.54)$$

As our confinement is a harmonic one,  $V(\mathbf{r}) = \frac{1}{2}m(\omega_x^2 x^2 + \omega_y^2 y^2 + \omega_z^2 z^2)$ , the effective chemical potential is maximum at the center where  $V(0) = 0$ . Thus the maximum occupation number  $n_{\max}$  satisfies

$$n_{\max} - 1 < \frac{\mu}{U} < n_{\max}. \quad (2.55)$$

The boundary of the shells with  $n$  and  $n + 1$  occupations for each direction is given by

$$R_{x,y,z}^{(n)} = \left( \frac{2(\mu - nU)}{m\omega_{x,y,z}^2} \right)^{1/2}. \quad (2.56)$$

Therefore the Mott shell with the occupation number  $n$  lies in the area between two ellipsoids with radii  $R_{x,y,z}^{(n)}$  and  $R_{x,y,z}^{(n-1)}$ , and the shell with  $n_{\max}$  lies in an ellipsoid with radii  $R_{x,y,z}^{(n_{\max}-1)}$ . The number of sites of the occupation number  $n$  is then given by

$$S_n = \begin{cases} \frac{4\pi}{3d^3} (R_x^{(n-1)} R_y^{(n-1)} R_z^{(n-1)} - R_x^{(n)} R_y^{(n)} R_z^{(n)}) & \text{for } n < n_{\max}, \\ \frac{4\pi}{3d^3} R_x^{(n-1)} R_y^{(n-1)} R_z^{(n-1)} & \text{for } n = n_{\max}, \end{cases} \quad (2.57)$$

with  $d$  as the lattice spacing.

## 2.4 Feshbach resonances

Collisions of ultracold atoms are characterized by  $s$ -wave scattering lengths. Feshbach resonances make it possible to tune  $s$ -wave scattering lengths, i.e. inter-atomic interactions magnetically or optically [9, 49]. In this section we give properties of magnetic Feshbach resonances in the absence and presence of inelastic scattering.

### 2.4.1 Resonances in the absence of inelastic scattering

In a two-body scattering process of two atoms with a reduced mass  $m_{\text{red}}$  at ultracold temperatures where higher-order partial waves with angular momenta  $l > 0$  are suppressed, the  $s$ -wave scattering length  $a$  is defined by

$$a(k) = -\frac{\tan \delta(k)}{k}, \quad (2.58)$$

where  $\delta(k)$  is the phase shift with the wave vector  $k$  defined by the kinetic energy  $E_{\text{kin}} = \hbar^2 k^2 / 2m_{\text{red}}$ . The elastic cross-section is given by

$$\sigma(k) = g \frac{4\pi a^2}{1 + k^2 a^2}, \quad (2.59)$$

where the factor  $g = 1$  for non-identical atoms and  $g = 2$  for identical bosons.

A Feshbach resonance is well described by the two-channel model [49], in which the bound state and the continuum are each represented by one scattering channel. The  $s$ -wave scattering length  $a$  varies as a function of the magnetic field  $B$

$$a(B) = a_{\text{bg}} \left( 1 - \frac{\Delta}{B - B_0} \right), \quad (2.60)$$

where the background scattering length  $a_{\text{bg}}$  represents the off-resonant value,  $B_0$  denotes the resonance position, and  $\Delta$  is the resonance width. Therefore the cross-section Eq. (5.5) shows a sharp peak with a height of  $4\pi g/k^2$  at the resonance.

### 2.4.2 Resonances in the presence of inelastic scattering

In the presence of inelastic collisions, the scattering properties can be expressed by a complex  $s$ -wave scattering length [50, 51]

$$\tilde{a} = a - ib, \quad (2.61)$$

where  $a$  and  $b$  are real. In analogy with Eq. (2.58), it is defined by

$$\tilde{a}(k_0) = -\frac{\tan \delta_0(k_0)}{k_0}, \quad (2.62)$$

where  $\delta_0$  is the complex phase shift with a positive imaginary part and  $k_0$  is the wave vector of the entrance channel. Using the complex scattering length, the elastic and inelastic cross-sections are given by [52]

$$\sigma_{\text{el}}(k_0) = g \frac{4\pi |\tilde{a}|^2}{1 + k_0^2 |\tilde{a}|^2 + 2k_0 b} \quad (2.63)$$

and

$$\sigma_{\text{in}}(k_0) = g \frac{4\pi b}{k_0(1 + k_0^2 |\tilde{a}|^2 + 2k_0 b)}. \quad (2.64)$$

In the limit of  $k_0 \rightarrow 0$ , the elastic cross-section becomes

$$\sigma_{\text{el}} = 4\pi g(a^2 + b^2) \quad (2.65)$$

The inelastic loss coefficient  $K_{\text{in}}$  is obtained by multiplying the inelastic cross-section Eq. (2.64) by the relative collision velocity  $v = \hbar k/m_{\text{red}}$ . This results in [9]

$$K_{\text{in}} = \frac{2\hbar}{m_{\text{red}}} gb. \quad (2.66)$$

The complex scattering length  $\tilde{a}$  is given by

$$a(B) = a_{\text{bg}} - a_{\text{res}} \frac{\gamma(B - B_0)}{(B - B_0)^2 + (\gamma/2)^2}, \quad (2.67)$$

$$b(B) = 2a_{\text{res}} \frac{(\gamma/2)^2}{(B - B_0)^2 + (\gamma/2)^2}. \quad (2.68)$$

Here  $\gamma$  is the decay rate for the decay of the bound state into all available loss channels in magnetic field units. The resonance length parameter  $a_{\text{res}}$  is related to the resonance width  $\Delta$  by

$$a_{\text{res}} = a_{\text{bg}} \frac{\Delta}{\gamma}. \quad (2.69)$$

This gives an indication of the possible control of the scattering length as the real part  $a$  can vary within the range  $a_{\text{bg}} \pm a_{\text{res}}$ . A common figure of merit for the coherent control of the atoms is the ratio  $a/b$ . For  $|B - B_0| \gg \gamma$  and a change in scattering length much larger than  $a_{\text{bg}}$ , this can be shown from Eqs. (2.67) and (2.68) to be

$$\frac{a}{b} \approx -2 \frac{(B - B_0)}{\gamma} \approx 2 \frac{a_{\text{res}}}{a}. \quad (2.70)$$

Therefore a larger  $a_{\text{res}}$  gives better coherent control and smaller inelastic losses for a given change in scattering length. From Eqs. (2.66) and (2.70), the inelastic loss coefficient can be written as

$$K_{\text{in}} \approx g \frac{h}{m_{\text{red}}} \frac{a^2}{a_{\text{res}}}. \quad (2.71)$$

Thus in the presence of inelastic scattering, a Feshbach resonance is accompanied by an increase of the inelastic loss coefficient by the square of the change in scattering length.



## Atomic properties

Since the first realization of a Bose–Einstein condensation (BEC) of a dilute atomic gas of  $^{87}\text{Rb}$  in 1995 [53], various species have been cooled down to BEC or Fermi degenerate regime. Each species has different features, which enables us to perform a variety of experiments with different species.

In this chapter basic properties and features of lithium and ytterbium used in this work are described. Especially their energy level structures and collisional properties are introduced. Unique features of mixtures of Yb and Li are also summarized.

### 3.1 Lithium

Lithium (Li) is the lightest alkali metal atom with two naturally occurring stable isotopes, fermionic  $^6\text{Li}$  and bosonic  $^7\text{Li}$ . A BEC of  $^7\text{Li}$  and Fermi degeneracy of  $^6\text{Li}$  were first realized in 1995 [54] and in 2001 [55], respectively. The existence of  $^6\text{Li}$  is invaluable because it is the only fermionic stable isotope in the alkali metal group apart from  $^{40}\text{K}$  and it has a broad Feshbach resonance. This motivated cold atom researchers to work with  $^6\text{Li}$  and indeed many landmark studies have been achieved with ultracold Li atoms: realization of a molecular BEC [56], observation of BCS–BEC crossover [11, 12], investigation on a unitary Fermi gas [57–59], a Bose–Fermi superfluid mixture [60], realization of an antiferromagnetic order [61, 62], and realization of fermionic quantum gas microscopes [63, 64]. In this work we also use  $^6\text{Li}$ . This section describes the energy

level structure and optical properties of  ${}^6\text{Li}$  relevant for laser cooling and trapping and its Feshbach resonances.

### 3.1.1 Energy level structure and optical properties

Electron configurations of the ground and first excited states of  ${}^6\text{Li}$  are  $1s^22s^1$  and  $1s^22p^1$ , respectively. Like for all alkali atoms, the spectrum line connecting these states is called the  $D$ -line for historical reasons. Figure 3.1 shows the energy level structure of the ground and first excited states of  ${}^6\text{Li}$ . The  $D$ -line splits into two, called the  $D_1$  (the lower one) and  $D_2$  lines, due to a fine-structure splitting in the excited  ${}^2\text{P}$  state ( ${}^2\text{P}_{1/2}$  and  ${}^2\text{P}_{3/2}$  states) by the spin-orbit coupling [65]. The two states are about 10 GHz apart [66]. Optical properties of the  $D_1$  and  $D_2$  lines are listed in Table 3.1.

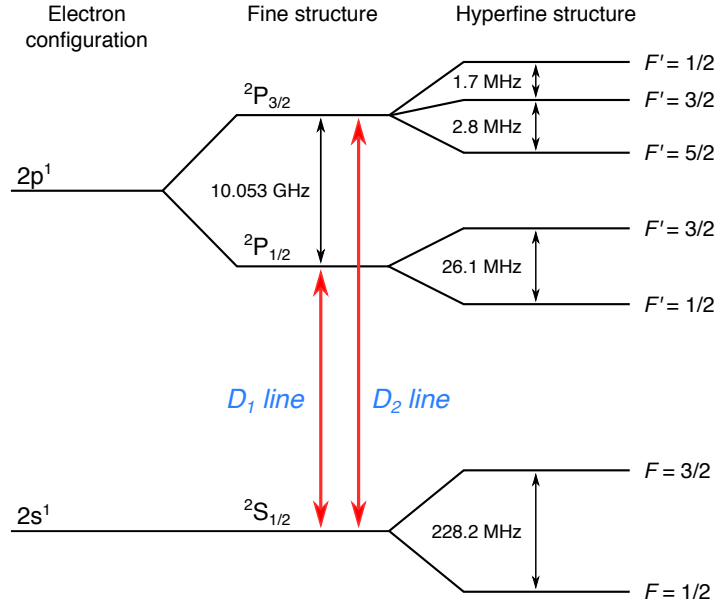


**Figure 3.1.** Energy level structure of  ${}^6\text{Li}$ . From left to right, the electron configuration, the hyperfine structure, and the hyperfine structure are involved.

The ground and excited levels have hyperfine structures due to the interactions between the magnetic field generated by the electrons and the magnetic dipole moment of the nuclear spin  $\mathbf{I}$ . The hyperfine structure of an atom is usually defined over the  $\{J, I, F, m_F\}$  eigenstates, where  $F$  is the quantum number of the total angular momentum  $\mathbf{F} = \mathbf{I} + \mathbf{J}$ . The hyperfine energy is given by

$$E_{\text{hfs}} = \frac{1}{2}hAK + hB \frac{3K(K+1) - 4I(I+1)J(J+1)}{8I(2I-1)J(2J-1)}, \quad (3.1)$$

**Table 3.1.** Optical properties of the  $D_1$  ( ${}^2S_{1/2} \leftrightarrow {}^2P_{1/2}$ ) and  $D_2$  ( ${}^2S_{1/2} \leftrightarrow {}^2P_{3/2}$ ) lines of  ${}^6\text{Li}$  [66, 67]. Here we note that though the lifetimes and equivalently linewidths and Doppler cooling limits for the both lines are identical, this is not typical in the alkalis.

Transition	Wavelength $\lambda$ (nm)	Lifetime $\tau$ (ns)	Linewidth $\Gamma/2\pi$ (MHz)	Doppler cooling limit $T_D$ ( $\mu\text{K}$ )
$D_1$ line	670.9925	27.1	5.87	141
$D_2$ line	670.9774	27.1	5.87	141

where  $K = F(F + 1) - I(I + 1) - J(J + 1)$ . The hyperfine constants  $A$  and  $B$  for the  ${}^2S_{1/2}$ ,  ${}^2P_{1/2}$ , and  ${}^2P_{3/2}$  states are listed in Table 3.2. The resulting splittings are shown rightmost in Fig. 3.1. As long as  $J$  is considered as a good quantum number, the hyperfine interaction Hamiltonian is written as

$$H_{\text{hfs}} = hA\mathbf{I} \cdot \mathbf{J} + hB \frac{6(\mathbf{I} \cdot \mathbf{J})^2 + 3(\mathbf{I} \cdot \mathbf{J})}{2I(2I - 1)2J(2J - 1)}. \quad (3.2)$$

**Table 3.2.** Hyperfine constants for the  ${}^2S$  and  ${}^2P$  levels [68].

Symbol	State	Value (MHz)
$A$	${}^2S_{1/2}$	152.136 840 7
	${}^2P_{1/2}$	17.375
	${}^2P_{3/2}$	-1.155
$B$	${}^2P_{3/2}$	-0.10

### Zeeman effect

An applied magnetic field lifts the degeneracy of the magnetic sublevels of a state due to the Zeeman effect. The Zeeman effect Hamiltonian is given by

$$H_{\text{ZE}} = g_J\mu_B\mathbf{J} \cdot \mathbf{B} + g_I\mu_B\mathbf{I} \cdot \mathbf{B}, \quad (3.3)$$

where  $\mu_B = h \times 1.40 \text{ MHz/G}$  is the Bohr magneton and  $g_J$  and  $g_I$  are the total electronic and nuclear spin  $g$ -factors, respectively. Values of  $g_J$  and  $g_I$  are given in Table 3.3. Total energy shifts of the hyperfine and Zeeman effects in an external magnetic field are obtained by diagonalizing the total Hamiltonian

$$H_{\text{total}} = H_{\text{hfs}} + H_{\text{ZE}}. \quad (3.4)$$

**Table 3.3.** Total nuclear and total electronic  $g$ -factors for  ${}^6\text{Li}$  [68].

Symbol	Value
$g_I$	$-0.000\,447\,654\,0$
$g_J({}^2\text{S}_{1/2})$	$2.002\,301\,0$
$g_J({}^2\text{P}_{1/2})$	$0.666\,8$
$g_J({}^2\text{P}_{3/2})$	$1.335$

The magnetic field dependence of the hyperfine Zeeman sublevels of the  ${}^2\text{S}_{1/2}$ ,  ${}^2\text{P}_{1/2}$ , and  ${}^2\text{P}_{3/2}$  states are presented in Figs. 3.2 and 3.3.

In a high field region where the Paschen-Back effect occurs,  $m_J$ , the projection of the total electronic spin  $J$ , and  $m_I$ , the projection of the nuclear spin  $I$ , are considered as good quantum numbers. Hence eigenstates of an atom are labeled by  $|m_J, m_I\rangle$ . The total energy of an eigenstate  $|m_J, m_I\rangle$  in a magnetic field  $B$  is given by

$$E_{m_J, m_I} = hAm_Jm_I + g_J\mu_B m_J B + g_I\mu_B m_I B. \quad (3.5)$$

In the Paschen-Back regime the second term dominates the energy shift as  $g_J \gg g_I$ . Therefore the energy levels of the  ${}^2\text{S}_{1/2}$  state splits into two manifolds,  $m_J = m_S = \pm 1/2$ . Similarly, those of the  ${}^2\text{P}_{1/2}$  and  ${}^2\text{P}_{3/2}$  states split into two ( $m_J = \pm 1/2$ ) and four ( $m_J = \pm 1/2, \pm 3/2$ ) manifolds, respectively. The first term in Eq. (3.5) gives a splitting

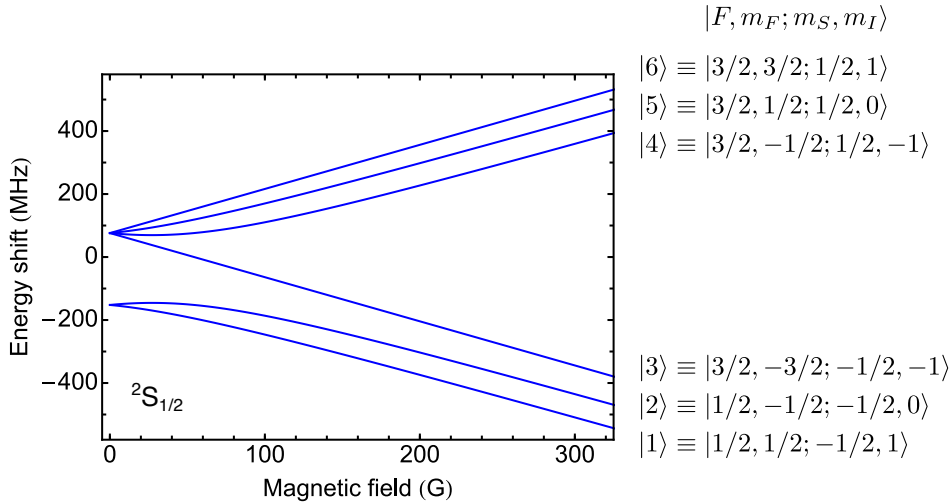


**Figure 3.2.** Magnetic field dependence of the hyperfine Zeeman sublevels of the ground state of  ${}^6\text{Li}$ . For convenience the eigenstates of the ground state are conventionally labeled as  $|1\rangle \cdots |6\rangle$  as in Eq. (3.6).

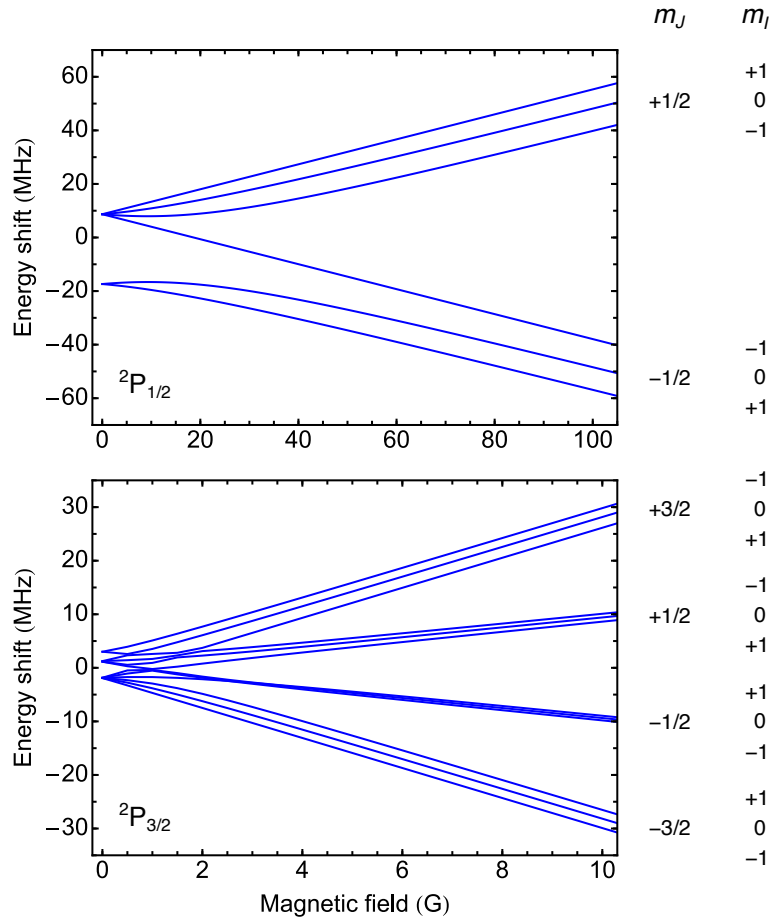


**Figure 3.3.** Magnetic field dependence of the hyperfine Zeeman sublevels of the  ${}^2P_{1/2}$  (upper panel) and  ${}^2P_{3/2}$  (lower panel) states of  ${}^6\text{Li}$ .

of each manifold into three as  $m_I$  takes either  $-1, 0$ , or  $+1$ .

The eigenstates of the ground state are conventionally labelled as  $|1\rangle \cdots |6\rangle$  starting from the lowest state:

$$\begin{aligned}
 |1\rangle &\equiv |F = 1/2, m_F = 1/2; m_S = -1/2, m_I = 1\rangle, \\
 |2\rangle &\equiv |F = 1/2, m_F = -1/2; m_S = -1/2, m_I = 0\rangle, \\
 |3\rangle &\equiv |F = 3/2, m_F = -3/2; m_S = -1/2, m_I = -1\rangle, \\
 |4\rangle &\equiv |F = 3/2, m_F = -1/2; m_S = 1/2, m_I = -1\rangle, \\
 |5\rangle &\equiv |F = 3/2, m_F = 1/2; m_S = 1/2, m_I = 0\rangle, \\
 |6\rangle &\equiv |F = 3/2, m_F = 3/2; m_S = 1/2, m_I = 1\rangle.
 \end{aligned} \tag{3.6}$$

We follow these notations in this thesis.

### 3.1.2 Feshbach resonances

Feshbach resonances in collisions of  ${}^6\text{Li}$  have been well studied both experimentally and theoretically. Figure 3.4 shows variations of scattering lengths between the lowest three states over a wide range of magnetic fields. They are obtained by coupled-channel calculations using binding energies measured by precise rf spectroscopy [69]. The scattering lengths in the  $|1\rangle\text{--}|2\rangle$ ,  $|1\rangle\text{--}|3\rangle$ , and  $|2\rangle\text{--}|3\rangle$  collisions diverge at 834 G, 690 G, and 811 G, respectively, indicating Feshbach resonances. The parameters of the FRs are given in Table 3.4. In addition to the broad resonances, there is a narrow resonance in the  $|1\rangle\text{--}|2\rangle$  collisions at 543 G [70].

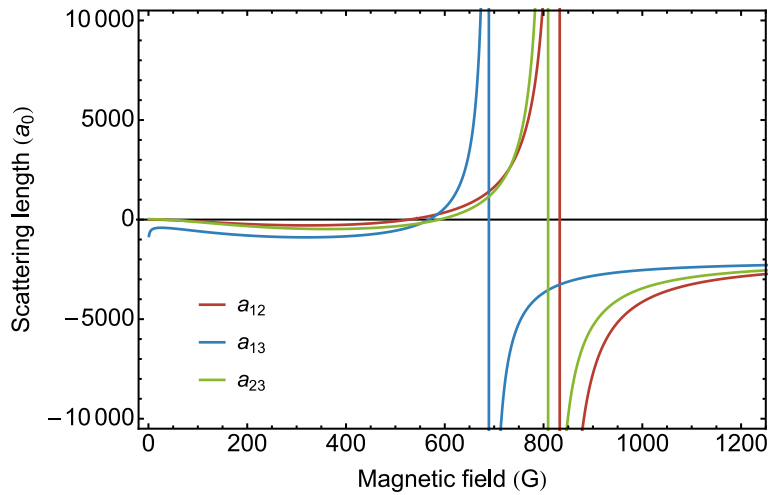


**Figure 3.4.** Inter-spin-state scattering lengths in units of the Bohr radius  $a_0$  over a wide range of magnetic fields. Divergencies of  $a_{12}$ ,  $a_{13}$ , and  $a_{23}$  are found at 834 G, 690 G, and 811 G, respectively, indicating Feshbach resonance locations. The figure is reproduced from the data provided in [69].

**Table 3.4.**  ${}^6\text{Li}$  Feshbach resonances between the three lowest spin states. In addition to a broad FR at 834 G there is a narrow resonance at 543 G in the  $|1\rangle\text{--}|2\rangle$  collisions. The values are taken from [9]

Channel	$B_0$ (G)	$\Delta$ (G)	$a_{\text{bg}}$ ( $a_0$ )
$ 1\rangle\text{--} 2\rangle$	834.1	-300	-1405
$ 1\rangle\text{--} 3\rangle$	690.4	-122.3	-1727
$ 2\rangle\text{--} 3\rangle$	811.2	-222.3	-1490
$ 1\rangle\text{--} 2\rangle$	543.25	0.1	60

## 3.2 Ytterbium

Ytterbium (Yb) is the fourteenth and the second to the last element in the lanthanide series. An important feature of Yb is the richness of its stable isotopes. It has five bosonic ( $^{168}\text{Yb}$ ,  $^{170}\text{Yb}$ ,  $^{172}\text{Yb}$ ,  $^{174}\text{Yb}$ ,  $^{176}\text{Yb}$ ) and two fermionic ( $^{171}\text{Yb}$ ,  $^{173}\text{Yb}$ ) isotopes, with  $^{174}\text{Yb}$  being the most abundant one (31.8% natural abundance). Quantum degeneracies of all isotopes except  $^{172}\text{Yb}$  have already been realized [71–76]. Thanks to this feature not only single bosonic or fermionic systems but also Bose–Bose, Bose–Fermi, and Fermi–Fermi mixtures can be realized at will [76, 77].

Another key feature is the existence of metastable  $^3\text{P}_2$  and  $^3\text{P}_0$  states. High-resolution spectroscopy using these states is an excellent probe for many-body systems in optical lattices [78, 79]. Also new kinds of Feshbach resonances between the ground and metastable states were observed recently [29, 30, 80–82].

This section describes basic properties of Yb. In addition to its energy level structure and ground state collisional properties, we focus on the metastable  $^3\text{P}_2$  state, which plays a crucial role in this work.

### 3.2.1 Energy level structure and optical properties

The ground state electron configuration of Yb is  $[\text{Xe}]4f^{14}6s^2$ . Since Yb has two valence electrons, its energy levels are classified into singlet and triplet series, similar to alkaline-earth (group II) atoms. Figure 3.5 shows the energy level structure of Yb relevant for our experiments.

The  $^1\text{S}_0 \rightarrow ^1\text{P}_1$  transition is an electric dipole (E1) transition with a natural linewidth of 29 MHz. This strong transition (399 nm) is suitable for Zeeman slowing and imaging of Yb atoms which require a high photon scattering rate. In contrast, the intercombination ( $^1\text{S}_0 \rightarrow ^3\text{P}$ ) lines are much weaker transitions. The  $^1\text{S}_0 \rightarrow ^3\text{P}_1$  transition has a linewidth of 182 kHz, with which one can achieve laser cooling down to the regime of a few  $\mu\text{K}$ . Optical properties of these two transitions relevant for laser cooling of Yb are summarized in Table 3.5.

The  $^1\text{S}_0 \rightarrow ^3\text{P}_0$  and  $^1\text{S}_0 \rightarrow ^3\text{P}_2$  transitions have much narrower linewidths of  $\approx 10$  mHz. These lines enable us to do what cannot be done with alkali atoms that are often used in cold atom experiments. The former, called clock transition, is one of the promising candidates for the next generation frequency standard [85]. High-resolution spectroscopy via the latter transition has been proven to be a powerful probe tool on

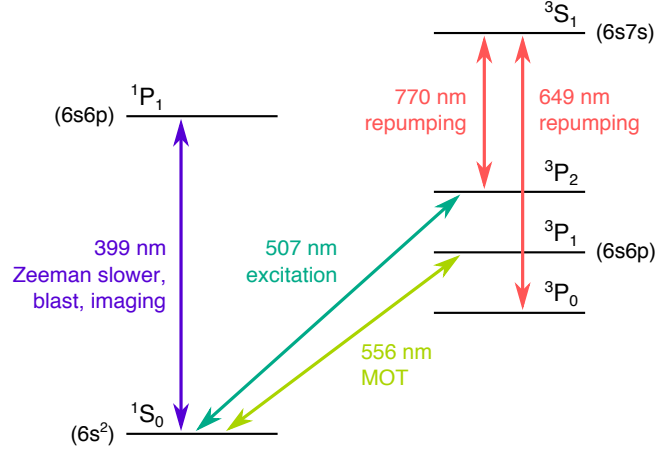


**Figure 3.5.** Energy levels of Yb relevant for our experiments shown with their transition wavelengths and applications. A strong  $^1S_0 \rightarrow ^1P_1$  transition (399 nm) is used for Zeeman slowing, blast, and absorption and fluorescence imaging. A narrow  $^1S_0 \rightarrow ^3P_1$  line (556 nm) is utilized for MOT. Metastable  $^3P_2$  state atoms are prepared by direct excitation from the ground  $^1S_0$  state (507 nm). The excited atoms are repumped into the ground state through a  $^3S_1 \rightarrow ^3P_1 \rightarrow ^1S_0$  process by simultaneous applications of  $^3P_2 \rightarrow ^3S_1$  (770 nm) and  $^3P_0 \rightarrow ^3S_1$  (649 nm) resonant lights before detection.

**Table 3.5.** Optical properties of transitions relevant for laser cooling of Yb [83, 84].

Transition	Wavelength $\lambda$ (nm)	Lifetime $\tau$ (ns)	Linewidth $\Gamma/2\pi$ (MHz)	Doppler cooling limit $T_D$ ( $\mu$ K)
$^1S_0 \leftrightarrow ^1P_1$	398.9	5.5	29	690
$^1S_0 \leftrightarrow ^3P_1$	555.8	875	0.182	4.4

ultracold Yb atoms [78, 86], which also plays an important role in this work. Table 3.6 gives optical properties of the  $^1S_0 \rightarrow ^3P_2$  transition.

**Table 3.6.** Optical properties of the  $^1S_0 \rightarrow ^3P_2$  transition.

Isotope	Wavelength $\lambda$ (nm)	Lifetime $\tau$ (s)	Linewidth $\Gamma/2\pi$ (mHz)
Bosons		15	10.6
$^{171}\text{Yb}$	507.35	6.3	25
$^{173}\text{Yb}$		7.2	22

### Zeeman effect

Bosonic Yb isotopes have no hyperfine structures in their energy levels because of the absence of nuclear spins. Therefore the Zeeman energy shift of a bosonic Yb atom is given by

$$\Delta E_{ZE} = g_J \mu_B m_J B. \quad (3.7)$$

Here the total electronic spin  $g$ -factor  $g_J$  is given by a Lendé  $g$ -factor expression that combines  $g$ -factors for the electron orbital  $g_L$  and for the electron spin  $g_S$

$$g_J = g_L \frac{J(J+1) - S(S+1) + L(L+1)}{2J(J+1)} + g_S \frac{J(J+1) + S(S+1) - L(L+1)}{2J(J+1)}. \quad (3.8)$$

The values of the  $g$ -factors are  $g_L = 1$  and  $g_S \approx 2$ , respectively, which simplifies Eq. (3.8) to

$$g_J \approx \frac{3}{2} + \frac{S(S+1) - L(L+1)}{2J(J+1)}. \quad (3.9)$$

The  $^3P_2$  state has five Zeeman sublevels as  $J = 2$  while the  $^1S_0$  state has no Zeeman shifts. The  $g$ -factor for the  $^3P_2$  state is  $g_J = 3/2$ . Hence an applied magnetic field lifts degeneracy of neighboring  $m_J$  sublevels by  $h \times 2.1$  MHz/G.

## 3.2.2 Collisional properties

### Ground state collisions

Ground state Yb atoms have no magnetic Feshbach resonances because of the absence of electronic spins. Instead, we can choose a variety of scattering lengths by using various pairs of isotopes. The  $s$ -wave scattering lengths between all combinations of the seven isotopes of Yb have been precisely determined by two-color photoassociation spectroscopy and the mass-scaling law [87]. The values are listed in Table 3.7.

Another way to tune the inter-atomic interaction is via an optical Feshbach resonance in the intercombination  $^1S_0 \rightarrow ^3P_1$  transition as proposed in [88]. In fact some resonances have been experimentally observed [89–91]. However, they are far from a practical use suffering from atomic loss due to photoassociation near the resonance.

### Metastable $^3P_2$ state

The metastable  $^3P_2$  state has a long lifetime of  $\approx 10$  s. However inelastic collision rates in Yb( $^3P_2$ )–Yb( $^3P_2$ ) and Yb( $^3P_2$ )–Yb( $^1S_0$ ) collisions are rather high on the order of  $10^{-12}$ – $10^{-11}$  cm<sup>3</sup>/s [92, 93], which means the  $^3P_2$  atoms are immediately de-excited and

**Table 3.7.** *S*-wave scattering lengths in nm for all combinations of the Yb isotopes [87].

	$^{168}\text{Yb}$	$^{170}\text{Yb}$	$^{171}\text{Yb}$	$^{172}\text{Yb}$	$^{173}\text{Yb}$	$^{174}\text{Yb}$	$^{176}\text{Yb}$
$^{168}\text{Yb}$	13.33	6.19	4.72	3.44	2.04	0.13	-19.0
$^{170}\text{Yb}$		3.38	1.93	-0.11	-4.30	-27.4	11.08
$^{171}\text{Yb}$			-0.15	-4.46	-30.6	22.7	7.49
$^{172}\text{Yb}$				-31.7	22.1	10.61	5.62
$^{173}\text{Yb}$					10.55	7.34	4.22
$^{174}\text{Yb}$						5.55	2.88
$^{176}\text{Yb}$							-1.28

escaped from a trap in a bulk sample. An optical lattice can isolate individual  $^3\text{P}_2$  atoms from the others and suppress their inelastic collisions.

Feshbach resonances between the  $^3\text{P}_2$  and  $^1\text{S}_0$  states have been observed with  $^{174}\text{Yb}$ ,  $^{173}\text{Yb}$ , and  $^{171}\text{Yb}$  isotopes [29, 30]. In addition to usual mechanisms of FRs as in alkali atoms [9], the observed resonances arise from anisotropy effects in their interactions [31], which are called anisotropy-induced Feshbach resonances and are originally discussed for collisions of strongly dipolar atoms such as erbium [94, 95] and dysprosium [96].

### 3.3 Yb–Li mixture

#### 3.3.1 Large mass imbalance

The most important feature of Yb–Li mixtures is their large mass imbalance  $m_{\text{Yb}}/m_{\text{Li}} \approx 29$ . This results in an extreme imbalance of their tunneling rates in an optical lattice. In a deep optical lattice the tunneling  $t$  is given by Eq. (2.48). For a  $\lambda = 532$  nm lattice used in the present work, the recoil energies and the ratio of the  $s$ -parameters for Yb and Li are  $E_{\text{R}}^{\text{Yb}} = 195$  nK,  $E_{\text{R}}^{\text{Li}} = 5.6$   $\mu\text{K}$ , and  $s_{\text{Yb}}/s_{\text{Li}} = 21.4$ , respectively. Tunneling rates calculated by Eq. (2.48) using these values are displayed in Fig. 3.6(a). Even at  $1 E_{\text{R}}^{\text{Li}}$  lattice depth for Li, Yb atoms already feel a  $20 E_{\text{R}}^{\text{Yb}}$  deep lattice potential and its tunneling rate is three orders of magnitude smaller than that of Li. That is to say, Yb atoms are deeply localized in lattice sites while Li atoms are still mobile in the system as illustrated in Fig. 3.6(b). This realizes an atomic impurity system where Li acts as itinerant fermions and Yb as localized impurities.

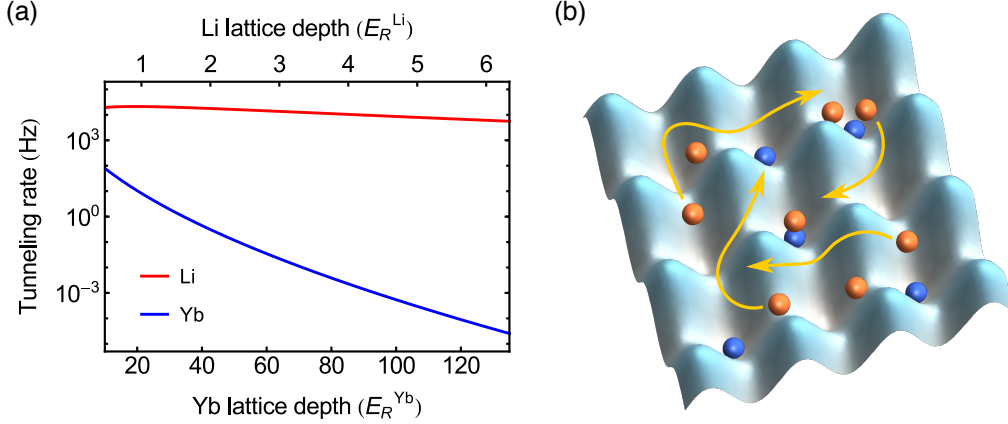


**Figure 3.6.** Yb–Li mixture in an optical lattice. (a) Tunneling rates of Li (red) and Yb (blue) at various lattice depths at  $\lambda = 532\text{nm}$  calculated by Eq. (2.48). The Yb tunneling rate is more than two orders of magnitude smaller than that of Li. (b) Illustration of a Yb–Li mixture in an optical lattice. Yb atoms (blue) are deeply localized in lattice sites while Li (orange) are moving around the sites in the whole system.

### 3.3.2 Collisional properties

#### Yb( $^1\text{S}_0$ )–Li collision

The absolute value of the  $s$ -wave scattering length between Yb and Li has been determined to be  $|a_{\text{Yb-Li}}| = 1\text{ nm}$  from their thermalization time constant [97]. This allows Li atoms to be sympathetically cooled by collisions with Yb atoms (see Section 5.2). Its sign was deduced to be positive from the reduction of the Yb oscillation frequency in the presence of Li recently [98].

In order to study impurity problems with Yb–Li mixtures, control of inter-species collisional properties is necessary. FRs between Yb and Li in their respective ground states have been theoretically calculated in [28]. The authors predict that resonances would exist at around 1 kG with a width of at most less than 1 mG. This is too narrow to precisely tune the interaction. We should find another way to control inter-species interactions.

#### Yb( $^3\text{P}_2$ )–Li collision

The metastable excited  $^3\text{P}_2$  state of Yb offers an interesting possibility to control interactions between Yb and Li. FRs between ground and excited  $^3\text{P}_2$  state Yb atoms have been observed as mentioned above, demonstrating the feasibility of working with FRs between different orbitals. In consideration of these recent results, it is reasonable to also expect some useful FRs in the Yb( $^3\text{P}_2$ )–Li system.

Indeed, several theoretical investigations of FRs in  $^{174}\text{Yb}(^3\text{P}_2)\text{-}^6\text{Li}$  [34, 38] and  $^{171}\text{Yb}(^3\text{P}_2)\text{-}^6\text{Li}$  systems [35] are reported. The existence of several FRs is predicted. Considering the complexity of the calculations involved, together with uncertainty of the constructed inter-atomic potentials, experimental feedback is indispensable to refine quantitative predictions of resonance positions and inelastic loss rates.

In previous works, a mixture of  $^{174}\text{Yb}(^3\text{P}_2, m_J = -1)$  and  $^6\text{Li}$  was realized at a few  $\mu\text{K}$  [36], and variations of the inelastic loss rate of the  $^{174}\text{Yb}(^3\text{P}_2, m_J = -1)\text{-}^6\text{Li}$  collisions for 100–520 G were observed [37]. Further experimental investigations of inelastic collisions should give further insight into  $\text{Yb}(^3\text{P}_2)\text{-Li}$  collisions. Especially, FRs in a  $^{174}\text{Yb}(^3\text{P}_2, m_J = -2)\text{-}^6\text{Li}$  system are theoretically predicted [38] based on optimized potentials obtained from the  $m_J = -1$  experimental results. Experimental confirmation of those predictions are as of yet lacking.

## Experimental setup

This chapter describes our experimental setup. The setup is composed of a vacuum apparatus and optical systems. Most parts of them have been constructed by predecessors and are described in their theses [99, 100]. In the first two sections we briefly review the overall vacuum and laser setups. The rest of this chapter details changes to the setup related to the present work.

### 4.1 Vacuum system

#### 4.1.1 Overview of the vacuum apparatus

Cold atom experiments require an ultrahigh vacuum environment in order to suppress unwanted collisions of trapped atoms with background gases. Our vacuum apparatus consists of a dual species oven, a Zeeman slower pipe, and a main experimental chamber, in contrast to a vacuum setup with separate ovens and Zeeman slowers for individual species as in [101]. This configuration makes the system compact, however, it is more difficult to optimize atomic beam parameters independently.

The dual species oven turned out to be the most difficult part to design properly. A revision history of the oven and the design concept of the latest version is explained in Section 4.1.2. A differential pumping tube is installed between the oven and the Zeeman pipe to keep the vacuum of the main region better. Also an atomic beam shutter is installed after the differential pumping tube. The shutter is a stainless steel sphere with

a through hole and is attached to a rotational actuator. The actuator is externally controlled to open or to close the shutter. It is kept closed apart from the atom loading stage during the experimental sequence to prevent trapped atoms from colliding with the atomic beam.

The Zeeman slower pipe is 285 mm long and its inner diameter is 16 mm. This also work as a differential pumping tube. The pipe is connected to the main metallic chamber. The chamber has four pairs of view ports. One is in the vertical direction, another two are 45° from the atomic beam direction in the horizontal plane, and the other is orthogonal to the atomic beam. All ports are ICF70 except for the pair orthogonal to the atomic beam in the horizontal plane which are ICF34. The vacuum in the main region is  $4\text{--}5 \times 10^{-12}$  Torr, which is realized by a combination of a 200 L/s ion pump and a titanium sublimation pump. This is clean enough to produce quantum degenerate atomic samples.

### 4.1.2 Dual species oven

We developed a new atomic oven because of decreased performance of the previous version. Before we introduce the new design, we review the previous ovens and troubles with their operations to understand the design concept of the new version.

#### History of our dual species oven

The first generation of our dual species oven consisted of a single container for the atoms and a short honeycomb nozzle, an array of thin tubes [99, 102]. Though this type of oven is simple and compact and has been working well in Yb only experiments in other chambers in our group, we faced the problem that the atomic flux gradually decreased. This would probably be caused by the honeycomb pipe, whose tubes were so thin that either species stuck to its walls and blocked the atom vapor from passing through.

The second generation of our oven, therefore, was designed without a honeycomb pipe [100]. Instead of using an array of thin tubes, we used a single long pipe in the nozzle part so that an atomic beam after the nozzle has the same divergence as with a honeycomb collimator. Also inspired by [103], this oven had two containers to separate Yb and Li to prevent them from any chemical reactions, because Li is liquid at the operational temperature of around 350 °C.

Initially this oven worked well, but we soon suffered from leaks at the flanges on the tops of the containers. The leaks were caused by thermal stress on the flanges by daily cycles from room temperature to several hundred °C and by chemical reactions of nickel

gaskets probably with Yb vapor [101]. We were able to partly overcome this problem by minor changes of the design such as having a long neck between the flanges and the nozzle so as to keep the temperature change at the flanges small, and putting a disk between the flange and the nozzle to prevent Yb and Li gases from coming up to the gaskets.

Apart from the leak trouble, later another strange and serious problem appeared. The vacuum pressure before the Zeeman slower gradually got worse for a few days and suddenly it dropped by about a half and again gradually increased. The period of this cycle was about a week. We could obtain an excellent number of atoms in MOTs and degenerate gases for a couple of days just after the drop of the vacuum pressure, but for the remainder of the time it was difficult to get sufficient number of atoms to do experiments. Interestingly, the drop of the vacuum always happened accompanied by a 10 °C temperature drop at the Yb oven part. This weird behavior still remains a mystery. One possible reason for the temperature drop at the Yb oven would be a bumping of liquid Li, but its relation with the vacuum change is unclear. It was difficult to continue experiments with this weird oven. Finally we decided to develop a new version of our dual species oven.

### **New oven**

Based on the above experiences, required specifications for the new design are;

1. no use of a honeycomb nozzle,
2. no heated flanges,
3. perfect separation of Yb and Li vapor till the oven exit.

To satisfy all these requirements, we designed separated parts of an atom reservoir and a double collimator system. A drawing of the new design is shown in Fig. 4.1.

The reservoir part has two reservoirs for Yb and Li. The collimator part is a 130 mm long cylinder and has two  $\phi 2.5$  holes whose centers are 4 mm apart. The upper one is a through-hole, a nozzle for Li vapor, and the lower is 105 mm deep and connects to an opening for the Yb reservoir. The collimator is fixed to the reservoir with vacuum compatible, vented screws. The surface of the collimator and the inner surface of the reservoir in the region indicated by the double-headed arrow in Fig. 4.1 have fit tolerance of h7 and H7, respectively, with which they fit smoothly but tightly. This ensures a tight gas seal between the Yb and Li reservoirs and good thermal contact between the outer reservoir and the inner collimator in this region.

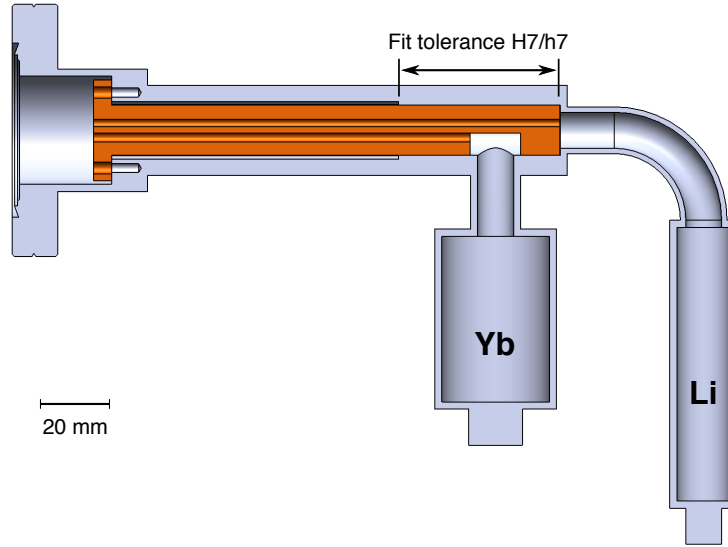


**Figure 4.1.** New dual species oven. It is an assembly of an outer reservoir part and an inner collimator part. Chunks of Yb with its natural abundance and enriched  ${}^6\text{Li}$  atoms are loaded in their respective reservoirs. The amounts of them are 50 g and 2.5 g, respectively. The collimator has two  $\phi 2.5$  holes that are separated nozzles for Yb and Li. The reservoir and collimator fit with fit tolerance of H7/h7 in the region indicated by the double-headed arrow, which ensures a tight gas seal between the Yb and Li reservoirs and good thermal contact between the outer reservoir and the inner collimator in this region.

We had two candidates for the material of the collimator, copper and stainless steel. Copper has a good thermal conductivity, but it reacts with Li vapor at high temperatures. As far as chemical reactions with vapor are concerned, stainless steel would be a good choice, however, its thermal conductivity is 15 times smaller than that of copper.

The collimator is heated only from the heated outer reservoir at the two ends. We calculated how long it takes for the center part to arrive at operation temperature from room temperature. We consider a situation that a 90 mm long cylinder initially at  $20^\circ\text{C}$  is touching  $400^\circ\text{C}$  heat baths at the both ends as illustrated in Fig. 4.2(a). The time

**Table 4.1.** Properties of material candidates for the collimator. Values for stainless steel are those of SUS430 that has the highest thermal conductivity in stainless steel.

	Thermal conductivity $k$ (W/(m·K))	Density $\rho$ (kg/m <sup>3</sup> )	Specific heat capacity $c_p$ (J/(kg·K))
Copper	400	8940	385
Stainless steel	26	7700	460

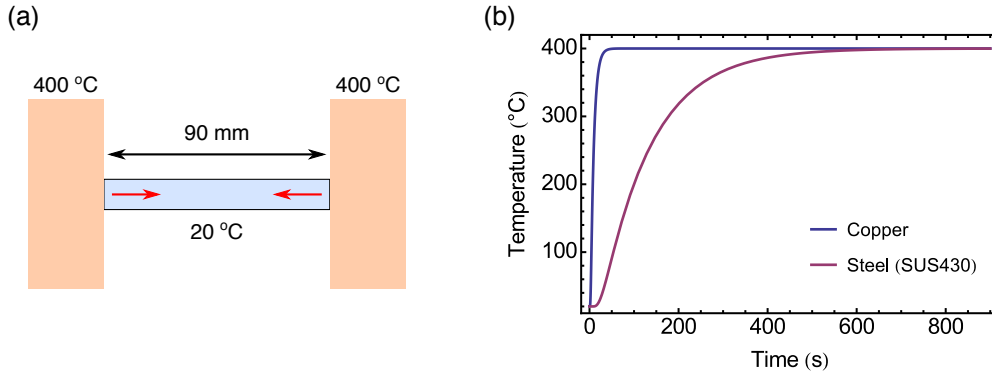


**Figure 4.2.** Modeled heat conduction of the collimator. (a) A 90 mm long bar at 20 °C is touching 400 °C heat baths at the both ends. Heat is transferred from the both sides to the center. Time evolution of the center temperature is obtained by solving Eq. (4.1). (b) Solutions of Eq. (4.1) for copper (blue) and stainless steel (red). Copper reaches the final temperature after 50 s while stainless steel takes 10 minutes.

evolution of the temperature at the center is obtained by solving the heat conduction equation

$$\frac{\partial T}{\partial t} = \alpha \nabla^2 T, \quad (4.1)$$

where  $\alpha = k/\rho c_p$  is the thermal diffusivity with the thermal conductivity  $k$ , the density  $\rho$ , and the specific heat capacity  $c_p$ . Values of these quantities for copper and stainless steel (SUS430) are given in Table 4.1.

Figure 4.2(b) shows results for copper and stainless steel. Stainless steel needs about 10 minutes to get the final temperature whereas copper takes less than a minute. Though the steel requires 10 times longer to sufficiently heat up compared to copper, this should not pose a problem in daily operation. The oven temperature is increased from room to operation temperature within 70 minutes, a time sufficient to allow the collimator stage to also heat up sufficiently. Finally we decided to use stainless steel (SUS430) for the collimator.

We load 50 g of Yb with its natural abundance and 2 g of enriched  $^6\text{Li}$  and 0.5 g of natural abundant Li in their respective reservoirs. The new oven has been trouble-free for two years now.

## 4.2 Laser systems

This section describes laser systems for laser cooling, trapping, and imaging of atoms. Cooling procedure consists of three steps; Zeeman slowing, magneto-optical trapping

(MOT), and evaporative and sympathetic cooling (see Section 5.2 for details). Since Zeeman slowing, MOT, and imaging utilize optical transitions of atoms, lasers for these purposes need to be frequency-stabilized. Here we explain specification and frequency stabilization of each laser.

### Li cooling laser

The  $D_2$  line (671 nm) of  ${}^6\text{Li}$  is utilized for laser cooling and imaging of Li atoms. The light source is a ring dye laser (899-21, Coherent Inc.) pumped by an optically pumped semiconductor laser (Taipan, Coherent Inc.) at 6 W with a wavelength of 532 nm. The dye is a solution of LD688 and ethylene glycol monophenyl ether. Typical output power of the dye laser is 250–350 mW. The output of the dye laser is divided into four properly frequency-shifted beams for Zeeman slowing, MOT cooling, MOT repumping, and imaging as shown in Fig. 4.3. The frequencies of the cooling and repumping beams can be tuned independently by direct digital synthesizers (DDSs). The laser frequency is stabilized to a cavity made of ultra low expansion (ULE) glass by the Pound-Drever-Hall (PDH) method [104]. Figure 4.4 shows the optical setup for the frequency locking to the ULE cavity.

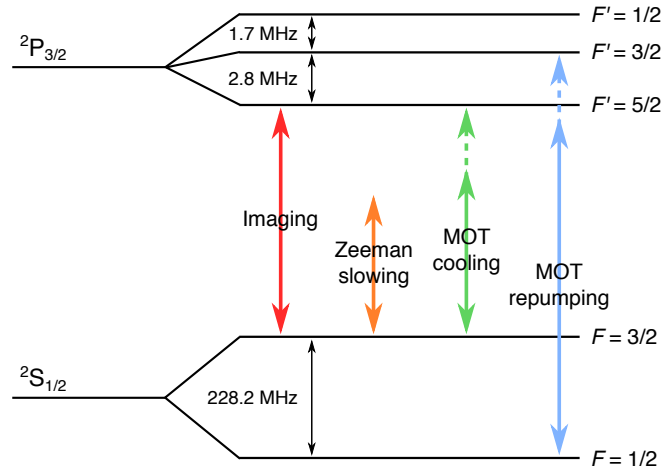


**Figure 4.3.** Four beams for Li cooling and imaging. The imaging beam is resonant to the  ${}^2S_{1/2}(F = 3/2) \rightarrow {}^2P_{3/2}(F' = 5/2)$  transition. Zeeman slowing and MOT cooling beams are detuned from the  ${}^2S_{1/2}(F = 3/2) \rightarrow {}^2P_{3/2}(F' = 5/2)$  transition. The repumping beam resonant to the  ${}^2S_{1/2}(F = 1/2) \rightarrow {}^2P_{3/2}(F' = 3/2)$  transition is applied during MOT loading and imaging to depopulate atoms from the  $F = 1/2$  state. The cooling and repumping frequencies can be independently tuned by DDSs.

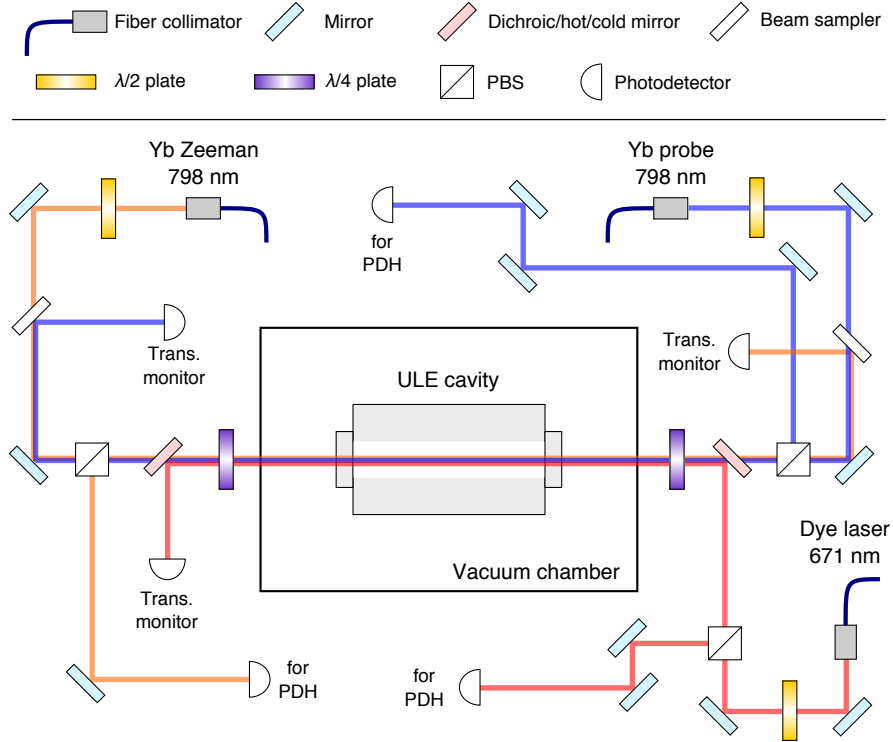


**Figure 4.4.** Frequency locking setup for the dye laser, the Ti:S laser for Yb Zeeman slower, and the 798 nm ECLD for Yb imaging. The three lasers are locked to a single ULE cavity by the PDH method. The cavity is placed in a vacuum chamber and stabilized to its zero-expansion temperature. The 671 nm beam is combined with and separated from the two 798 nm beams with cold mirrors. The two 798 nm beams oppositely enter the cavity and are separated by their polarizations.

### Yb Zeeman slower

399 nm light used for Zeeman slowing of Yb is generated by frequency-doubling of a 798 nm light from a Titanium:Sapphire (Ti:S) laser pumped by a diode-pumped solid state (DPSS) laser (Millenia eV, Spectra-Physics) at 10 W with a wavelength of 532 nm. Output power of the Ti:S laser is about 800 mW. Its frequency is stabilized to the same ULE cavity as the dye laser by the PDH method (see Fig. 4.4). The output of the Ti:S laser is converted into 399 nm by second harmonic generation (SHG) with a barium metaborate (BBO) crystal in a bow-tie cavity. The SHG cavity is stabilized by the Hänsch-Couillaud method [105]. Output power of the SHG cavity is 180 mW.

### Yb MOT laser

The 556 nm light resonant to the narrow  $^1S_0 \rightarrow ^3P_1$  transition used for the MOT of Yb atoms is generated by SHG of a 1112 nm laser [106]. The source of the 1112 nm light is a

fiber amplifier (Keopsys) seeded by a fiber laser (CYFL-KILO, Keopsys). The fiber laser is frequency-stabilized to a ULE cavity with higher finesse than that for the dye laser by the PDH method and its linewidth is less than 100 kHz. After an SHG cavity with a lithium triborate (LBO) crystal 130 mW output of 556 nm light is obtained. After an AOM and a fiber 80 mW is available for the MOT.

### Yb imaging laser

The laser system of 399 nm for Yb imaging consists of an external cavity laser diode (ECLD) and a tapered amplifier (TA) at 798 nm and an SHG cavity with a periodically poled KTP (PPKTP) crystal. The frequency of the ECLD is stabilized to the same ULE as the dye laser and the Ti:S laser by the PDH method (see Fig. 4.4). Output from the SHG cavity is 50–70 mW.

### FORT lasers

The atoms captured in their respective MOTs are transferred into a crossed optical far-off-resonance trap (FORT). The crossed FORT is composed of a horizontal FORT with a wavelength of 1070 nm and a vertical FORT with a wavelength of 1064 nm. Laser sources are fiber lasers (YLR-LP series, IPG Photonics) and are operated at 65 W and 40 W, respectively. The horizontal FORT beam is elliptical with the waists of 22  $\mu\text{m}$  horizontally and 79  $\mu\text{m}$  vertically, and the vertical FORT beam is round with the waist of 82  $\mu\text{m}$  at the atom position.

## 4.3 Gravitational-sag compensation beam

One obstacle to be overcome in experiments with Yb–Li mixtures is the reduced spatial overlap between the Yb and Li atom clouds due to their different gravitational sag. To compensate for this, we apply an intensity gradient of a  $\lambda = 532$  nm laser, which acts as an attractive potential for Yb and a repulsive one for Li. Section 5.3 details effectiveness of this gravitational sag compensation beam (GCB).

The laser source is a DPSS laser (Verdi-V10, Coherent Inc.), shared with the optical lattice beams. The output of the source is divided into four beams, one for the GCB and the others for the lattice, and they are delivered to the vicinities of the chamber by optical fibers. Figure 4.5 shows a picture of the optical path of the GCB after the fiber. The GCB is superimposed on the H-FORT beam just in front of the chamber at a dichroic mirror. For a precise control of the pointing of the beam at the atom position,

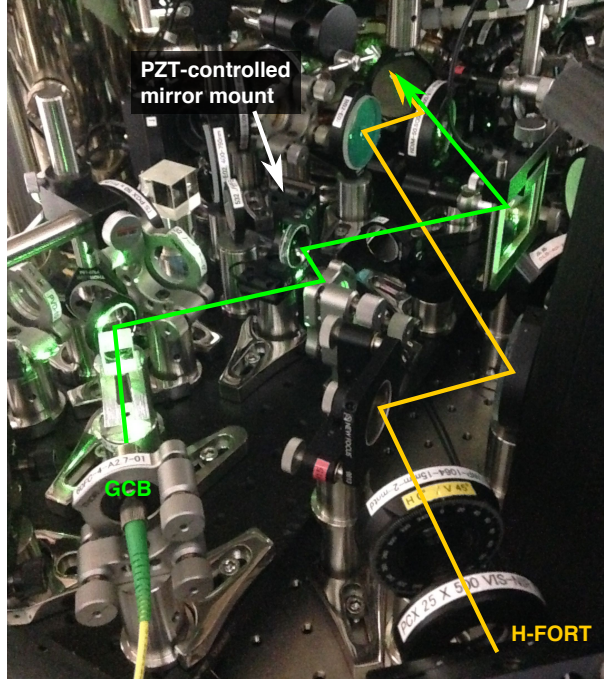


**Figure 4.5.** The optical path of the GCB around the chamber. The GCB (green) is superimposed on the H-FORT beam (yellow) just in front of the chamber at a dichroic mirror. One of the mirrors for the GCB is mounted on a piezo-driven mirror mount so as to precisely tune the pointing of the beam.

one of the mirrors for the GCB is mounted on a piezo-driven mirror mount (AG-M100N, Newport corporation). The GCB is focused down to  $75\ \mu\text{m}$  at the position of trapped atoms.

## 4.4 Optical lattice

We have previously installed a three-dimensional optical lattice with a wavelength of  $1064\ \text{nm}$  in our setup [107]. We observed the disappearance of interference patterns of an Yb BEC and performed  $^3\text{P}_2$  spectroscopy in an  $^{174}\text{Yb}$ - $^6\text{Li}$  quantum degenerate mixture in the lattice. However, we encountered difficulties in the adiabatic loading of an Yb BEC into the lattice and in performing spectroscopy with high resolution.

Optical lattice experiments with Yb atoms are conveniently done with a  $\lambda_L = 532\ \text{nm}$  lattice<sup>1</sup>. In a  $532\ \text{nm}$  lattice, adiabatic loading of an Yb BEC [108] and high-resolution  $^3\text{P}_2$  spectroscopy [78] have been successfully performed. Figure 4.6 contrasts a  $1064\ \text{nm}$

<sup>1</sup>In experiments particularly using the  $^3\text{P}_0$  state,  $\lambda = 759\ \text{nm}$  light is used for an optical lattice. Atoms in the  $^1\text{S}_0$  and  $^3\text{P}_0$  states feel same amount of light shift in a trap at this wavelength, which is called a “magic wavelength.”

and 532 nm lattice. Lattice sites for Yb and Li coincide in a 1064 nm lattice whereas in a 532 nm lattice they alternate. This is why we first chose 1064 nm for our lattice.

However, the ratio of tunneling rates  $t$  in a 1064 nm and 532 nm lattice is  $t_{1064}/t_{532} = 1/4$  because  $t \propto E_R$  at the same lattice depth parameter  $s$  as shown in Eq. (2.48). In addition, since a lattice spacing of a 1064 nm lattice is twice larger than that of a 532 nm lattice, energy offset differences between neighboring sites  $\Delta\varepsilon_i = \varepsilon_{i+1} - \varepsilon_i$  produced by a global harmonic confinement of the optical traps are  $\Delta\varepsilon_i^{1064} > \Delta\varepsilon_i^{532}$ . Therefore Yb atoms in a 1064 nm lattice hardly spread to as many lattice sites as in a 532 nm lattice and many atoms tend to localize in same sites. This reduces adiabaticity of the system.

Also in a  $^3P_2$  spectroscopy experiment, a 532 nm lattice has an advantage over a 1064 nm lattice. In a deep lattice, single lattice sites can be treated as harmonic potentials and vibrational levels separated by  $\hbar\omega = \sqrt{4s} \times E_R$  are formed. At  $s = 15$  excitation to the  $^3P_2$  state in a higher vibrational level ( $v = 0 \rightarrow v' = 1$ ) is spectroscopically well resolved from carrier excitation ( $v = 0 \rightarrow v' = 0$ ), but the separation in a 1064 nm lattice is four times smaller than in a 532 nm lattice. Furthermore, in a Mott insulating state resonance frequencies of atoms in singly occupied sites and doubly occupied sites are shifted due to the interatomic interaction. Since the on-site interaction  $U$  is proportional to  $\omega^{3/2}$ ,  $U^{1064}/U^{532} = 1/8$ . This makes it difficult to spectroscopically resolve multiply occupied sites from singly occupied sites in a 1064 nm lattice.

The rightmost figures in Fig. 4.6 contrast sketches of typical  $^3P_2$  spectra of an Yb Mott insulator at  $s = 15$  in 1064 nm and 532 nm lattices. In a 1064 nm lattice the carrier peak and the higher bands are barely resolved, further the double occupancy peaks overlap with the singly occupancy peaks, whereas in a 532 nm lattice all peaks are well resolved.

Therefore we decided to use a 532 nm lattice instead of a 1064 nm one. Though lattice sites for Yb and Li alternate in a 532 nm lattice because of opposite signs of their polarizabilities, Li is sufficiently delocalized to reasonably overlap with localized Yb at suitable lattice depths as  $s_{Yb}/s_{Li} = 21.4$ .

The light source is the same laser as the GCB. Three branching beams for the lattice are delivered in the vicinities of the chamber by optical fibers. Their frequencies are slightly shifted by AOMs before the fibers to avoid unwanted interferences between the three at the atom position. Beam waists are 70–80  $\mu\text{m}$ . A lattice is formed by retro-reflecting each beam after the chamber. Lattice depths are calibrated by the pulsed optical lattice method [109] onto an Yb BEC.

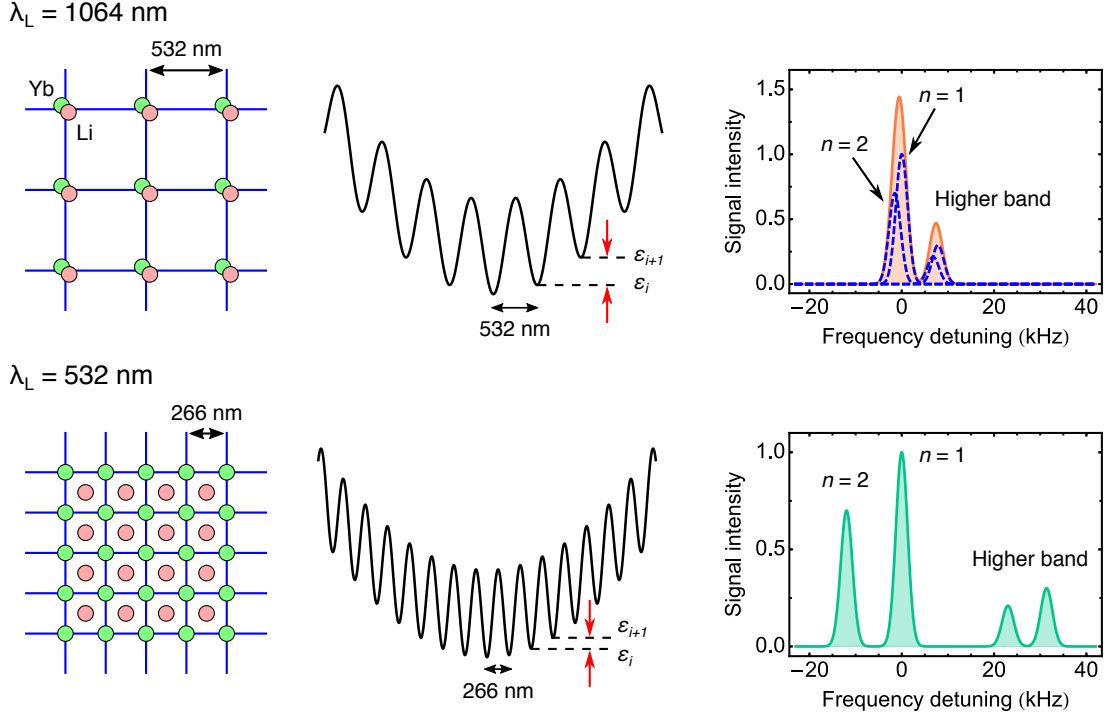


**Figure 4.6.** Differences between lattices at  $\lambda_L = 1064$  nm (upper row) and 532 nm (lower row). (Left) Lattice sites for Yb and Li coincide in a 1064 nm lattice whereas they alternate in a 532 nm lattice. (Middle) There exists a global harmonic confinement by the optical traps, which produces an energy offset difference between neighboring sites as  $\Delta\varepsilon_i = \varepsilon_{i+1} - \varepsilon_i$ . Since the lattice spacing of a 1064 nm lattice is twice that of a 532 nm lattice, neighboring site energy differences are  $\Delta\varepsilon_i^{1064} > \Delta\varepsilon_i^{532}$ . Therefore the number of sites the atoms spread to is much smaller in a 1064 nm lattice than in a 532 nm lattice. This makes it difficult to adiabatically load atoms into a 1064 nm lattice. (Right) Sketches of typical  $^3P_2$  spectra of an Yb Mott insulator at  $s = 15$ . All peaks are well resolved in a 532 nm lattice whereas they can hardly be resolved in a 1064 nm lattice. The blue dashed lines denote individual lineshapes of the peaks and the orange curve denote the observable total of them.

## 4.5 Setup for $^3P_2$ state preparation and detection

This section describes experimental setups for  $^3P_2$  state preparation and detection. In order to perform high-resolution spectroscopy of Yb atoms in an optical lattice as an inter-atomic interaction probe [29, 30], we develop an ultra-narrow 507 nm excitation laser. A 100 Hz linewidth is achieved by locking it to a high-finesse cavity.

For a high-sensitive detection of the excited Yb atoms, we construct a fluorescence imaging system similar to the one presented in [110]. In order to perform the fluorescence imaging of the excited atoms, we need lasers to repump them into the ground state as well as a MOT system using the strong  $^1S_0 \rightarrow ^1P_1$  transition. In the following the

excitation laser, the repumping lasers, and the fluorescence imaging system are detailed.

### 4.5.1 Excitation laser

#### Light source

The 507 nm excitation light is generated by SHG of a 1014 nm laser. The laser system is composed of an ECLD and a TA at 1014 nm and an SHG module. The frequency of the ECLD is locked to a high-finesse ULE cavity by the PDH method.

The ECLD is Littrow configuration with an AR-coated LD chip (EYP-RWE-1060, Eagleyard photonics). Its frequency can be tuned by a piezo element attached to a diffraction grating [111]. The current source for the ECLD is an ultra-low noise and high bandwidth controller (D2-105, Vescent Photonics), which is based on the Libbrecht-Hall circuit [112]. Performance of the ECLD is presented in Fig. 4.7(a). We operate it at 95 mA and obtain 27 mW after two optical isolators. The beam is divided into two branches, 20 mW go to the TA and the rest to the frequency locking.

The tapered amplifier (TA-1010-2000-DHP, m2k Laser) amplifies the seed light up to 2.3 W (see Fig. 4.7(b)). The output of the TA is coupled to an SHG module with a periodically poled lithium niobate (PPLN) waveguide (WH-0507-000-A-B-C, NTT Electronics) via a fiber. Figure 4.8(a) shows a picture of the SHG module. Phase matching (temperature optimization) of the crystal is necessary to get the highest conversion efficiency. As a result of the phase matching, maximal SHG output power is 180 mW (see Fig. 4.8(b)). The 507 nm light is brought to the vicinity of the chamber via a fiber. There

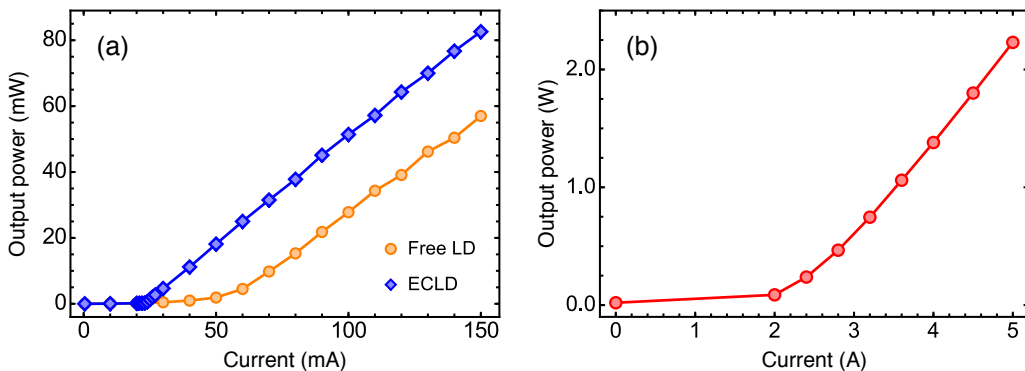


**Figure 4.7.** Performance of the ECLD and TA. (a) Output power of the free running LD (without grating) and the ECLD (with grating). Grating feedback starts to work at around 24 mA. The ECLD is operated at 95 mA in the experiment. (b) Output power of the TA. Seed power is 20 mW. We can obtain 2.3 W output power at maximum TA current.

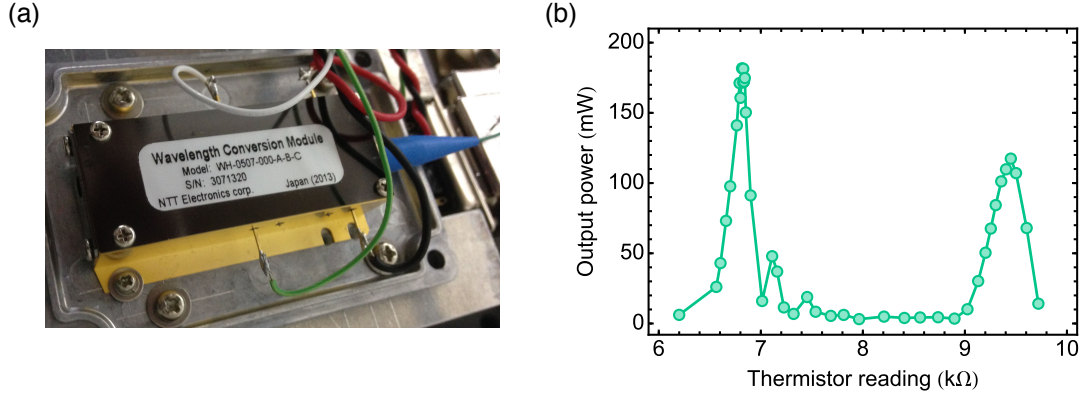


**Figure 4.8.** Second harmonic generation of 507 nm light. (a) Picture of the PPLN waveguide SHG module. 1014 nm light is coupled to the crystal via an attached fiber and output of the 507 nm light is free air. The temperature of the crystal inside the module is stabilized. (b) Phase matching of the SHG. SHG output power depends on the crystal temperature. The horizontal axis is the 10 k $\Omega$  thermistor reading. TA output is 2.3 W. We can obtain about 180 mW output power at the optimal crystal temperature.

is an AOM for switching and power control after the fiber. The power is stabilized by an intensity stabilization circuit. The beam waist at the atom position is  $\approx 50 \mu\text{m}$ .

The frequency of the ECLD is locked to a high finesse ULE cavity by the PDH method. A portion of the ECLD output is brought to the cavity via two fiber EOMs (see Fig. 4.9). The first one is used for frequency tuning of the laser. The light after the EOM has frequency sidebands both on the positive and negative sides of the carrier frequency. The frequency difference between the sidebands and the carrier corresponds to the rf applied to the EOM. We lock either sideband component to the cavity and tune the laser frequency relative to the ULE locking point by changing the EOM driving frequency. The second EOM, which is driven by a 16 MHz crystal oscillator, is used to generate an error signal by the PDH method.

The finesse and the free spectral range (FSR) of the cavity is 50,000 and 1.5 GHz, respectively. Feedback is applied to the current controller and the piezo driver through a high-speed laser servo (D2-125, Vescent Photonics). As a result of the tight lock to the ULE cavity the linewidth of the ECLD is narrowed down to  $\approx 100$  Hz, which is evaluated by measuring beat linewidths of all combinations of the three independent 1014 nm laser sources available in our laboratories. Figure 4.9 shows a schematic of the laser apparatus.

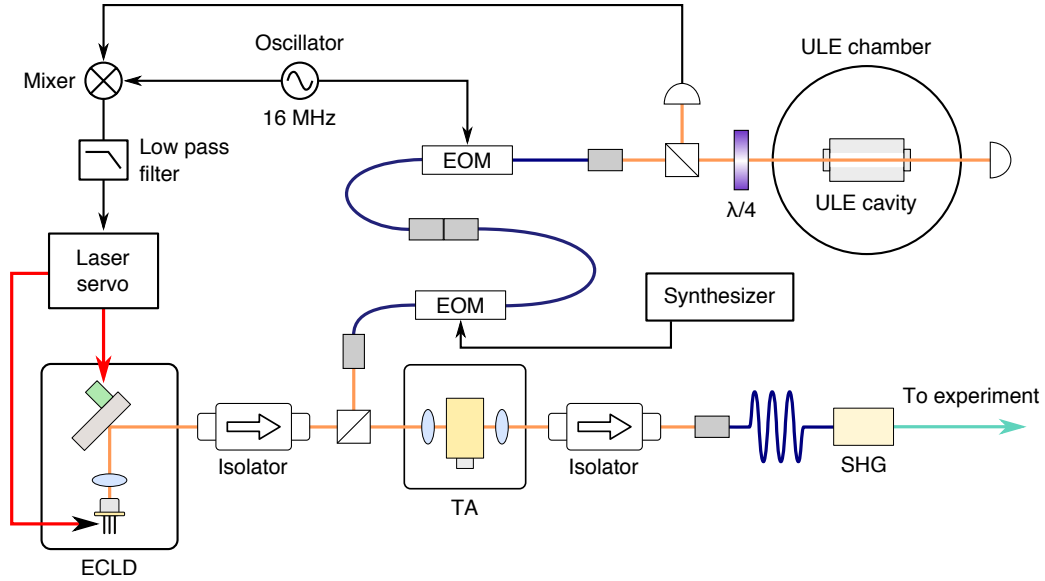


**Figure 4.9.** Schematic of the 507 nm laser system. It is composed of a Littrow configuration ECLD and a TA of 1014 nm and an SHG module. The ECLD is locked to a high finesse ULE cavity by the PDH method. A portion of the ECLD output is brought to the cavity via two fiber EOMs. A sideband generated by the first EOM is locked to the cavity and the ECLD frequency is tuned by a radio frequency applied to the EOM. The second EOM generates sidebands for the PDH locking. A laser servo sends feedback to the current and the piezo voltage.

### ULE cavity

In order to achieve narrow and stable frequency locking, the ULE cavity should be isolated from ambient noises such as thermal and acoustic fluctuations. We put the cavity in a temperature-stabilized vacuum chamber and place it on a vibration isolation platform made by Minus K in an acoustic isolation box.

ULE glass has a temperature at which its coefficient of thermal expansion (CTE) becomes zero. Therefore, a cavity made of the ULE glass whose temperature is stabilized to the zero expansion temperature becomes a good reference to the wavelength. Since the ULE cavity we use was made to have its zero expansion temperature around 30–40 °C, the chamber is heated by a 300 W film heater made by Kawai corporation (see Fig. 4.10(a)). At first we tried to control the heater by a heater controller (TC200, Thorlabs), but it turned out that its power was insufficient to heat the chamber higher than 36 °C. Next we tried a higher power temperature controller (TED4015, Thorlabs), however, it was limited by a voltage limitation and the chamber could not be heated beyond 30 °C.

Therefore we constructed a temperature control system using an external power sup-

## 4.5. SETUP FOR $^3\text{P}_2$ STATE PREPARATION AND DETECTION

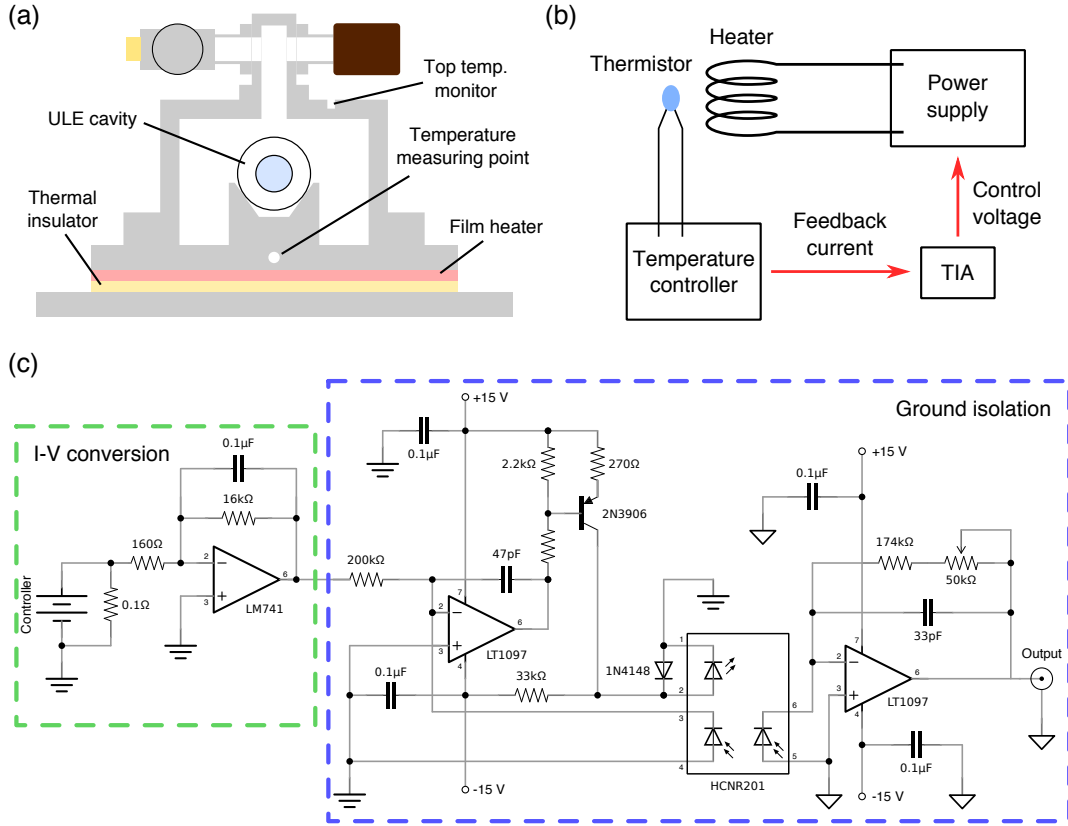


**Figure 4.10.** Temperature stabilization of the ULE chamber. (a) Schematic of the ULE vacuum chamber. There are two temperature sensors (thermistors) on the top and the bottom of the chamber. The temperature controller evaluates the bottom one while the top one is for diagnostic purposes only. The chamber is heated by a film heater underneath the base plate. (b) Temperature feedback control system. A temperature controller (TED4015, Thorlabs) generates a feedback current depending on the difference between the set temperature and the actual temperature. The feedback current is converted into a control voltage by a transimpedance amplifier (TIA). The converted voltage controls an external power supply (GP050-2, Takasago Ltd.) which applies current to the film heater. (c) Schematic diagram of the TIA. It converts a 1 A feedback current into a 10 V control voltage. The circuit consists of a current-voltage ( $I$ - $V$ ) conversion part and a ground isolation part by an analog optocoupler (HCNR201, Avago technologies).

ply. Figure 4.10(b) shows the principle of our control system. A temperature controller (TED4015, Thorlabs) creates feedback current depending on the set value and the reading of a thermistor at the center of the ULE chamber base plate. The feedback current is sent to a transimpedance amplifier (TIA), which converts a 1 A feedback current into a 10 V voltage signal. The converted voltage controls a power supply (GP050-2, Takasago Ltd.) which applies the current to the heater depending on the control voltage. Figure 4.10(c) is a schematic diagram of the TIA. The TIA consists of an current-to-voltage

conversion part and a ground isolation part by an analog optocoupler (HCNR201, Avago technologies). This system can heat the chamber beyond 40 °C and stabilize the temperature to within  $\pm 10$  mK.

Here we describe the determination of the zero expansion temperature  $T_0$ . The CTE  $\alpha$  can be assumed to linearly depend on the temperature  $T$  around  $T_0$ . Recalling the resonance frequency condition for a cavity with a length of  $L$ ,  $n\lambda = nc/f = L$ , we have to linear order of  $\alpha(T)$  the following equation,

$$\alpha(T) = \frac{1}{L} \frac{\partial L}{\partial T} = -\frac{1}{f} \frac{\partial f}{\partial T} = \alpha_0(T - T_0), \quad (4.2)$$

where  $\alpha_0$  is a CTE slope around  $T_0$ . From the rightmost equation the resonance frequency of the cavity at temperature  $T$  is derived as

$$f(T) = f_0 \exp\left(-\frac{1}{2}\alpha_0(T - T_0)^2\right), \quad (4.3)$$

where  $f_0$  is the resonance frequency at  $T_0$ . Therefore the resonance frequency has an extreme value at  $T_0$ .

We have another 1014 nm laser locked to another ULE cavity stabilized at its zero expansion temperature available. A beat frequency measurement with it is a good indication of resonance frequency shifts of our ULE cavity. We would expect to observe an inversion of the beat frequency drift if we change the ULE temperature to cross  $T_0$ . In order to evaluate  $T_0$  from the beat frequency trace, we need to know the time evolution of the ULE temperature.

The ULE cavity obtains heat only from the temperature stabilized vacuum chamber. According to Newton's law of cooling, the temperature  $T$  of a material in surroundings with a temperature  $T_{\text{env}}$  obeys

$$\frac{dT(t)}{dt} = -r(T(t) - T_{\text{env}}), \quad (4.4)$$

where  $r = hS/C$  is a positive constant characteristic of the system with the heat transfer coefficient  $h$ , the heat transfer surface area  $S$ , and the heat capacity  $C$ . The solution of this differential equation gives

$$T(t) = T_{\text{env}} + (T(0) - T_{\text{env}})e^{-rt}. \quad (4.5)$$

Therefore if the temperature of the ULE chamber is changed from  $T(0)$  to  $T_{\text{env}}$ , the resonance frequency evolves as

$$f(t) = f_0 \exp\left(-\frac{1}{2}\alpha_0(T(t) - T_0)^2\right) \quad (4.6)$$

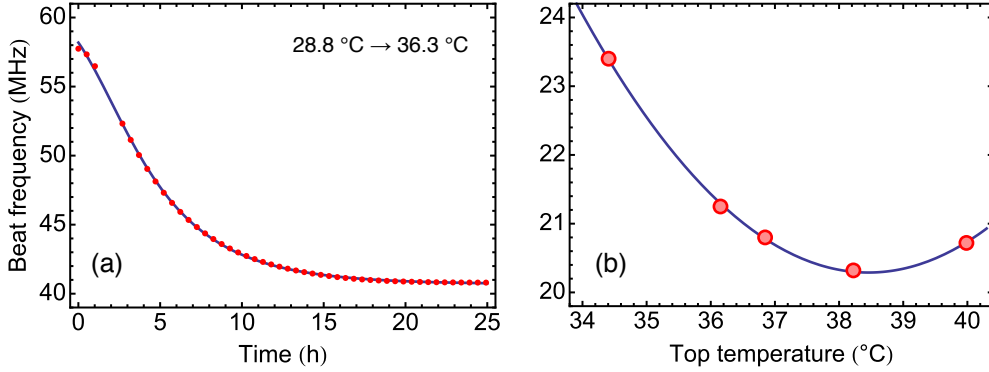


**Figure 4.11.** Determination of the zero expansion temperature of the ULE cavity. (a) Beat frequency drift from 28.8 °C to 36.3 °C. We trace the beat frequency between the ECLD locked to the ULE cavity and another ECLD locked to another ULE cavity whose temperature is stabilized to its zero expansion temperature. The red dots are measured points and the blue curve is a fit by Eq. (4.6). The fit gives  $T_0 \approx 39^\circ\text{C}$ . (b) Beat frequencies at several ULE temperatures around 39 °C. A minimum of the beat frequency is at around 38.5 °C. The blue line is a fit by a quadratic function.

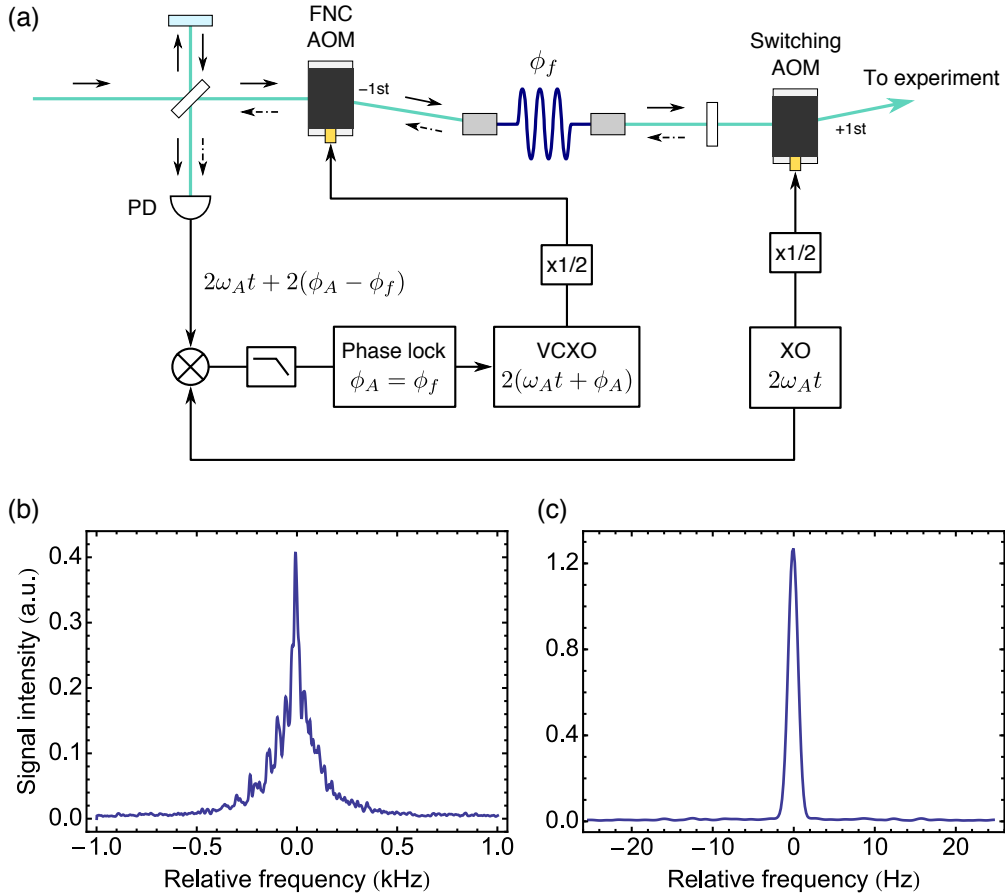
with  $T(t)$  as Eq. (4.5).

Figure 4.11(a) shows a result of a beat frequency measurement with the ULE temperature changed from 28.8 °C to 36.3 °C. Here we note that temperatures shown here are values from the sensor on the top of the chamber, though we control the bottom temperature. This is because there is a slight inconsistency in temperature calibrations of the two temperature controllers which we changed in the middle of the  $T_0$  determination measurement. In the beat frequency trace we do not observe an inversion of the frequency drift, which indicates that  $T_0$  lies above 36 °C. A fit to the trace by Eq. (4.6) gives  $T_0 \approx 39^\circ\text{C}$ . We measure beat frequencies at several ULE temperatures around 39 °C (see Fig. 4.11(b)). A fit by a quadratic function gives a minimum at 38.5 °C. In the end we set the bottom temperature to 40.15 °C so that the top temperature is around 38.5 °C.

Even though the ULE cavity is stabilized at the zero expansion temperature, there persists a residual shrinking because of the amorphousness of the glass. We check the  $m_J = 0$  resonance frequency of a free-falling  $^{174}\text{Yb}$  BEC every morning and compensate for the residual drift by evaluating a drift rate from the  $m_J = 0$  resonance frequencies on the latest several days. Right after installation we observed about 700 Hz/h and that now 1.5 years later we are at about 300 Hz/h.

### Fiber noise cancellation

Since our main experimental optical table and the 507 nm laser system are far apart, the 507 nm light is brought to the vicinity of the main experimental chamber via a 15 m long optical fiber. However a long fiber causes phase noises on the light by vibrations and thermal fluctuations of the fiber, which is unfavorable for high-resolution spectroscopy.



**Figure 4.12.** Fiber noise cancellation (FNC). (a) Setup for the FNC. We monitor a beat frequency between input light and retro-reflected light. Since the reflected light passes twice through an FNC AOM to which  $\omega_A t + \phi_A$  from a VCXO is applied and the fiber, the beat frequency is  $2\omega_A t + 2(\phi_A - \phi_f)$  with the fiber noise  $\phi_f$ . A phase lock circuit controls the VCXO to be  $\phi_A = \phi_f$  so that the fiber noise is cancelled. Monitored beat signal (b) without and (c) with the phase lock loop. The fiber noise causes about a few 100 Hz broadening on the light. It is cancelled with the phase lock loop.

We cancel the fiber induced noise out by a phase lock loop as shown in Fig. 4.12(a). We monitor the beat frequency between the light before entering the fiber and the light having passed through the fiber, having partially been retro-reflected at its output side and having thus travelled again back through the same fiber. The reflected light passes

through an AOM for FNC and the fiber twice till it is detected at the PD. Since an applied frequency to the AOM is  $\omega_{At} + \phi_A$ , half of that from a voltage-controlled crystal oscillator (VCXO), the detected beat frequency is  $2\omega_{At} + 2(\phi_A - \phi_f)$  with the fiber noise  $\phi_f$ . A phase lock circuit controls the VCXO to be  $\phi_A = \phi_f$  by comparing the beat frequency with a reference frequency  $2\omega_{At}$  from a crystal oscillator (XO). The XO drives a switching AOM after the fiber with the opposite order from the FNC AOM. Therefore the light going to the experiment has the same frequency as the light before the fiber.

The FNC can be checked by a broadening of the beat signal. The beat signal is broadened without the phase lock loop (Fig. 4.12(b)), while it has no broadening without the loop (Fig. 4.12(c)).

### 4.5.2 Repumping lasers

We use the  $^3P_2 \rightarrow ^3S_1$  (770 nm) and  $^3P_0 \rightarrow ^3S_1$  (649 nm) transitions to repump the excited atoms into the ground state. Both lights are generated by Littrow configuration ECLDs. LD chips are EYP-RWE-0790 and EYP-RWE-0650 from Eagleyard photonics, respectively. At the position of the atoms the beams are focused down to a few 100  $\mu\text{m}$

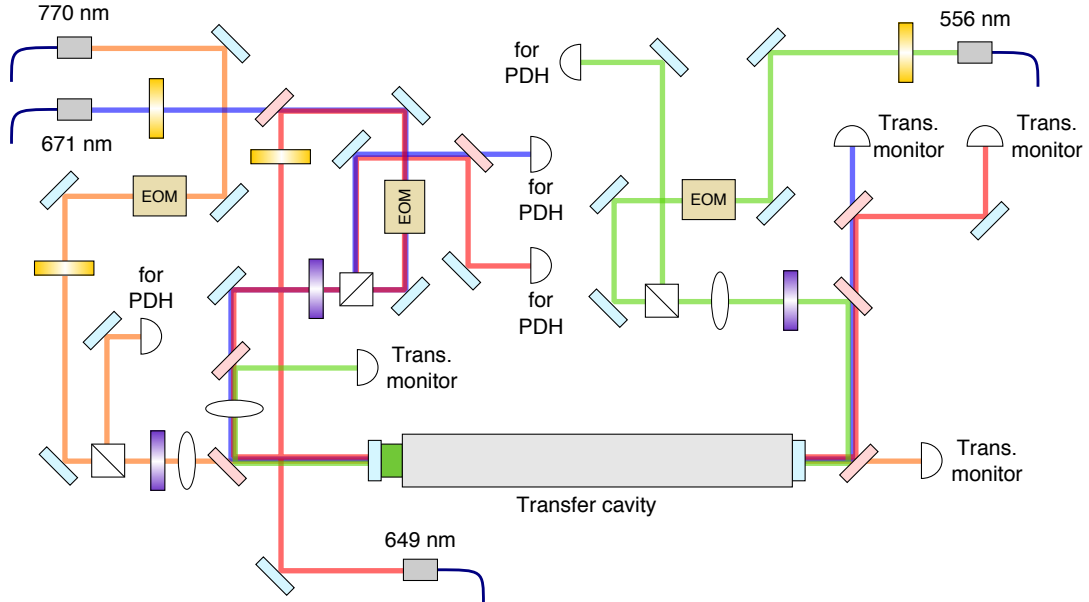


**Figure 4.13.** Frequency locking setup for the repumping lasers and the optical pumping laser. The three lasers are frequency-stabilized to a transfer cavity. The cavity length is stabilized by a 556 nm light stabilized to a ULE cavity. In addition to the two repumping lasers and the reference light, a 671 nm light for optical pumping of Li is locked to the same cavity (see Appendix A).

with powers of 6–7 mW and 2–3 mW, respectively.

Since the linewidth of the  $^3S_1$  state is 11 MHz, these lasers are not required to be as narrow as the 507 nm laser. Their frequencies are stabilized by the PDH method to a transfer cavity whose length is stabilized by 556 nm light locked to a ULE cavity. Figure 4.13 shows a schematic of the optical setup around the transfer cavity.

### 4.5.3 Fluorescence imaging

A standard technique to measure the number of atoms is absorption imaging (see Section 5.1), however, it is hard to detect a small number of atoms by this method. For detection of a small number of atoms, fluorescence imaging is more useful. We construct a fluorescence detection system for Yb using a MOT operating on the strong  $^1S_0 \rightarrow ^1P_1$  transition. We obtain our signal by integrating the fluorescence signal in time. The fluorescence intensity from the MOT is detected and is proportional to the number of atoms.

Trapped atoms should be confined in a small volume in order to reduce scattering light which limits our signal-to-noise ratio. We apply a magnetic field gradient of  $\approx 60$  G/cm, the strongest gradient our system can generate. The light is detuned by 20 MHz from the resonance frequency. A beam along each axis has a diameter of  $\approx 10$  mm and power of 5–10 mW. The fluorescence signal is detected by an EMCCD camera (iXon, Andor).

Figure 4.14(a) shows a fluorescence image of  $\approx 1000$  atoms. We evaluate the fluo-

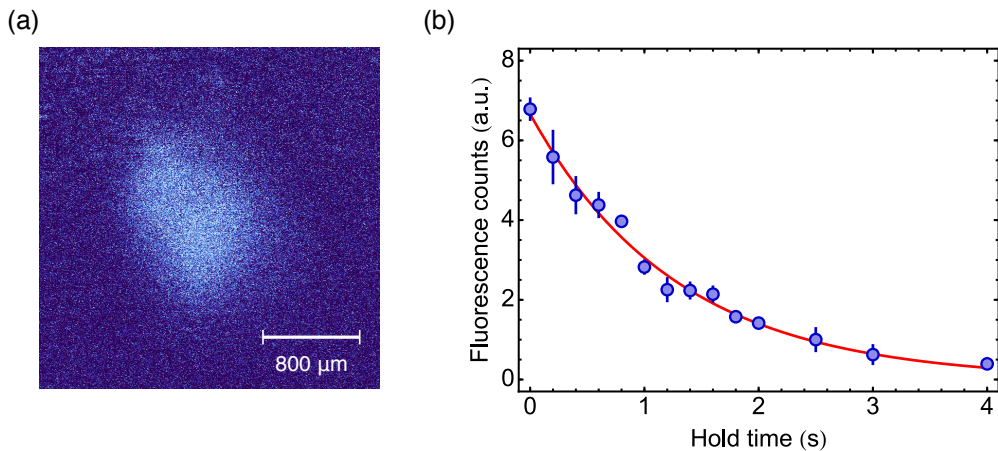


**Figure 4.14.** Detection MOT. (a) A fluorescence image of 1000 atoms. (b) Time evolution of a detection MOT. The red line denotes a fit by an exponential function. The lifetime is 1.3 s.

rescence counts by fitting the obtained images with a gaussian function. Lifetime of a fluorescence MOT is 1.3 s (see Fig. 4.14(b)). Therefore we set an exposure time for 1 s. Compared to the background noise, the detection limit is  $\approx 10$  atoms.



# Quantum degenerate mixture of Yb and Li in an optical lattice

This chapter describes the preparation of an ultracold atomic sample. First we produce a quantum degenerate Yb–Li mixture by combining laser cooling and evaporative cooling. To compensate for a reduced overlap between the Yb and Li atomic clouds due to different gravitational sags, we apply the gravitational-sag compensation beam after the production of a quantum degenerate mixture. Finally the mixture is loaded into a three-dimensional optical lattice.

## 5.1 Absorption imaging

Before recounting a cooling process to quantum degeneracy, here we explain an imaging method to evaluate the number and temperature of trapped atoms. A standard technique to measure a density distribution of trapped atoms is the absorption imaging method. We shine a resonant laser pulse on an atomic cloud and its shadow is imaged on a CCD camera. Atomic density can be evaluated from the optical density on the camera.

In the low intensity regime  $I \ll I_s$ , where  $I_s$  is the saturation intensity, the intensity distribution of a laser propagating along the  $z$  direction after passing through an atomic cloud with density distribution of  $n(x, y, z)$  is given by

$$I(x, y) = I_0(x, y) \exp\left(-\sigma_0 \int n(x, y, z) dz\right). \quad (5.1)$$

Here  $I_0(x, y)$  is the intensity profile without atoms and  $\sigma_0$  is the absorption cross section for a resonant light expressed by

$$\sigma_0 = \frac{3\lambda^2}{2\pi}, \quad (5.2)$$

with the wavelength of the laser  $\lambda$ . For Li imaging using the  $^2S_{1/2}(F = 3/2) \rightarrow ^2P_{3/2}(F' = 5/2)$  transition,  $\sigma_0$  in Eq. (5.1) should be replaced by the effective absorption cross section  $\sigma_{\text{eff}} = 2\sigma_0/3$ .

Therefore the density profile of the atoms can be evaluated from the optical density distribution on a CCD camera by

$$n(x, y) = \int dz n(x, y, z) = -\frac{1}{\sigma_0} \log\left(\frac{I(x, y)}{I_0(x, y)}\right). \quad (5.3)$$

The number of atoms  $N$  can be obtained by integrating Eq. (5.3) over the  $x$  and  $y$  directions.

## Time-of-flight method

The density profile of the trapped atoms is obtained by absorption imaging Eq. (5.3). This allows us to evaluate also the temperature of the atoms in association with the time-of-flight (TOF) method.

## Thermal gases

We release atoms from a trap and let them expand. When the temperature of the atoms is far above the BEC critical temperature or the Fermi temperature, time evolution of the density distribution of the atomic cloud is given by

$$n_{\text{th}}(\mathbf{r}, t) = \frac{N}{(2\pi)^{3/2}\sigma_x(t)\sigma_y(t)\sigma_z(t)} \exp\left(-\frac{x^2}{2\sigma_x(t)^2} - \frac{y^2}{2\sigma_y(t)^2} - \frac{z^2}{2\sigma_z(t)^2}\right), \quad (5.4)$$

where

$$\sigma_{x,y,z}(t) = \sqrt{\frac{k_B T}{m\omega_{x,y,z}^2}} b_{x,y,z}(t), \quad (5.5)$$

is the width of the cloud with the atomic mass  $m$  and the trapping frequency  $\omega_{x,y,z}$  in each direction. The scaling factor  $b_{x,y,z}(t)$  is given by

$$b_{x,y,z}(t) = \sqrt{1 + \omega_{x,y,z}^2 t^2}. \quad (5.6)$$

The density distribution obtained by the absorption imaging is the column density integrated along the imaging axis. Integrating Eq. (5.4) along the  $z$ -direction we obtain

$$n_{\text{th}}(x, y, t) = \frac{N}{2\pi\sigma_x(t)\sigma_y(t)} \exp\left(-\frac{x^2}{2\sigma_x(t)^2} - \frac{y^2}{2\sigma_y(t)^2}\right), \quad (5.7)$$

Therefore the number  $N$  and temperature  $T$  of the atoms can be evaluated by fitting the obtained density profile by Eq. (5.7). If the expansion time  $t$  is long enough ( $\omega_{x,y,z}^2 t^2 \gg 1$ ), the temperature can simply be determined by the relation  $k_B T = m\sigma^2/t^2$ . Since the cloud becomes isotropic after a long enough expansion time, the line density

$$n_{\text{th}}(x, t) = \frac{N}{\sqrt{2\pi}\sigma_x(t)} \exp\left(-\frac{x^2}{2\sigma_x(t)^2}\right) \quad (5.8)$$

can also be used for the evaluation.

### Fermi degenerate gases

Time evolution of the density distribution of a Fermi degenerate gas released from a trap is described by

$$n_{\text{FD}}(\mathbf{r}, t) = -\frac{1}{b_x(t)b_y(t)b_z(t)} \frac{g_s}{\lambda_{\text{th}}^3} \text{Li}_{3/2} \left[ -\mathcal{F} \exp\left(-\frac{x^2}{2\sigma_x(t)^2} - \frac{y^2}{2\sigma_y(t)^2} - \frac{z^2}{2\sigma_z(t)^2}\right) \right]. \quad (5.9)$$

The column and line densities are

$$n_{\text{FD}}(x, y, t) = \frac{n_2}{\text{Li}_2(-\mathcal{F})} \text{Li}_2 \left[ -\mathcal{F} \exp\left(-\frac{x^2}{2\sigma_x(t)^2} - \frac{y^2}{2\sigma_y(t)^2}\right) \right], \quad (5.10)$$

$$n_{\text{FD}}(x, t) = \frac{n_1}{\text{Li}_{5/2}(-\mathcal{F})} \text{Li}_{5/2} \left[ -\mathcal{F} \exp\left(-\frac{x^2}{2\sigma_x(t)^2}\right) \right], \quad (5.11)$$

where  $n_2$  and  $n_1$  represent the peak column and line density, respectively. The number of atoms is obtained by

$$N = 2\pi n_2 \sigma_x(t) \sigma_y(t) \frac{\text{Li}_3(-\mathcal{F})}{\text{Li}_2(-\mathcal{F})} = \sqrt{2\pi} n_1 \sigma_x(t) \frac{\text{Li}_3(-\mathcal{F})}{\text{Li}_{5/2}(-\mathcal{F})}. \quad (5.12)$$

The temperature  $T/T_F$  is directly determined from the obtained fugacity by Eq. (2.28).

### Bose–Einstein condensates

Time evolution of the density distribution of a pure Bose–Einstein condensate released from a trap is described by

$$n_{\text{BEC}}(\mathbf{r}, t) = \frac{\mu m}{4\pi\hbar^2 a} \max\left(1 - \left(\frac{x^2}{R_x(t)^2} + \frac{y^2}{R_y(t)^2} + \frac{z^2}{R_z(t)^2}\right), 0\right), \quad (5.13)$$

where

$$R_{x,y,z}(t) = \sqrt{\frac{2\mu}{m\omega_{x,y,z}^2}} b_{x,y,z}(t). \quad (5.14)$$

Using the relation Eq. (2.19), the density distribution is written as

$$n_{\text{BEC}}(\mathbf{r}, t) = \frac{15N}{8\pi R_x(t)R_y(t)R_z(t)} \max\left(1 - \left(\frac{x^2}{R_x(t)^2} + \frac{y^2}{R_y(t)^2} + \frac{z^2}{R_z(t)^2}\right), 0\right). \quad (5.15)$$

The column and line densities are then obtained by integrating this along one- and two-dimensionally,

$$n_{\text{BEC}}(x, y, t) = \frac{5N}{2\pi R_x(t)R_y(t)} \max\left(1 - \left(\frac{x^2}{R_x(t)^2} + \frac{y^2}{R_y(t)^2}\right), 0\right), \quad (5.16)$$

$$n_{\text{BEC}}(x, t) = \frac{15N}{16R_x(t)} \max\left(1 - \frac{x^2}{R_x(t)^2}, 0\right). \quad (5.17)$$

The number of atoms in the BEC is evaluated by fitting the obtained absorption image by Eq. (5.16) or (5.17).

## 5.2 Quantum degenerate Yb–Li mixture

### 5.2.1 Zeeman slowing and magneto-optical trapping

Yb and Li atoms in a collimated atomic beam from the oven have mean velocities of  $\approx 340$  m/s and  $\approx 1500$  m/s at  $400^\circ\text{C}$ , respectively. They are first cooled and trapped by means of laser cooling techniques.

The initial cooling process is Zeeman slowing, a method to cool an atomic beam. A Zeeman slower consists of a varying-field solenoid and a near-resonant laser of the atoms. The atomic beam travels along the axis of the solenoid and the laser is shone on the atomic beam in the direction opposite to the beam's motion. Atoms in a certain velocity class are Doppler cooled by the laser beam. The solenoid produces a spatially varying magnetic field along the axis so that the Zeeman shift compensates for the change in the Doppler shift as atoms decelerate. At the exit of the slower the velocity of the atoms is reduced down to few 10 m/s. We use the  $^1\text{S}_0 \rightarrow ^1\text{P}_1$  and the  $D_2$  ( $F = 3/2 \rightarrow F' = 5/2$ ) transitions for the deceleration of Yb and Li, respectively. They are detuned by  $-440$  MHz and  $-524$  MHz from their respective resonance frequencies and superimposed by a dichroic mirror in front of the entrance window.

The atoms decelerated by the Zeeman slower are then captured in magneto-optical traps (MOTs). A MOT consists of a quadrupole magnetic field produced by a pair of coils in an anti-Helmholtz configuration and three orthogonal pairs of counter-propagating laser beams with a frequency slightly below the atomic resonance frequency. The three

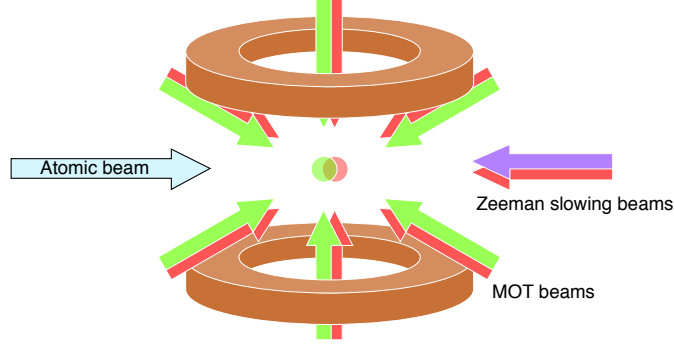


**Figure 5.1.** The configuration of the dual species Zeeman slowing and MOT of Yb and Li. An atomic beam consists of Yb and Li atoms from the oven travel along a Zeeman slower. The Zeeman slowing beams are shone on the atomic beam from the opposite direction. The beams are detuned by  $-440$  MHz from the  $^1S_0 \rightarrow ^1P_1$  resonance for Yb and by  $-524$  MHz from the  $D_2$  ( $F = 3/2 \rightarrow F' = 5/2$ ) resonance for Li. The decelerated atoms are captured in MOTs. Atoms are collected at the intersection of the MOT beams where the magnetic field produced by the MOT coils is zero. The  $^1S_0 \rightarrow ^3P_1$  transition is used for the Yb MOT and the  $D_2$  ( $F = 3/2 \rightarrow F' = 5/2$ ) and the  $D_2$  ( $F = 1/2 \rightarrow F' = 3/2$ ) transitions are used for the Li MOT.

pairs of beams intersect the center of the coils at which the field is zero. The quadrupole magnetic field causes an imbalance in the scattering forces of the laser beams and it is the radiation force that strongly confines the atoms. We use the  $^1S_0 \rightarrow ^3P_1$  transition for a Yb MOT and the  $D_2$  ( $F = 3/2 \rightarrow F' = 5/2$ ) line for cooling and the  $D_2$  ( $F = 1/2 \rightarrow F' = 3/2$ ) line for repumping of a Li MOT. These beams are superimposed by dichroic mirrors in each direction and retro-reflected after the chamber. Figure 5.1 shows the configuration of our dual species Zeeman slowing and MOT.

According to the theory of Doppler cooling, the achievable temperature by laser cooling with a laser with intensity  $I$  and a frequency detuned by  $\Delta$  from an atomic resonance is described as [113]

$$T = \frac{\hbar\Gamma}{4k_B} \frac{1 + I/I_s + (2\Delta/\Gamma)^2}{2|\Delta|/\Gamma}, \quad (5.18)$$

where  $\Gamma$  is the natural linewidth of the transition and  $I_s$  is the saturation intensity. Accordingly, a laser with a weaker intensity and a smaller detuning realizes lower temperature. When  $I \ll I_s$  and  $\Delta = -\Gamma/2$ , Eq. (5.18) takes the minimum and approaches the Doppler cooling limit

$$T_D = \frac{\hbar\Gamma}{2k_B}. \quad (5.19)$$

In our experimental sequence, the MOT for each species consists of three steps;

loading, compression, and cooling. In the loading stage each MOT has a large velocity capture range to collect as many atoms as possible by having high-power and far-detuned beams and a weak field gradient. Typically the detunings of Yb and Li MOT beams are  $-16\Gamma_{\text{Yb}}$  and  $-4\Gamma_{\text{Li}}$  (for both cooling and repumping), respectively, where  $\Gamma_{\text{Yb(Li)}}$  is the natural linewidth of the  $^1\text{S}_0 \rightarrow ^3\text{P}_1$  ( $D_2$ ) transition. The atoms in this loading stage MOT are too sparse and too hot to be transferred into an optical trap described below. In the next compression stage we ramp up the magnetic field gradient to make the confinement of the atoms tighter. This allows us to increase the density of the atoms. Also at this moment the Zeeman slower is shut off and no atoms are additionally loaded. Finally in the cooling stage we reduce the power and the detuning of the laser beams and cool the trapped atoms according to Eq. (5.18). We reduce the detunings down to  $-4\Gamma_{\text{Yb}}$  and  $-0.5\Gamma_{\text{Li}}$  and the temperatures reach a few  $10 \mu\text{K}$  and a few  $100 \mu\text{K}$  for Yb and Li, respectively, which are cold enough to transfer the atoms into the optical trap efficiently. The practical MOT procedure in the mixture production is Yb loading  $\rightarrow$  Li loading  $\rightarrow$  Yb compression and cooling  $\rightarrow$  Li compression and cooling. The order is chosen such as to have an increased field gradient in each step.

## 5.2.2 Evaporative and sympathetic cooling

The MOTs achieve a few  $10$  or  $100 \mu\text{K}$  as mentioned above, yet the atoms are still far from quantum degeneracy. They need to be much denser and colder. For tighter confinement and further cooling we load them into a crossed optical far-off-resonance trap (FORT) and perform evaporative and sympathetic cooling.

Using the polarizability  $\alpha$ , an optical dipole potential felt by a two-level atom is expressed as [114]

$$U(\mathbf{r}) = -\frac{3\pi c^2 \Gamma}{2\omega_0^3} \left( \frac{1}{\omega_0 - \omega} + \frac{1}{\omega_0 + \omega} \right) I(\mathbf{r}) \equiv -\frac{1}{4} \alpha I(\mathbf{r}), \quad (5.20)$$

where  $\Gamma$  is the natural linewidth of the transition,  $\omega_0$  is the resonance frequency of the atom,  $\omega$  and  $I(\mathbf{r})$  are the frequency and intensity of the laser light, respectively. As  $U(\mathbf{r}) \propto I(\mathbf{r})$ , the trap geometry is determined by the intensity distribution of the laser light. Potential minima correspond to maxima of the intensity with a red-detuned ( $\omega < \omega_0$ ) light and to minima of the intensity with a blue-detuned ( $\omega > \omega_0$ ) light.

The most common way is to confine atoms in the focus of a red-detuned Gaussian laser beam. The intensity distribution of a Gaussian beam propagating along the  $z$

**Table 5.1.** Transition coefficients  $C_{ab}$  for relevant transitions.

Yb		Li	
$^1S_0 \rightarrow ^1P_1$	$^1S_0 \rightarrow ^3P_1$	$D_1$	$D_2$
1	1	$\sqrt{\frac{1}{3}}$	$\sqrt{\frac{2}{3}}$

direction with power  $P$  is given by

$$I(r, z) = \frac{2P}{\pi w(z)^2} \exp\left(-\frac{2r^2}{w(z)^2}\right), \quad (5.21)$$

with the  $z$ -dependent beam waist  $w(z) = w_0\sqrt{1 + (z/z_R)^2}$ . Here  $w_0$  is the waist at the focus position and  $z_R = \pi w_0^2/\lambda$  is the Rayleigh length with the wavelength  $\lambda$ .

For a multi-level atom, polarizability of the ground state  $a$  can be written as

$$\alpha = 6\pi c^2 \sum_b C_{ab}^2 \frac{\Gamma_{ab}}{\omega_{ab}^3} \left( \frac{1}{\omega_{ab} - \omega} + \frac{1}{\omega_{ab} + \omega} \right), \quad (5.22)$$

where the summation is carried out over all electronically excited states  $b$ . The coefficient  $C_{ab}$  can be obtained as the coefficient of the reduced matrix element. It is well-known that a specific transition matrix element  $\langle J_a || e\mathbf{r} || J_b \rangle$  can be written as a product of a reduced matrix element  $\langle L_a || e\mathbf{r} || L_b \rangle$  and a real transition coefficient  $C_{ab}$  as follows;

$$\begin{aligned} \langle J_a || e\mathbf{r} || J_b \rangle &\equiv \langle L_a S_a J_a || e\mathbf{r} || L_b S_b J_b \rangle \\ &= (-1)^{J_b + L_a + 1 + S_a} \sqrt{(2J_b + 1)(2L_b + 1)} \begin{Bmatrix} L_a & L_b & 1 \\ J_b & J_a & S_a \end{Bmatrix} \langle L_a || e\mathbf{r} || L_b \rangle \quad (5.23) \\ &= C_{ab} \langle L_a || e\mathbf{r} || L_b \rangle. \end{aligned}$$

Here  $L$ ,  $S$ , and  $J$  are the orbital, spin, and total angular momenta of the state and the braces denote Wigner's 6- $j$  symbol. For the ground states of Yb and Li, it is sufficient to take into consideration the  $^1S_0 \rightarrow ^1P_1$  and  $^1S_0 \rightarrow ^3P_1$  transitions and the  $D_1$  and  $D_2$  transitions, respectively. Values of transition coefficients of these transitions are summarized in Table 5.1.

Our crossed FORT is composed of a horizontally propagating FORT (H-FORT) with a wavelength of 1070 nm and a vertical FORT (V-FORT) with 1064 nm. The polarizabilities at these wavelengths and at 532 nm, which is used for gravitational-sag compensation and an optical lattice as described below, for the ground states of Yb and Li are listed in Table 5.2. The beam waists of the H-FORT are 79  $\mu\text{m}$  in horizontal direction and 22  $\mu\text{m}$

**Table 5.2.** Polarizabilities  $\alpha/k_B$  of FORT and lattice lasers for the ground states of Yb and Li in nK/(kW/cm<sup>2</sup>). 532 nm light has a negative polarizability for Li and acts as a repulsive potential.

Wavelength	Yb( <sup>1</sup> S <sub>0</sub> )	Li( <sup>2</sup> S <sub>1/2</sub> )
1070 nm	1069.0	2402.9
1064 nm	1071.1	2420.6
532 nm	1813.1	-2468.1

vertically and that of the V-FORT is 82  $\mu$ m. The H-FORT has an elliptical shape in order to reduce a gravitational sag of Yb by having a tighter confinement in the vertical direction than the others. The atoms in MOTs are transferred into the crossed FORT after the MOT cooling phase.

We then perform evaporative cooling to reach quantum degeneracy. This well established cooling scheme is as follows; hot atoms are forced to escape from a trap by reducing the trap depth and the remaining atoms thermalize by mutual collisions, which results in a colder sample than before. Repeating this procedure, we obtain a quantum degenerate sample. Here we note that at the end of the MOT procedure, Li atoms are populated in the two lowest spin states ( $|1\rangle$  and  $|2\rangle$ ) by turning off the repumping beams 0.3 ms earlier than the cooling beams. This is because inelastic loss rates in collisions of higher spin states are so high that atoms are lost from the trap during evaporation [115].

We reduce the trap depth by decreasing the FORT powers. The initial H- and V-FORT powers are 45 W and 30 W, respectively. They are decreased down to 600 mW and 3.0 W in 9 s. Finally we obtain a mixture of a BEC of <sup>174</sup>Yb and a degenerate Fermi gas of <sup>6</sup>Li as shown in Fig. 5.2. Atom numbers of Yb and Li are  $1.4 \times 10^5$  and  $4.0 \times 10^4$ , respectively. The Fermi gas of Li equally consists of the two spin states in the ground  $F = 1/2$  state. The Li temperature is  $T_{\text{Li}} = 500$  nK and  $T_{\text{Li}}/T_{\text{F}} \approx 0.2$ , where  $T_{\text{F}}$  is the Fermi temperature. The final trapping frequencies of Yb and Li are  $(\omega_x, \omega_y, \omega_z) = 2\pi \times (69, 83, 223)$  Hz and  $2\pi \times (566, 1189, 1680)$  Hz, respectively, where the  $z$  direction is along gravity.

We note that since the applied magnetic field during the evaporative cooling is less than a few G, <sup>6</sup>Li atoms in  $|1\rangle$  and  $|2\rangle$  states are almost non-interacting as shown in Fig. 3.4 and can hardly thermalize by themselves<sup>1</sup>, while the scattering length of <sup>174</sup>Yb atoms is large enough to support frequent elastic collisions (see Table 3.7). On the other

---

<sup>1</sup>In single species experiments with <sup>6</sup>Li in other laboratories, they usually perform evaporative cooling at 300 G where the scattering length between  $|1\rangle$  and  $|2\rangle$  states is  $-330a_0$ .

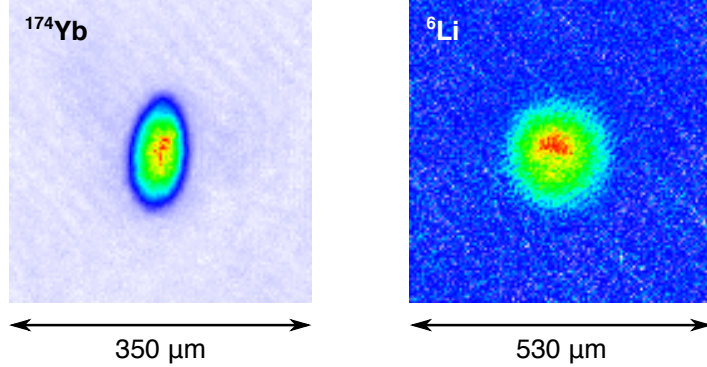


**Figure 5.2.** Time of flight absorption images of an  $^{174}\text{Yb}$  BEC and a  $^6\text{Li}$  degenerate Fermi gas. TOF times of Yb and Li are 20 ms and 1.5 ms, respectively. The numbers of atoms are  $N_{\text{Yb}} = 1.4 \times 10^5$  and  $N_{\text{Li}} = 4.0 \times 10^4$ , respectively. The Li temperature is  $T_{\text{Li}} = 500$  nK and  $T_{\text{Li}}/T_{\text{F}} \approx 0.2$ . The images are averaged over 5 measurements.

hand, the scattering length between Yb and Li is  $|a_{\text{Yb-Li}}| = 1$  nm [97], which is smaller than that of Yb but larger than Li. Therefore, the  $^6\text{Li}$  atoms are sympathetically cooled by elastic collisions with evaporatively cooled  $^{174}\text{Yb}$  atoms.

### 5.3 Gravitational-sag compensation

In mass-imbalanced atomic mixture experiments, one of the obstacles to be overcome is reduced spatial overlap due to different gravitational sags. In the vertical direction the atoms feel the gravity potential  $mgz$  in addition to the confining potential. The effect of the gravity is negligibly small in a deep trap potential. However, decreasing the trap confinement during evaporative cooling, the total potential starts to be distorted by the gravitational potential at some point and the minimum of the total potential shifts downwards. The amount of the sag depends on the mass and the trap depth. Generally a heavier atom is stronger affected than a lighter one, which results in a reduced spatial overlap between them.

Despite the strong confinement in the vertical direction by the elliptical shaped H-FORT, the Yb cloud sits about  $6.5 \mu\text{m}$  below the Li cloud at the final stage of evaporative cooling (see Fig. 5.3(b)). Here we note that our FORT potential at the end of evaporation is so shallow that the standard expression for gravitational sag assuming harmonic potentials,  $g/\omega_z^2$ , is no longer valid<sup>2</sup>. Therefore, we evaluate the sag of the Yb cloud by considering the fully Gaussian shaped FORT and the gravity potential.

<sup>2</sup>Assuming a harmonic trap for a confinement, the total potential of the trap and the gravity along

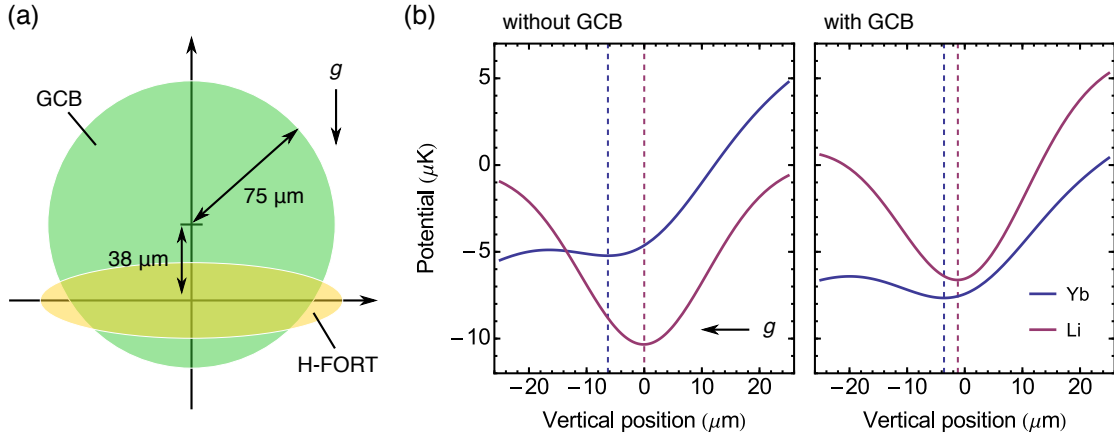


**Figure 5.3.** Calculated trapping potentials along the vertical direction. (a) Geometry of the H-FORT (yellow) and the GCB (green). The GCB has a waist of  $75 \mu\text{m}$  and is pointing about  $38 \mu\text{m}$  above the center of the H-FORT. (b) Calculated trapping potentials for Yb (blue) and Li (red) along the vertical direction at the end of evaporation without the GCB (left) and with the GCB (right). The arrow indicates the direction of gravity. The dashed lines indicate positions of potential minima in which atomic clouds settle. The Yb cloud sits  $6.5 \mu\text{m}$  below the Li cloud without the GCB. The GCB lifts the Yb cloud by about  $3 \mu\text{m}$  whereas the Li cloud barely move down by  $1 \mu\text{m}$  at a GCB power of  $900 \text{ mW}$ .

There are some ways to compensate for a reduced overlap due to different gravitational sags. One way is to use a “magic” optical dipole trap. Calculating polarizabilities Eq. (5.22) for a certain combination of species 1 and 2, one finds a wavelength which satisfies  $\alpha_1/\alpha_2 = m_1/m_2$ . In an optical trap with such a wavelength the two species obtain same amount of sags. This “magic” optical dipole trap is successfully demonstrated with Rb–K mixtures [116]. However it is inapplicable to Yb–Li mixtures, because  $\alpha_{\text{Yb}} < \alpha_{\text{Li}}$  with any red-detuned wavelengths.

Another way is to use a magnetic field gradient as in a  $^{133}\text{Cs}$ – $^6\text{Li}$  mixture reported in [117]. They compensate for the sag of Cs by applying a magnetic field gradient against the direction of gravity. Though this is applicable to Yb–Li mixtures [101], different from the Cs–Li mixture case the magnetic field gradient should be applied so as to increase the sag of Li because of magnetic-field insensitivity of Yb.

In contrast to using a magnetic field gradient, we apply an intensity gradient of a laser whose wavelength is  $532 \text{ nm}$ . The laser field acts as an attractive potential for Yb and a repulsive one for Li, because the signs of their polarizabilities are opposite (see Table 5.2). Figure 5.3(a) shows the geometrical configuration of the gravitational sag

---

the vertical direction is  $U(z) = \frac{1}{2}m\omega_z^2 z^2 + mgz = \frac{1}{2}m\omega_z^2 \left(z + \frac{g}{\omega_z^2}\right)^2 - \frac{1}{2}m\frac{g^2}{\omega_z^2}$ . Thus the amount of the sag can be evaluated by  $-g/\omega_z^2$ .

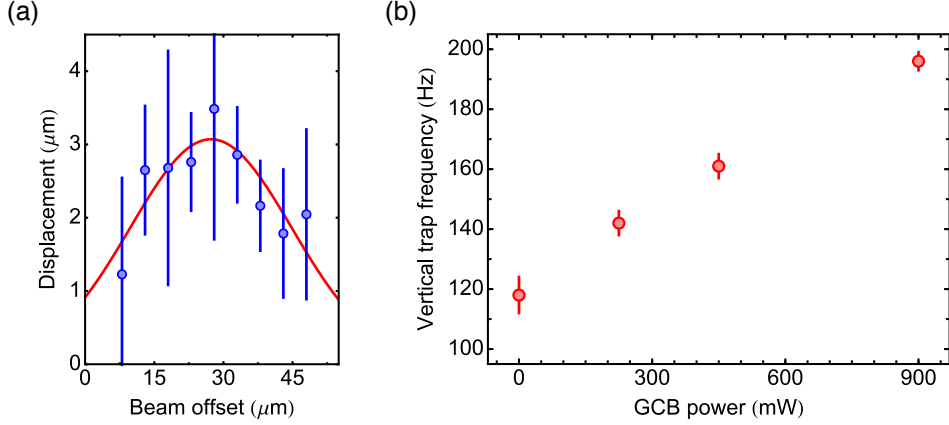


**Figure 5.4.** Effect of the GCB. (a) Vertical position displacement of the Yb cloud. Beam pointing is changed by the piezo-controlled mirror mount. The GCB power is 900 mW. The cloud is displaced by about  $3 \mu\text{m}$  at the best beam position. (b) Measured vertical trap frequencies of Yb with the GCB with various powers. The beam position is fixed at the best position determined by cloud displacement. The frequency increases as the power increases.

compensation beam (GCB) and the H-FORT. The GCB has a waist of  $75 \mu\text{m}$  and is pointing about  $38 \mu\text{m}$  above the atomic cloud. Resulting total potentials for Yb and Li in the vertical direction at a GCB power of 900 mW are shown in Fig. 5.3(b). The Yb cloud is pulled up by about  $3 \mu\text{m}$ , while Li is nearly unaffected and does not move due to its strong confinement within the FORT. 900 mW is the current limit of our laser system. However, the Li potential will also start to be seriously deteriorated at some point. As such, for the experiments at hand we think to have established a good compromise. We linearly ramp up the GCB in 100 ms followed by 100 ms holding at the end of evaporation to prevent heating and oscillations of the atomic sample.

The effectiveness of the GCB is confirmed by the displacement of the Yb cloud and the change of the vertical trap frequency. Figure 5.4 shows the vertical position displacement of the Yb cloud by the GCB. We change the pointing of the GCB by the mirror on the piezo-controlled mount (see Section 4.3). The maximum displacement is about  $3 \mu\text{m}$ , which is consistent with our calculation shown in Fig. 5.3(b). The GCB pointing is fixed at the optimal position determined by the displacement measurement.

## 5.4 Optical lattice

The next step in the experimental sequence is to load the Yb–Li quantum degenerate mixture into a 3D optical lattice with wavelength  $\lambda_L = 532 \text{ nm}$  and to form an Yb Mott

insulator. The optical lattice is adiabatically ramped up to  $15 E_R^{\text{Yb}}$  in 200 ms, where  $E_R = \hbar^2(2\pi/\lambda_L)^2/(2m)$  is the recoil energy with atomic mass  $m$ . The ratio of  $s = |V_L|/E_R$ , the lattice depth divided by the recoil energy, for Yb and Li is  $s_{\text{Yb}}/s_{\text{Li}} = 21.4$ . At  $s_{\text{Yb}} = 15$  we have  $s_{\text{Li}} = 0.7$  at which the Bloch state is well delocalized in the system. This ensures, even though at  $\lambda_L = 532$  nm their polarizabilities have opposite signs, reasonable overlap between the delocalized Li and the localized Yb atoms.

The formation of the Yb Mott insulator is confirmed by the disappearance of interference peaks in TOF absorption images of Yb atoms. Releasing a BEC from an optical lattice, one observes phase coherence of the BEC in the lattice by multiple matter wave interference peaks in a TOF absorption image. In a shallow lattice sharp peaks with a momentum  $2\hbar k$  clearly appear while in a deep lattice they vanish, indicating a quantum phase transition from a superfluid to a Mott insulator [16].

It is interesting to see how the presence of Li affects the superfluid to Mott insulator transition of Yb atoms. In a  $^{87}\text{Rb}$ – $^{40}\text{K}$  mixture in an optical lattice enhancement of localization of bosonic Rb atoms by doping with localized fermionic K atoms has been observed [22, 23]. In contrast to the Rb–K mixture system, in the Yb–Li mixture fermionic Li atoms are delocalized even in a lattice with a depth at which Yb atoms are deeply localized. The effect of the delocalized Li on the phase coherence of the Yb atoms in the lattice is unclear.

We take absorption images of Yb atoms released from the lattice with a depth ranging from 0 to  $15 E_R^{\text{Yb}}$  both in the absence and the presence of Li. We prepare a quantum degenerate mixture of a BEC of  $1 \times 10^5$  Yb atoms and a Fermi degenerate gas of  $2 \times 10^4$  Li atoms. The Li atoms are removed from the trap by applying a laser pulse resonant to the  $D_2$  line with a duration of 1 ms before ramping up the lattice in the case without Li. Figure 5.5 shows images at representative lattice depths together with illustrations of respective situations of localized Yb atoms and a delocalized Li gas in an optical lattice.

In order to quantitatively compare the two cases we evaluate visibilities of the absorption images [118]. The visibility is defined as

$$\mathcal{V} = \frac{N_{\text{max}} - N_{\text{min}}}{N_{\text{max}} + N_{\text{min}}}, \quad (5.24)$$

where  $N_{\text{max}}$  is the total number of atoms in the first order interference peaks and  $N_{\text{min}}$  is that in the diagonal areas with the same distance from the central peak (see Fig. 5.6(a)). Figure 5.6(b) shows a variation of visibility as a function of the lattice depth. No notable difference between the two cases is observed.

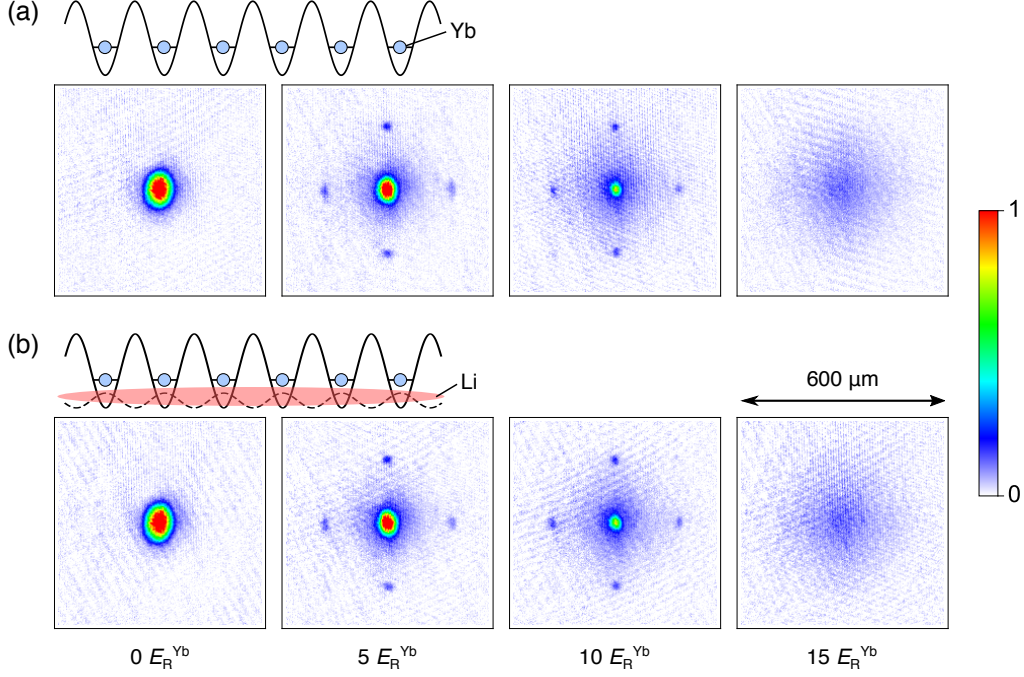


**Figure 5.5.** Absorption images of multiple matter wave interference patterns of  $^{174}\text{Yb}$  atoms after a TOF of 22 ms. The number of Yb atoms is  $N_{\text{Yb}} = 1 \times 10^5$ . Lattice depths are 0, 5, 10,  $15 E_R^{\text{Yb}}$  from left to right. The images are averaged over 5 measurements. (a) Images in the absence of  $^6\text{Li}$ . We remove Li atoms by applying a  $D_2$  resonant light pulse for 1 ms after the production of a Yb–Li quantum degenerate mixture. (b) Images in the presence of Li. The number of Li atoms is 20% of that of Yb atoms. Even though lattice sites alternate for Yb and Li (solid and dashed lines, respectively) because of the opposite signs of their polarizabilities at  $\lambda_L = 532 \text{ nm}$ , the Li atoms are delocalized enough to overlap with the localized Yb atoms due to the shallow specific potential.

Another indication for the phase coherence of a BEC in an optical lattice is the central peak width. We integrate the absorption images along the vertical direction and evaluate the full width at half maximum (FWHM) of the central peak by fitting the peak with a lorentzian function as shown in Fig. 5.6(c).

In both the visibility and the central peak width analyses no notable difference between the cases with and without Li is observed. This is in agreement with the result in a  $\lambda_L = 1064 \text{ nm}$  lattice presented in [107]. There we considered that the reduced spatial overlap would be one of the reasons for the negligible effect of the presence of Li on the phase coherence of Yb BEC in an optical lattice. However in this work we compensate for the reduced overlap by the GCB. Therefore we exclude this from possible reasons for the small effect. Instead it is attributed to the small inter-species interaction.

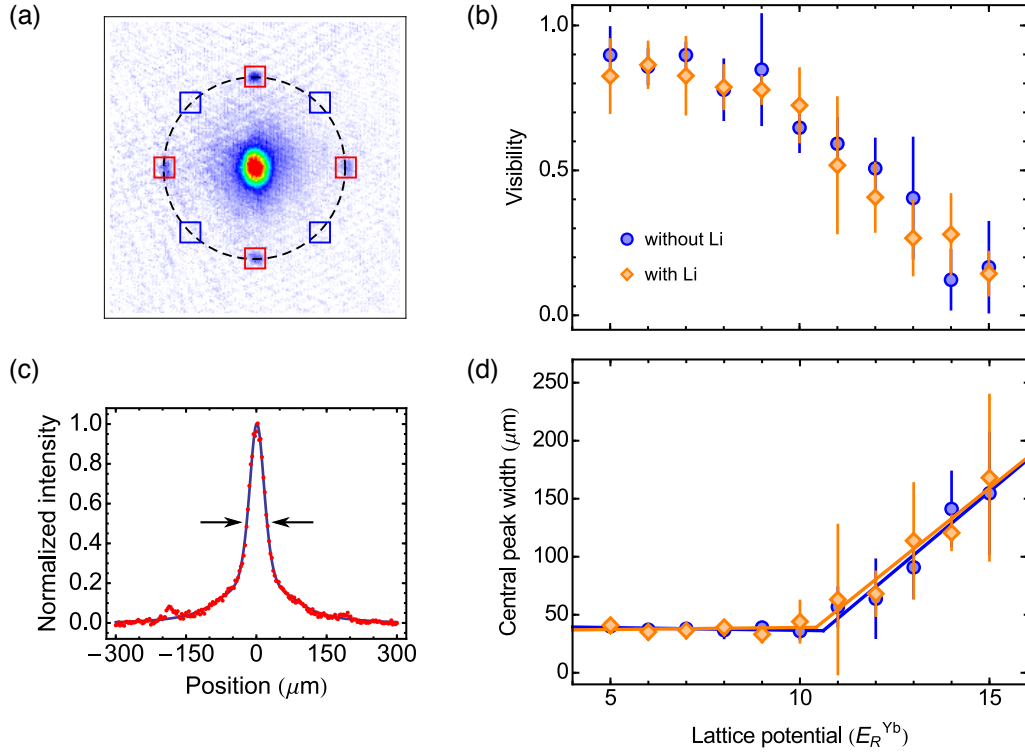


**Figure 5.6.** Quantitative analyses of TOF absorption images of Yb. (a) Evaluation of visibility. The visibility of interference fringes is defined as  $\mathcal{V} = (N_{\max} - N_{\min}) / (N_{\max} + N_{\min})$ .  $N_{\max}$  is the total atom number in red squares and  $N_{\min}$  is that in blue squares. (b) Visibility of Yb interference fringes at various lattice depths in the cases without Li (blue circle) and with Li (orange diamond). (c) Evaluation of the central peak width. We integrate the absorption images along the vertical direction and fit the central peak with a lorentzian function. The central peak width is the FWHM of the fit. (d) Central peak width at various lattice depths in the cases without Li (blue circle) and with Li (orange diamond). Solid lines denote fits with dual linear functions. No notable difference between the two cases in the visibility nor the central peak width is discerned. Error bars in (b) and (d) indicate the standard deviation of five independent measurements.

## Collisional stability of localized Yb( $^3P_2$ ) atoms immersed in a Fermi sea of Li

In this chapter, we report on the main result of the present thesis, the realization of a system of localized Yb atoms with controllable internal states immersed in a Fermi sea of Li in a three-dimensional optical lattice. In this situation we investigate inelastic losses in detail. Instead of using spin-polarized fermionic isotopes immersed in a Fermi degenerate gas of Li as in a  $^{40}\text{K}$ - $^6\text{Li}$  mixture [119], performing the experiments in a deep optical lattice and using direct excitation from the Yb ground to the excited  $^3P_2$  state, we achieve high selectivity on the collisional partners and high flexibility in the target state preparation. This method allows us to work also with bosonic Yb isotopes. Accordingly the results presented in this work provide a general survey on inelastic collisional properties of Li with one or several Yb atoms in  $^1S_0$  and  $^3P_2$  states. The results reported here are published in [120].

### 6.1 $^3P_2$ state preparation and detection

This section describes  $^3P_2$  state preparation and detection methods. A portion of the ground state Yb atoms is directly excited to the  $^3P_2$  state by a 0.1–1 ms laser pulse at a resonant wavelength of 507 nm. The Landé  $g$ -factor of the  $^3P_2$  state of  $^{174}\text{Yb}$  is  $g_J = 3/2$ . Hence, an applied magnetic bias field lifts the degeneracy of neighboring  $m_J$  sublevels by  $h \times 2.1$  MHz/G, where  $h$  is the Planck constant, and allows for  $m_J$  selective excitation

to the  $^3P_2$  state. We ramp the bias field to 282 mG for the excitation of the  $m_J = 0$  state and 200 mG for the  $m_J = -2$  state while the lattice goes from 0 to  $5 E_R$  in 100 ms. Apart from measurements comparing magnetic field dependencies the bias fields are then left unchanged until atom detection.

While the absolute value of the magnetic field is important for individual substates selectivity, the direction of the field connects to the shape of the spectrum due to the inhomogeneity of the optical potentials. In an optical trap, the excitation frequency is shifted from the bare transition frequency depending on the position as

$$h\Delta\nu(\mathbf{r}) = -\frac{1}{4}(\alpha_e - \alpha_g)I(\mathbf{r}), \quad (6.1)$$

where  $\alpha_{g(e)}$  is the polarizability of the ground (excited) state. If the difference between  $\alpha_g$  and  $\alpha_e$  is large, the excitation frequency is position sensitive, which results in a broadening of the spectrum. Particularly in the case  $\alpha_g = \alpha_e$ , inhomogeneous broadening is totally canceled, which is called a “magic wavelength” condition.

In an optical trap with a linear polarization, the polarizability of a magnetic substate  $m_J$  depends on the angle between the direction of the quantization axis and the polarization of the laser field as [121]

$$\alpha(J, m, \theta) = \alpha^S + \alpha^T(3 \cos^2 \theta - 1) \frac{3m^2 - J(J+1)}{2J(2J-1)}, \quad (6.2)$$

where  $\alpha^S$  and  $\alpha^T$  are the scalar and tensor polarizabilities, respectively. Therefore it is important to choose the field orientation for each magnetic sublevel to reduce inhomogeneous broadening. Since  $\alpha^T = 0$  when  $J = 0$  or  $1/2$  [121], the polarizability of the  $^1S_0$  state is constant. For the  $^3P_2$  state the polarizability (6.2) is reduced to

$$\alpha_e(m, \theta) = \alpha_e^S + \alpha_e^T(3 \cos^2 \theta - 1) \frac{m^2 - 2}{4}. \quad (6.3)$$

The polarizabilities of the  $^1S_0$  state are calculated by Eq. (5.22). Those of the  $^3P_2$  state are determined by spectroscopy of an Yb cloud in optical traps with various trap

**Table 6.1.** Calculated  $\alpha_g$  and measured  $\alpha_e^S$  and  $\alpha_e^T$  for 1070 nm and 532 nm light fields in units of Hz/(W/cm<sup>2</sup>).

Wavelength	$\alpha_g/h$	$\alpha_e^S/h$	$\alpha_e^T/h$
1070 nm	22.26	15.98	-13.20
532 nm	37.76	52.44	13.32

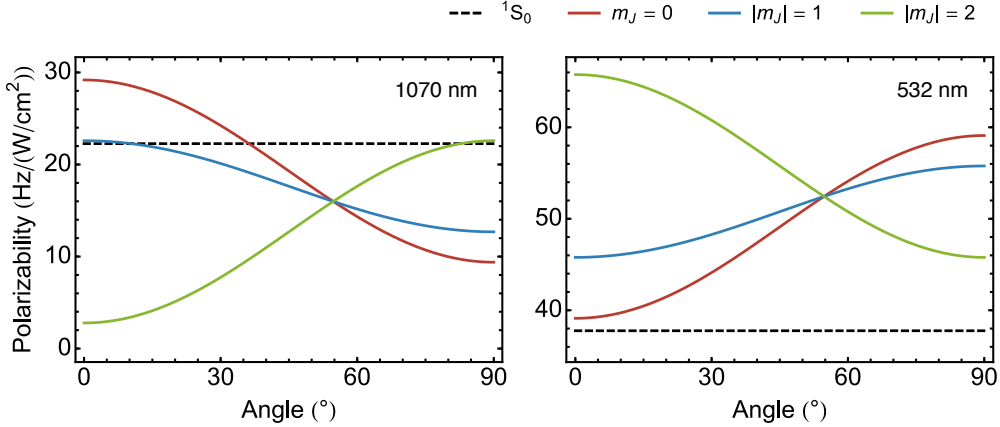


**Figure 6.1.** Polarizabilities of the  $^1S_0$  state and magnetic sublevels of the  $^3P_2$  state of  $^{174}\text{Yb}$  in 1070 nm (left) and 532 nm (right) light fields. The “magic wavelength” condition is satisfied where the polarizabilities of  $^1S_0$  and  $^3P_2$  cross.

depths. Values of calculated  $\alpha_g$  and measured  $\alpha_e^S$  and  $\alpha_e^T$  for 1070 nm and 532 nm optical traps are summarized in Table 6.1.

Using these values we obtain the angle dependences of  $\alpha_e$  for different  $m_J$  sublevels as shown in Fig. 6.1. The black dashed lines in the figure indicate the polarizabilities of the  $^1S_0$  state. The magic wavelength condition is satisfied where the  $^1S_0$  and  $^3P_2$  polarizabilities cross. Table 6.2 gives the angles at which the magic wavelength condition is satisfied. Due to the limitation of our setup, it is impossible to cancel inhomogeneous broadening by all lasers at the same time. Therefore we choose the magnetic field orientation to minimize the broadening as good as possible.

To further reduce inhomogeneous broadening the GCB is ramped down to 0 mW while the lattice goes from 10 to 15  $E_R$  in 50 ms. Since the Yb atoms are already pinned at lattice sites at 10  $E_R$ , the spatial overlap between Yb and Li remains restored even with the GCB turned off at this point.

For the detection of the  $^3P_2$  atoms, we first remove the ground state Yb atoms from

**Table 6.2.** Angles between the magnetic field and the light polarization which satisfy the magic wavelength condition. In a 1070 nm light field each magnetic sublevel has the angle, while in 532 nm there are no such angles for all sublevels.

Wavelength	$m_J = 0$	$ m_J  = 1$	$ m_J  = 2$
1070 nm	36.2°	10.2°	82.8°
532 nm	n/a	n/a	n/a

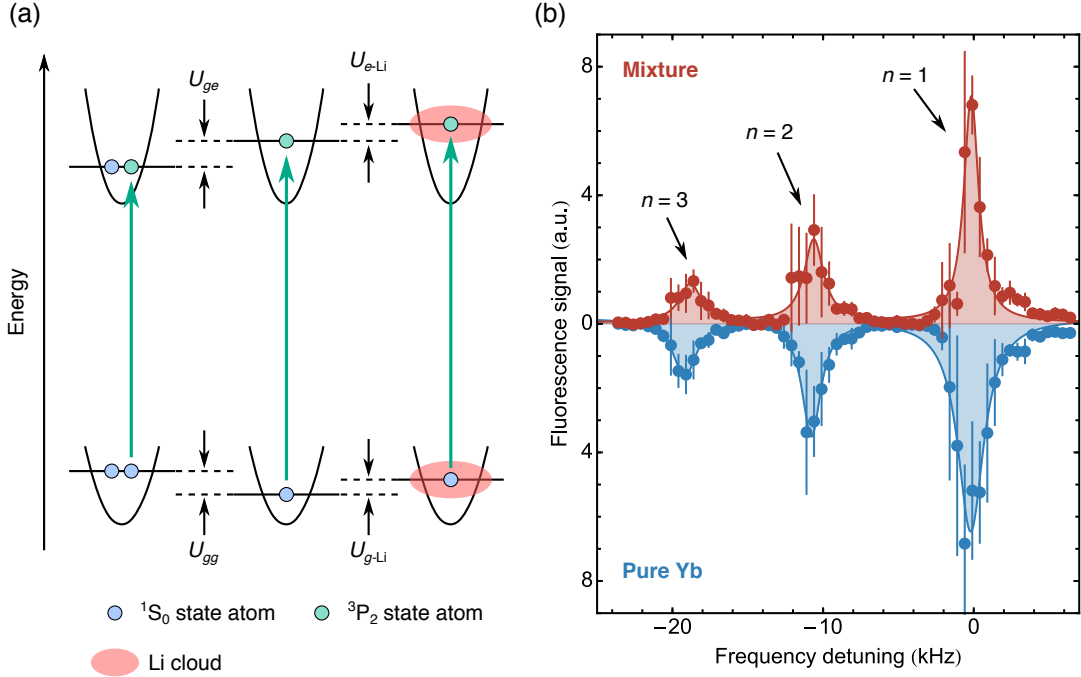


**Figure 6.2.** (a) Energy shifts of an Yb atom by inter-atomic interactions. In a doubly occupied site, a resonance frequency shift from that of an atom in a singly occupied site is  $(U_{ge} - U_{ge})/h$ , where  $U_{gg}$  and  $U_{ge}$  are the on-site interactions between two ground state Yb atoms and between ground and excited Yb atoms, respectively. The presence of Li shifts the resonance frequency by  $(U_{e-Li} - U_{g-Li})/h$ , where  $U_{g-Li}$  and  $U_{e-Li}$  represent the inter-species interactions of ground and excited Yb atoms with Li, respectively. (b) Typical  $^1\text{S}_0 \rightarrow ^3\text{P}_2(m_J = 0)$  excitation spectra of an  $^{174}\text{Yb}$  Mott insulator in an optical lattice at  $15 E_R$  with (upper) and without (lower)  $^6\text{Li}$ . The pure Yb case is inverted for ease of comparison. Resonances of single, double, and triple occupancies ( $n = 1, 2, 3$ ) in the lattice are separated due to interatomic interaction. Any significant differences between the spectra in the presence and absence of Li are not discerned. The solid lines denote the fits with Lorentzian functions for each of the resonances.

the trap by a 0.5–1 ms laser pulse resonant to the  $^1\text{S}_0 \rightarrow ^1\text{P}_1$  transition. The atoms in the  $^3\text{P}_2$  state are then repumped to the ground state via the  $^3\text{S}_1$  state by simultaneous applications of two laser pulses resonant to the  $^3\text{P}_2 \rightarrow ^3\text{S}_1$  and  $^3\text{P}_0 \rightarrow ^3\text{S}_1$  transitions with a duration of 1 ms (see Fig. 3.5).

Finally, the atoms returned to the ground state are recaptured by a detection MOT operating on the strong  $^1\text{S}_0 \rightarrow ^1\text{P}_1$  transition. The fluorescence intensity from the MOT is detected and is proportional to the number of repumped atoms. Figure 6.2 shows a typical  $^1\text{S}_0 \rightarrow ^3\text{P}_2(m_J = 0)$  excitation spectrum of the Yb Mott insulator at  $15 E_R$  immersed in a Fermi degenerate gas of Li. The formation of a Mott insulator state is

reflected by the spectrum with well-resolved resonance peaks shifted by on-site interactions [78]. We note that the corresponding spectrum taken without Li (lower panel, inverted) is basically identical, in agreement with previous observations [107]. The width of the  $n = 1$  peak, 1 kHz, together with our Li density, results in an upper bound for the  $s$ -wave scattering length difference as  $|a_{e\text{-Li}} - a_{g\text{-Li}}| < 40$  nm (see Appendix B). In the measurements below, we selectively excite Yb atoms in singly, doubly, and triply occupied ( $n = 1, 2, 3$ ) sites by properly setting the excitation laser frequency.

## 6.2 Yb( $^3P_2$ )–Li inelastic collisions

We measure the loss of Yb( $^3P_2, m_J = 0$ ) atoms by inelastic collisions with Li. The experimental procedure is as follows; after the lattice depth reaching  $15 E_R$  the 507 nm excitation pulse resonant to Yb singly occupied ( $n = 1$ ) lattice sites is applied. Remaining ground state Yb atoms are removed by  $^1S_0 \rightarrow ^1P_1$  resonant light as described above. This procedure allows us to exclude unwanted Yb( $^3P_2$ )–Yb( $^3P_2$ ) and Yb( $^3P_2$ )–Yb( $^1S_0$ ) collisions that have shown to have large inelastic loss rates on the order of  $10^{-11}$  and  $10^{-12}$  cm $^3$ /s, respectively [93]. It is also important to note that the number of excited atoms is less than 10% of that of Li so that the Li density can be considered constant during the interaction time. After a variable holding time of the Yb( $^3P_2$ )–Li mixture in the lattice we detect the Yb atoms remaining in the  $^3P_2$  state. Li atoms are detected by absorption imaging at the same time. For comparison, we repeat the identical experimental sequence for a sample without Li, where Li atoms are removed from the trap by applying a laser pulse resonant to the Li  $D_2$  line with a duration of 1 ms before loading the lattice.

The result is shown in Fig. 6.3(a). A fast decay of Yb( $^3P_2$ ) atoms by the collision with Li is clearly observed. Fits to the data with exponential functions give decay time constants of  $\approx 15$  ms and  $\approx 1000$  ms for the cases with and without Li, respectively. To determine the Yb( $^3P_2, m_J = 0$ )–Li inelastic loss coefficient, we repeat the measurement with various Li densities by changing either GCB intensities or the total number of Li atoms. We vary the GCB power between 0–900 mW and the total Li atom number between  $8\text{--}73 \times 10^3$  by changing the initial Li loading time. In the former case the Li number is  $3.0 \times 10^4$  and in the latter case the GCB power is fixed at 900 mW. Results with representative GCB powers are shown in Fig. 6.3(b). The atoms decay faster as GCB power increases. This also indicates the effectiveness of our GCB approach in which it lifts the Yb cloud up to the denser regions of the Li cloud. Figure 6.3(c) shows results

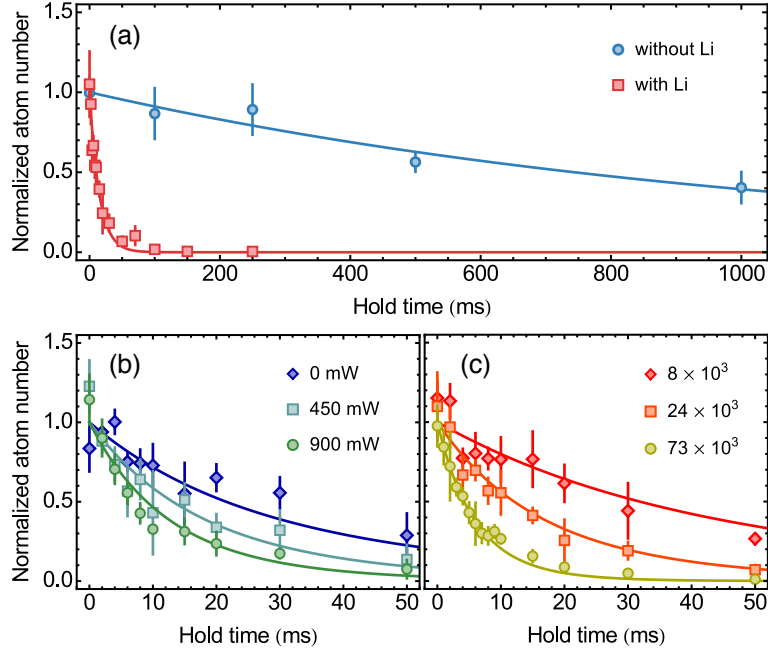


**Figure 6.3.** (a) Time evolutions of  $\text{Yb}(^3\text{P}_2, m_J = 0)$  atoms with and without Li. The GCB power and the total number of Li are 900 mW and  $2.5 \times 10^4$ , respectively. A stronger decay in the presence of Li is clearly observed. Fits by exponential functions (solid lines) give decay time constants of  $\approx 15$  ms and  $\approx 1000$  ms, respectively. Inelastic decays of  $\text{Yb}(^3\text{P}_2)$  atoms (b) at various GCB powers with  $3.0 \times 10^4$  Li atoms, and (c) with various total numbers of Li at 900 mW GCB power. The decays become faster as Li density increases. Solid lines denote fits to the data (see text). The applied bias field is 282 mG in all cases. Error bars indicate the standard deviation of three independent measurements.

with representative total numbers of Li atoms. Faster decay with more Li atoms is clearly discerned.

We fit the datasets and determine the inelastic loss coefficient in the following way. In the absence of  $\text{Yb}(^3\text{P}_2)\text{--}\text{Yb}(^3\text{P}_2)$  and  $\text{Yb}(^3\text{P}_2)\text{--}\text{Yb}(^1\text{S}_0)$  collisions thanks to the optical lattice and the occupancy selective excitation scheme, the decay of  $\text{Yb}(^3\text{P}_2)$  atoms is described by the  $\text{Yb}(^3\text{P}_2)\text{--}\text{Li}$  inelastic decay term as a dominant process;

$$\dot{n}_{\text{Yb}} = -\alpha n_{\text{Yb}} - \beta \xi n_{\text{Li}} n_{\text{Yb}}, \quad (6.4)$$

where  $n_{\text{Yb}}$  and  $n_{\text{Li}}$  are the density of  $\text{Yb}(^3\text{P}_2)$  and Li, respectively,  $\alpha$  is the one-body loss rate, and  $\beta$  is the  $\text{Yb}(^3\text{P}_2)\text{--}\text{Li}$  inelastic loss coefficient averaged over the two contributing Li spin states. Here we assume that higher than two-body collisions are negligible.

We have further introduced a Li density correction factor  $\xi$ . It accounts for the reduced density of the Li Bloch wave function at Yb sites for a lattice depth of  $s_{\text{Li}} = 0.7$  (see Fig. 6.4(a)). The correction factor  $\xi$  is determined by the three dimensional overlap

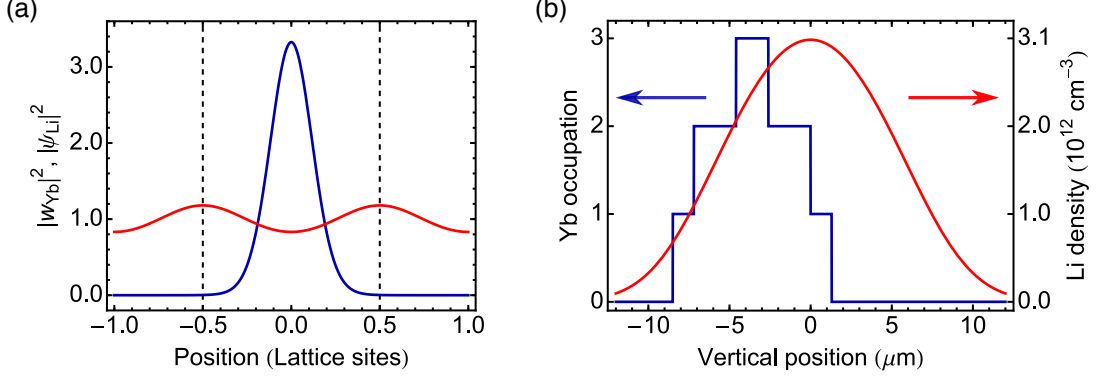


**Figure 6.4.** (a) The Wannier state of Yb (blue) and the Bloch state of Li (red) at  $s_{\text{Yb}}(s_{\text{Li}}) = 15(0.7)$ . The density correction factor  $\xi$  is determined by the overlap integral of them in a single lattice site (between  $-0.5$  and  $0.5$  lattice sites). (b) Mott shell structure of the Yb ground state (blue) and density distribution of Li (red) along the vertical direction. Examples with  $N_{\text{Yb}} = 1.0 \times 10^5$  and  $N_{\text{Li}} = 2.5 \times 10^4$  at GCB power 900 mW are displayed. The Yb( $^3P_2$ ) atoms can be assumed to be equally distributed in the  $n = 1$  Mott shell volume, because we selectively excite the atoms in the  $n = 1$  shell.

integral of the Wannier state of Yb and the Bloch state of Li in a single lattice site;

$$\xi = \int_{-d/2}^{d/2} |w_{\text{Yb}}(r)|^2 |\psi_{\text{Li}}(r)|^2 d^3r. \quad (6.5)$$

Here  $w_{\text{Yb}}$  is the Wannier state of Yb,  $\psi_{\text{Li}}$  is the Bloch state of Li, and  $d = 266$  nm is the lattice spacing. Evaluating the Yb Wannier function we include that the lattice depth for Yb( $^3P_2$ ) in each direction is slightly different due to the dependence of its polarizability on the angle between the magnetic field orientation and the laser polarization. For the  $m_J = 0$  state the correction factor is calculated to be  $\xi = 0.66$ .

Considering the number of Yb( $^3P_2$ ) is less than 10% of that of Li atoms, we regard  $n_{\text{Li}}$  as time independent as mentioned above. Therefore, the time evolution of the number of Yb( $^3P_2$ ) is expressed as

$$N_{\text{Yb}}(t) = \int n_{\text{Yb}}(r, t = 0) e^{-(\alpha + \beta \xi n_{\text{Li}}(r))t} d^3r. \quad (6.6)$$

Figure 6.4(b) shows a typical Mott shell structure of the Yb ground state and a density distribution of Li along vertical direction with GCB power 900 mW. Since we selectively excite Yb atoms in the  $n = 1$  Mott shell, we assume that the Yb( $^3P_2$ ) atoms are equally distributed in  $n = 1$  shell volume. The one-body loss rate is determined to be  $1/\alpha = (900 \pm 250)$  ms from the fit to the data without Li. We evaluate  $\beta$  using a bootstrap method. All datasets are fitted 100 times by Eq. (6.6) with  $\beta$  being a common parameter among them. Each time the Li cloud size, the numbers of Yb and Li, and the

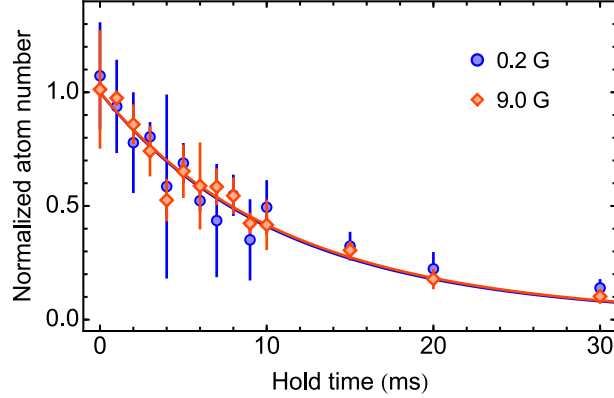


**Figure 6.5.** Inelastic decays of  $\text{Yb}(^3\text{P}_2, m_J = -2)$  with Li at 200 mG and 9.0 G. Solid lines are fits to the data with Eq. (6.6). Both decay curves are rather identical. This does not support the previous theoretical prediction of a FR at around 10 G.

Yb vertical position are randomly chosen in the ranges of  $\pm 10\%$  (roughly corresponds to Li temperatures  $\pm 150$  nK),  $\pm 10\%$ , and  $\pm 0.5 \mu\text{m}$ , respectively. The mean and the standard deviation of the fit results yield  $\beta = (4.4 \pm 0.3) \times 10^{-11} \text{ cm}^3/\text{s}$  for the  $m_J = 0$  state. Solid lines in Fig. 6.3(b) and (c) show the fit results.

For the determination of the inelastic loss coefficient for the  $m_J = -2$  state, possible contributions from both  $n = 1$  and 2 shells are included. They arise from excitation uncertainties caused by small intra-species interaction in combination with a significant sensitivity to magnetic field noise of this state. Our error budget accounts for this by also allowing partial to full excitation in the  $n = 2$  shell in the bootstrap analysis. The analysis with  $\xi = 0.64$  results in  $\beta = (4.7 \pm 0.8) \times 10^{-11} \text{ cm}^3/\text{s}$ . This value is two orders of magnitude smaller than that predicted in [38] and better matches the prediction in [34]. In the former report, the authors also predict an increase of  $\beta$  with a  $^{174}\text{Yb}(^3\text{P}_2, m_J = -2)$ - $^6\text{Li}$  FR at around 10 G, while the latter predicts a decrease of  $\beta$  for 0–50 G. To check these, we compare the decays of  $\text{Yb}(^3\text{P}_2, m_J = -2)$  at magnetic fields of 200 mG and 9.0 G (Fig. 6.5). The magnetic field is swept to the desired value in 1 ms after the excitation. The experimentally obtained decay curves at both magnetic fields are almost identical, highlighting the continuing challenges in a theoretical treatment of the problem. Our result provides additional input to refine the required inter-atomic potentials.

To give further insight into the  $\text{Yb}(^3\text{P}_2)$ -Li inelastic collisions, we investigate the inelastic decay channels of the  $^3\text{P}_2$  atoms by collisions with Li. Possible decay processes are spin changing, fine structure changing, and principal quantum number changing collisions. Considering energy and momentum conservation in  $\text{Yb}(^3\text{P}_2)$ -Li inelastic col-

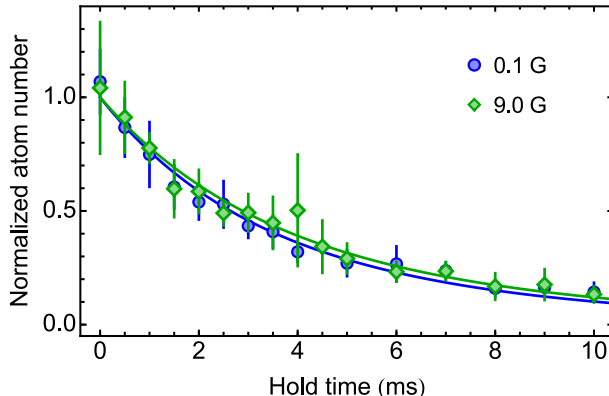


**Figure 6.6.** Inelastic decay of  $\text{Yb}(^3\text{P}_2, m_J = 0)$  with Li at 100 mG and 9.0 G. Solid lines are fits to the data with Eq. (6.6). No differences are observed below and above the threshold magnetic field 500 mG. This excludes spin changing collision dominance in the  $\text{Yb}(^3\text{P}_2)$ –Li inelastic collisions.

lisions, a decayed Yb atom carries away only  $m_{\text{Li}}/(m_{\text{Li}} + m_{\text{Yb}}) \approx 3\%$  of the released energy. If spin changing collisions dominantly occur, there is a magnetic field threshold beyond which  $^3\text{P}_2(m_J > -2)$  atoms in the process  $m_J \rightarrow -2$  gain more energy (3% of the magnetic field dependent Zeeman splitting) than the lattice and FORT support. As a result, we would expect faster decays of  $m_J > -2$  states at higher magnetic fields.

The lattice depths for all the sublevels of the  $^3\text{P}_2$  state are 1–1.4 times deeper than that for the  $^1\text{S}_0$  state due to their polarizabilities depending on the direction of the quantization axis. Since the Zeeman splitting of the  $^3\text{P}_2$  state of  $^{174}\text{Yb}$  is  $k_B \times 100 \mu\text{K}/\text{G}$  per  $\Delta m_J = 1$ , the threshold is—taking also into account that only 3% of the collisional energy are transferred onto Yb—in the range of 500–700 mG for  $m_J = 0$  at a lattice depth of  $15 E_R = k_B \times 2.9 \mu\text{K}$  for the  $^1\text{S}_0$  state. We compare the  $\text{Yb}(^3\text{P}_2, m_J = 0)$  decays at 100 mG and 9.0 mG (Fig. 6.6). We do not find any significant differences between the two cases. Therefore, we conclude that the decay of  $\text{Yb}(^3\text{P}_2)$  by inelastic collisions with Li at low magnetic field is dominated by fine structure changing or principal quantum number changing collisions.

### 6.3 Site-occupancy selective loss measurements

Besides the  $\text{Yb}(^3\text{P}_2)$ –Li inelastic collision measurements, we demonstrate that our method using an optical lattice and a direct excitation allows us to study collisional processes site-occupancy selectively. First, we measure the decay of  $^3\text{P}_2$  state atoms in doubly occupied ( $n = 2$ ) sites. By selectively exciting Yb atoms in  $n = 2$  sites to the  $^3\text{P}_2$

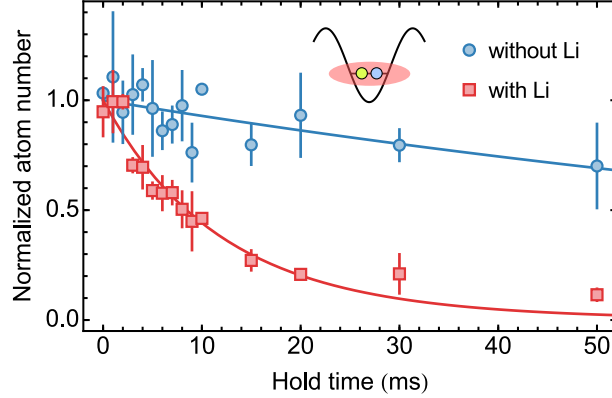


**Figure 6.7.** Time evolutions of  $\text{Yb}(^3\text{P}_2, m_J = -2)$  in  $n = 2$  sites at 200 mG. The solid lines denote fits to the data with an exponential function for the data without Li and with Eq. (6.6) for the data with Li. Any particular behavior in a  $\text{Yb}(^3\text{P}_2)$ – $\text{Yb}(^1\text{S}_0)$  system with Li is not confirmed. Inset: Sketch of the situation. In a single lattice site  $\text{Yb}(^1\text{S}_0)$  (blue),  $\text{Yb}(^3\text{P}_2)$  (yellow), and delocalized Li (red) interact.

state,  $\text{Yb}(^3\text{P}_2)$ – $\text{Yb}(^1\text{S}_0)$  inelastic collisions become detectable while  $\text{Yb}(^3\text{P}_2)$ – $\text{Yb}(^3\text{P}_2)$  and higher order collisions are inhibited. We use the  $m_J = -2$  state that is stable against inelastic collision with  $\text{Yb}(^1\text{S}_0)$  [93]. The experimental procedure is as in the above measurements apart from the absence of the  $\text{Yb}(^1\text{S}_0)$  blast pulse before having the holding time.

The result is shown in Fig. 6.7 together without the case with Li for comparison. The decay model is described by Eq. (6.6) with  $\alpha$  modified by the collision with  $\text{Yb}(^1\text{S}_0)$  atoms. From an exponential fit to the data without Li,  $\alpha$  is determined to be  $1/\alpha = (135 \pm 20)$  ms in agreement with the previous result in [93]. The fit to the data with Li by Eq. (6.6) yields  $\beta = (5.4 \pm 1.0) \times 10^{-11}$  cm<sup>3</sup>/s, a value similar to the one obtained above for  $\text{Yb}(^3\text{P}_2, m_J = -2)$ –Li collisions in absence of  $\text{Yb}(^1\text{S}_0)$  atoms. This demonstrates that the Li-induced inelastic decay of the two-atom state of  $\text{Yb}(^1\text{S}_0)$ + $\text{Yb}(^3\text{P}_2)$  can be approximated reasonably by assuming Li to only affect the  $\text{Yb}(^3\text{P}_2)$  atoms.

To complete the picture, we also investigate by selective excitation the time evolutions of only ground state Yb atoms in singly, doubly, and triply occupied lattice sites separately. We have a variable hold time at  $15 E_R$  and then measure for each occupation number the remaining number of sites by site-occupancy selective excitation to the  $m_J = 0$  state. Here we note that since our excitation method excites only one of the atoms in each lattice site, not the number of atoms but the number of sites is measured.

The results are shown in Fig. 6.8. An increase of the number of singly occupied sites and decays of those of doubly and triply occupied sites are observed. The observed

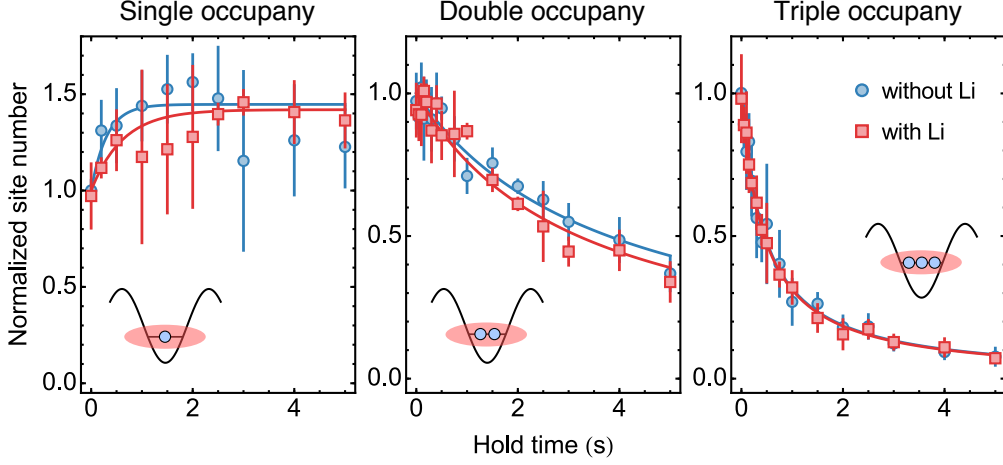


**Figure 6.8.** Time evolutions of the number of singly, doubly, and triply occupied sites at 282 mG measured by site-occupancy selective excitation. The number of  $n = 1$  sites increases by about 50% in a few seconds. Decays of  $n = 2$  and 3 sites are observed. Note that while in the previous experiments the relevant dynamics was in the range of milliseconds, the current experiment with ground state atoms only is on the order of seconds. These behaviors should be related not only to three-body decay processes but also to complication of tunneling and on-site interactions. In any occupation order, no notable differences between the cases of presence and absence of Li are observed. Solid lines are guides to the eye.

behaviors should be attributed to an intricate dynamics where tunneling and interaction interplay as well as three-body decays. In the case of singly and doubly occupied sites the dynamics is likely to be dominated by redistribution of the site occupation by hopping and due to heating effects induced by the lattice beams. In triply occupied sites molecule formation also becomes possible. In contrast to the systems including  $\text{Yb}(^3\text{P}_2)$  atoms, notable differences between the cases with and without Li are not observed in any occupation order. This proves in agreement to our previous results that in the Yb ground state the intra-species collisional properties are not significantly altered by the presence of Li.



## Conclusions and outlook

### Conclusions

In this work we realized a system of localized Yb atoms with controllable internal states immersed in a Fermi sea of Li. First we developed a compensation method for a reduced spatial overlap between Yb and Li atomic clouds due to different gravitational sags. By applying an intensity gradient of a 532 nm beam onto the atomic clouds, Yb atoms are pulled up and Li atoms are pushed down a bit. About a  $3\mu\text{m}$  displacement of an Yb cloud was observed, which indicates the effectiveness of the compensation beam.

We then loaded a quantum degenerate  $^{174}\text{Yb}$ - $^6\text{Li}$  mixture into a three-dimensional optical lattice with a wavelength of 532 nm. A superfluid to Mott insulator transition of Yb both in the absence and presence of Li atoms was successfully observed. It was confirmed that the phase coherence of an Yb BEC and a  $^3\text{P}_2$  spectrum of an Yb Mott insulator were almost unaltered by the presence of Li even with the reduced overlap compensated. This is in agreement with previous observations in a 1064 nm optical lattice [107]. Also by the direct excitation of localized Yb atoms from the ground to the excited  $^3\text{P}_2$  state, we realized localized metastable Yb atoms. This together with the mobile Li atoms marks the first experimental realization of having localized metastable Yb atoms immersed in a Fermi sea of Li, the main goal of the present research.

Combining a deep optical lattice and a direct excitation to the  $^3\text{P}_2$  state, we investigated Yb( $^3\text{P}_2$ )-Li inelastic collisional properties in detail. The  $^{174}\text{Yb}(^3\text{P}_2)$ - $^6\text{Li}$  inelastic

loss coefficients for  $m_J = 0$  and  $-2$  states were determined to be  $(4.4 \pm 0.3) \times 10^{-11} \text{ cm}^3/\text{s}$  and  $(4.7 \pm 0.8) \times 10^{-11} \text{ cm}^3/\text{s}$ , respectively. The obtained inelastic loss rate of  $m_J = -2$  and its magnetic field dependence should provide stimulus to further improve current calculations on the Yb( $^3\text{P}_2$ )–Li Feshbach resonance landscape. The observed magnetic field independence of the inelastic loss rate for  $m_J = 0$  implies little contribution of spin changing processes to the decay of Yb( $^3\text{P}_2$ ) in collisions with Li.

Our method also allows us to investigate decays of atoms in one- or few-body systems separately. In fact, we measured the time evolution of Yb( $^3\text{P}_2$ ) in  $n = 2$  sites, and we found that the Li-induced inelastic decay of the two-atom state of Yb( $^1\text{S}_0$ )+Yb( $^3\text{P}_2$ ) is well understood by the Li atoms affecting solely the Yb( $^3\text{P}_2$ ) state. Further we successfully observed time evolutions of ground state Yb atoms in  $n = 1, 2$ , and 3 sites separately and confirmed absence of the effect of Li on the intra-species collisional properties.

In addition to the realization of metastable Yb in the Fermi sea of Li we could also get a rather complete picture on the interaction between the two species. The inelastic collisions are characterized in type and quantity and for the elastic collisions an upper boundary could be established. This is the foundation for the next series of experiments to try to get control over the inter-species interactions.

## Outlook

The experimental method presented in this work can serve as a tool in the search for Yb( $^3\text{P}_2$ )–Li Feshbach resonances by measuring variations of inter-species inelastic loss rates over a wide range of magnetic fields (see Appendix B). Also it is applicable to other isotopes. Especially, fermionic Yb isotopes ( $^{171}\text{Yb}$  and  $^{173}\text{Yb}$ ) are interesting candidates to search for inter-species Feshbach resonances, where both usual and anisotropy-induced Feshbach resonances are expected to exist because of their hyperfine structures in the  $^3\text{P}_2$  states. We plan to also make use of high-resolution spectroscopy on the  $^1\text{S}_0 \rightarrow ^3\text{P}_2$  transition to measure scattering lengths between Yb( $^3\text{P}_2$ ) and Li at eventually confirmed Feshbach resonances as performed in [29, 30] (see Appendix B).

Once we find a usable Yb( $^3\text{P}_2$ )–Li Feshbach resonance, we can address impurity problems. Especially, Anderson’s orthogonality catastrophe (OC) would be an interesting topic [32, 122–124]. In our setup localized impurity Yb atoms can be switched from almost non-interacting to strongly-interacting with a Li Fermi sea by exciting them from the ground to the excited  $^3\text{P}_2$  state. OC of the Fermi sea by the suddenly introduced

---

local impurities can be seen by Ramsey-interference and spin-echo type measurements of the impurities [32]. This kind of experiment has been performed for non-localized impurity atoms in the context of polarons [125, 126], but not for localized impurities as Anderson's OC.

Also coherent manipulation of Yb atoms immersed in a spin mixture of Li allows us to demonstrate deterministic quantum computation with one clean qubit (DQC1) [127], which can solve some computationally hard problems.

Another interesting research direction is physics in mixed dimensions. Atoms living in different dimensions show interesting scattering properties including confinement-induced resonances. Several theoretical studies have been carried out for 1D–3D or 2D–3D mixtures of Bose–Fermi or Fermi–Fermi mixtures [128–131]. However there is only a few experimental works on those mixed dimensional systems and confinement induced resonances [132, 133]. As already seen in this thesis, Yb atoms can be subjected to low dimensions while Li remains a three-dimensional gas in an optical lattice. Mixed dimensional physics is an accessible research area with Yb–Li mixtures.





## Optical pumping of ${}^6\text{Li}$

If a Feshbach resonance between  $\text{Yb}({}^3\text{P}_2)$  and  $\text{Li}$  exists, the spin state involved in the resonance is only one spin component of each species. We can prepare a single component of the  ${}^3\text{P}_2$  state by the direct excitation to each sublevel. For  $\text{Li}$  atoms, we need another trick to polarize the spin component of the ground state. Here we present the optical pumping method to prepare a spin-polarized  $\text{Li}$  sample.

Figure A.1(a) illustrates the scheme to optically pump to the  $m_F = +1/2$  state in  $F = 1/2$ . Initially,  $\text{Li}$  atoms consists of the  $m_F = \pm 1/2$  states equally. Applying a laser resonant to the  $D_1(F = 1/2 \rightarrow F' = 1/2)$  line with the  $\sigma^+$  polarization, atoms in  $m_F = -1/2$  in  $F = 1/2$  are excited to  $m_{F'} = +1/2$  of the  ${}^2\text{P}_{1/2}(F' = 1/2)$  state and immediately decay to either  $m_F = -1/2, +1/2, +3/2$  in  $F = 1/2$  and  $F = 3/2$ . At the same time, unpolarized  $D_2(F = 3/2 \rightarrow F' = 3/2)$  resonant light is applied. This light excites atoms in all spin states of  $F = 3/2$  to the  ${}^2\text{P}_{3/2}$  state. The excited atoms can decay to all spin states in the  ${}^2\text{S}_{1/2}$  state. Since only the  $m_F = +1/2$  state in  $F = 1/2$  becomes the dark state, atoms are in the end pumped to this state. Pumping to  $m_F = -1/2$  can be done by using the  $\sigma^-$  polarization  $D_1$  light.

Similarly, atoms can be pumped to either  $m_F = \pm 3/2$  state in  $F = 3/2$  (Fig. A.1(b)). In this case we use lasers resonant to the  $D_1(F = 3/2 \rightarrow F' = 3/2)$  and  $D_2(F = 1/2 \rightarrow F' = 3/2)$  lines.

The laser source for the  $D_1$  resonant light is a Littman configuration ECLD. Its frequency is locked to the transfer cavity (see Fig. 4.13). The applied beam power is 300–500  $\mu\text{W}$  and the beam diameter is 2 cm. The  $D_2$  resonant light is the same as used

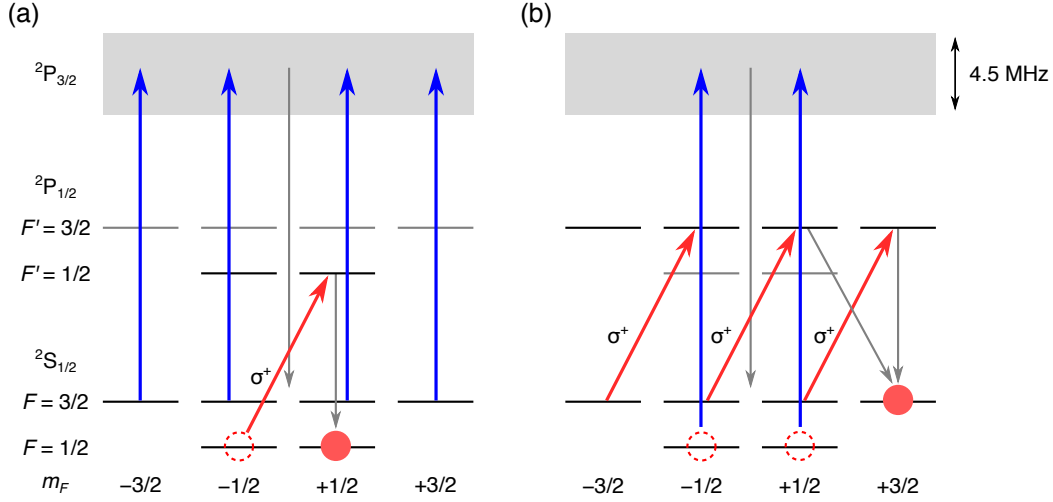


**Figure A.1.** Optical spin pumping of  ${}^6\text{Li}$ . (a) Pumping to  $m_F = +1/2$  in the  $F = 1/2$  state is carried out by simultaneous applications of a  $D_1(F = 1/2 \rightarrow F' = 1/2)$  resonant light with  $\sigma^+$ -polarization and an unpolarized  $D_2(F = 3/2 \rightarrow F' = 3/2)$  resonant light. Pumping to  $m_F = -1/2$  can be done by using  $\sigma^-$  polarized  $D_1$  light. (b) Similarly to the  $m_F = \pm 1/2$  case, we can pump atoms to either  $m_F = \pm 3/2$  state of the  $F = 3/2$  state. Pumping lasers are resonant to the  $D_1(F = 3/2 \rightarrow F' = 3/2)$  and  $D_2(F = 1/2 \rightarrow F' = 3/2)$  lines.

for the MOT cooling or repumping beams. A pumping pulse of 0.5 ms duration is applied 2 s after evaporative cooling starts to prevent atoms heated by the pumping process to leave the still relatively deep optical trap.

The pumping is confirmed by the Stern–Gerlach method. Applying a magnetic field gradient during TOF, different spin states feel different external forces during the expansion and they are spatially separated. Figure A.2 shows Stern–Gerlach TOF images. Without spin pumping, an atomic sample is an almost equal spin mixture of  $|1\rangle$  and  $|2\rangle$ . Figure A.2(b–e) present results of pumping to the  $|1\rangle$ ,  $|2\rangle$ ,  $|3\rangle$ , and  $|6\rangle$  states, respectively and confirms the effectiveness of our optical pumping scheme.

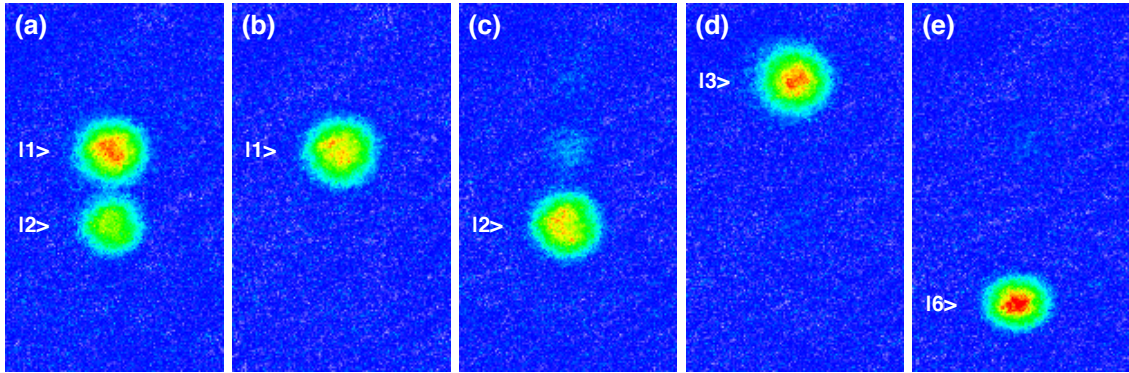


**Figure A.2.** Spin resolved absorption images by the Stern–Gerlach technique. A magnetic field gradient is applied during 1.2 ms expansion time. (a) Unpolarized  ${}^6\text{Li}$  sample. (b–e) Samples spin-polarized to the  $m_F = +1/2$  and  $-1/2$  in the  $F = 1/2$  state and  $m_F = -3/2$  and  $+3/2$  in the  $F = 3/2$  state, respectively. The images are averaged over 5 measurements.



## Feshbach resonance search

This appendix presents preliminary results of our search for Feshbach resonances between Yb( $^3P_2$ ) and Li. First we measure inelastic loss coefficients for a wide range of magnetic fields to locate resonances. An increase of the inelastic loss coefficient is expected around a resonance (see Section 2.4). We then perform  $^1S_0 \rightarrow ^3P_2$  spectroscopy of Yb around the magnetic field at which an increase of the inelastic coefficient is observed. This enables us to directly measure the change of the Yb( $^3P_2$ )–Li scattering length at the applied magnetic field.

### B.1 Inelastic loss coefficients

We measure inelastic coefficients of various combinations of spin states of  $^{174}\text{Yb}(^3P_2)$  and  $^6\text{Li}(^2S_{1/2})$  for 40–800 G. The experimental procedure is similar to the one presented in Section 6.2. First we produce a quantum degenerate mixture of Yb( $^1S_0$ ) and spin-polarized Li( $^2S_{1/2}$ ). We can prepare either  $|1\rangle, |2\rangle, |3\rangle$ , or  $|6\rangle$  spin state of Li (see Appendix A). The mixture sample is then loaded into a three-dimensional lattice at  $15 E_R^{\text{Yb}}$ . A portion of the Yb atoms in the singly occupied sites are excited to the  $^3P_2$  state at 200 mG in the lattice and the remaining ground state atoms are removed from the trap by a blast pulse.

Then the magnetic field is ramped to the desired value. Due to the limitation of the coils to generate high fields (Feshbach coils), it takes several ms for the coils to stably reach the set value. The ramping time is 4 ms for  $B \leq 500$  G, 6 ms for  $B \leq 600$  G, 8 ms

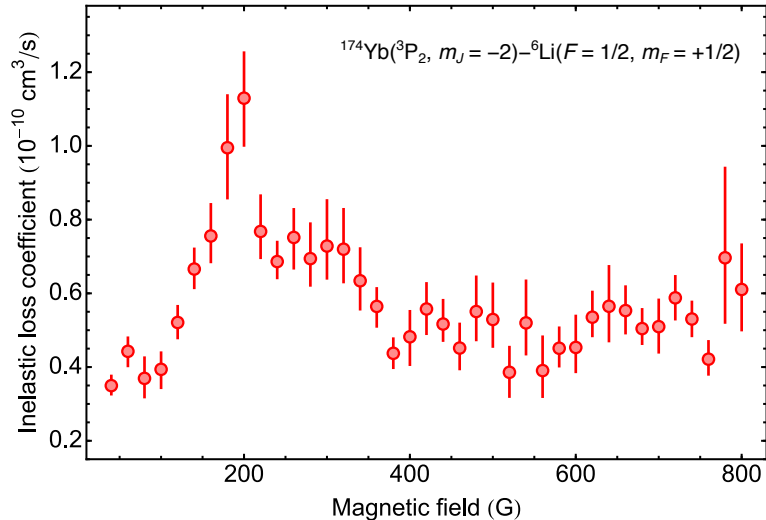


**Figure B.1.** Inelastic loss coefficients of the collisions in a  $^{174}\text{Yb}(^3\text{P}_2, m_J = -2)-^6\text{Li}(F = 1/2, m_F = +1/2)$  system for 40–800 G. A peak is observed at around 200 G. This probably indicates the existence of a Feshbach resonance. Though the location is consistent with the prediction in [34], the value of the loss coefficient is one order of magnitude smaller than the theoretical calculation. Also the measured coefficients for 400–800 G are almost constant, which does not match a resonance prediction at 750 G.

for  $B \leq 700$  G, and 11 ms for  $B \leq 800$  G. After various waiting times at the target magnetic field it is ramped down to 0 G in 2 ms. A second blast of ground state Yb atoms and repumping of the remaining excited Yb atoms are performed after the field ramp down. Yb atoms returned to the ground state and remaining Li atoms are finally detected by fluorescence and absorption imaging, respectively. Inelastic loss coefficients are evaluated by the method presented in this work.

So far we have measured inelastic loss coefficients of all combinations of  $\text{Yb}(^3\text{P}_2, m_J = -2, -1, 0)$  and all accessible spin states of Li for 40–800 G. Variations of the inelastic loss coefficients are observed in several combinations. In Fig. B.1 the result of the  $\text{Yb}(^3\text{P}_2, m_J = -2)-\text{Li}(F = 1/2, m_F = +1/2)$  system is shown. A peak-like feature is observed at 200 G. This would possibly indicate the existence of a Feshbach resonance there. This result is partially consistent with the theoretical calculation in [34], in which they predict a resonance at 200 G. However, the maximum value of the experimentally obtained loss coefficients is one order of magnitude smaller than the prediction. Also they predict a large resonance at 700 G whereas our result shows a flat spectrum for 400–800 G.

We do not assert that their calculation is wrong, because we think that the inelastic loss measurements at high fields still have some problems. The major problem is the long

magnetic-field ramp time. As seen in Section 6.2, typical decay times of the Yb( $^3P_2$ )-Li collisions is  $\lesssim 10$  ms. The field ramp time is comparable to the interaction time which might cause us to miscalculate loss coefficient values. Further investigations and checks of reproducibility of the measurements are necessary.

## B.2 Spectroscopy at high magnetic fields

In order to measure possible changes of the Yb-Li scattering length, we perform spectroscopy of Yb atoms around the magnetic field where an increase of the inelastic loss coefficient is observed. Different from the inelastic loss measurements the magnetic field is ramped to the desired value before excitation. Immediately after excitation and a blast pulse is applied, the excited atoms are repumped and detected by fluorescence imaging. We take spectra of the  $n = 1$  Mott shell in the presence and absence of Li and evaluate the shift of the resonance frequency.

We deal with the  $m_J = 0$  state of the  $^3P_2$  state for now because its resonance frequency is insensitive to the magnetic field. This also helps to do the blast and repump after the excitation at high fields, which results in reducing unwanted Yb( $^3P_2$ )-Li interaction time during which Yb atoms are lost due to their inelastic collisions. The applied magnetic field is oriented to the direction of gravity because of the configuration of the Feshbach coils. Therefore the obtained spectra are broadened due to the inhomogeneity of the optical traps compared to Fig. 6.2 taken at low fields where we can choose the field orientation to minimize inhomogeneous broadening.

Figure B.2 shows the result of the Yb( $^3P_2, m_J = 0$ )-Li( $F = 3/2, m_F = -3/2$ ) collisions. Since an increase of the inelastic loss coefficient is observed at around 750 G (Fig. B.2(a)), we take spectra for 650–810 G. Figure B.2(b) presents a spectrum in the absence and presence of Li at 750 G. The peak intensity for the case with Li is lower than for the case without Li. This is because in the presence of Li, a part of excited Yb atoms is lost during the excitation and blast time for 1.3 ms in total. We fit the obtained spectrum by a Gaussian function and evaluate the center resonance frequency.

Frequency shifts of the case with Li with respect to the case without Li at different magnetic fields are plotted in Fig. B.2(c). Positive shifts mean  $a_{e-Li} - a_{g-Li} > 0$  and negative shifts mean  $a_{e-Li} - a_{g-Li} < 0$ , where  $a_{g-Li}$  and  $a_{e-Li}$  represent the inter-species scattering length for ground and excited state Yb, respectively. Generally the resonance frequency tends to shift to the positive side in the presence of Li. This implies that the background scattering length is  $a_{e-Li} - a_{g-Li} > 0$ . If a Feshbach resonance is present,

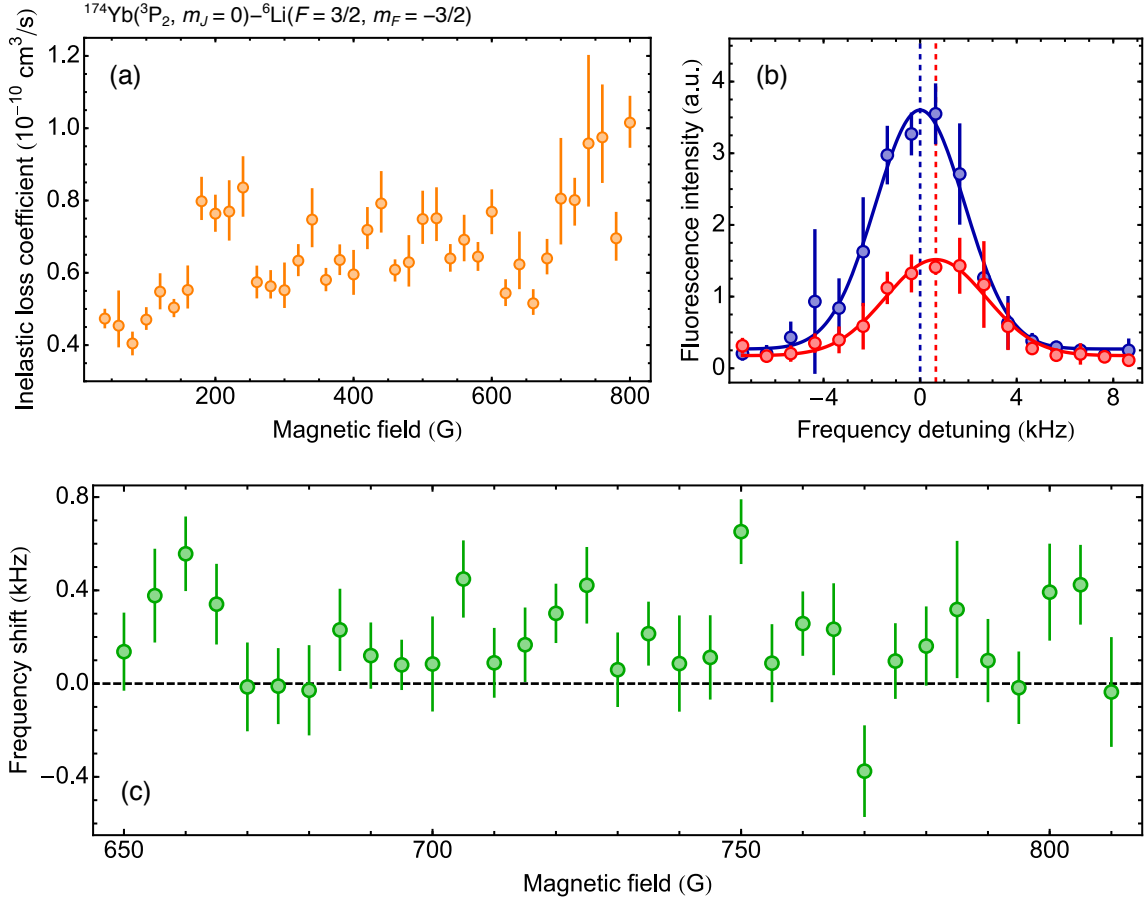


**Figure B.2.** Collisional properties of  $^{174}\text{Yb}(^3\text{P}_2, m_J = 0)$  and  $^6\text{Li}(F = 3/2, m_F = -3/2)$ . (a) Inelastic loss coefficients for 40–800 G. An increase of the inelastic loss coefficient is observed around 750 G. (b)  $^3\text{P}_2$  excitation spectrum of Yb in an  $n = 1$  Mott shell at 750 G with (red) and without (blue) Li. The solid lines are fits to the data by a Gaussian function. The dashed lines indicate their respective center frequencies. (c) Resonance frequency shifts of the data with Li with respect to the resonance without Li for 650–810 G. A diverging feature which is an evidence of a Feshbach resonance is not observed. Generally the resonance frequencies with Li shift to the positive side from those without Li. This implies that the background scattering length of the excited Yb and Li is positive.

we would expect that the resonance frequency shift diverges at the Feshbach resonance position. However such behavior is not observed at this resolution.

For a single Yb atom confined in a single lattice site, the inter-species interaction  $U_{\text{Yb-Li}}$  is given by

$$U_{\text{Yb-Li}} = \frac{2\pi\hbar^2 a_{\text{Yb-Li}}}{m_{\text{red}}} \int_{-d/2}^{d/2} |w_{\text{Yb}}(\mathbf{r})|^2 |\psi_{\text{Li}}(\mathbf{r})|^2 n_{\text{Li}}(\mathbf{r}) d^3\mathbf{r}, \quad (\text{B.1})$$

where  $a_{\text{Yb-Li}}$  is the Yb–Li scattering length,  $m_{\text{red}} = m_{\text{Yb}}m_{\text{Li}}/(m_{\text{Yb}} + m_{\text{Li}})$  is the reduced

mass,  $w_{\text{Yb}}$  and  $\psi_{\text{Li}}$  are the Yb Wannier and Li Bloch wave functions, and  $n_{\text{Li}}$  is the Li density. Since the integration range is within a single lattice site with  $d$  as the lattice spacing, the Li density can be regarded as constant. Thus Eq. (B.1) is written as

$$U_{\text{Yb-Li}} = \frac{2\pi\hbar^2 a_{\text{Yb-Li}}}{m_{\text{red}}} \xi n_{\text{Li}}, \quad (\text{B.2})$$

with  $\xi$  as defined as Eq. (6.5). The observed spectral shift corresponds to  $(U_{\text{e-Li}} - U_{\text{g-Li}})/h$ . Therefore a +0.5 kHz shift together with our Li density corresponds to  $a_{\text{e-Li}} - a_{\text{g-Li}} \approx 20$  nm.



## Bibliography

- [1] J. Kondo, “Resistance Minimum in Dilute Magnetic Alloys,” *Progress of Theoretical Physics* **32**, 37 (1964).
- [2] P. W. Anderson, “Absence of Diffusion in Certain Random Lattices,” *Physical Review* **109**, 1492 (1958).
- [3] P. W. Anderson, “Infrared Catastrophe in Fermi Gases with Local Scattering Potentials,” *Physical Review Letters* **18**, 1049 (1967).
- [4] R. P. Feynman, “Simulating physics with computers,” *International Journal of Theoretical Physics* **21**, 467 (1982).
- [5] I. Bloch, J. Dalibard, and W. Zwerger, “Many-body physics with ultracold gases,” *Reviews of Modern Physics* **80**, 885 (2008).
- [6] S. Giorgini, L. P. Pitaevskii, and S. Stringari, “Theory of ultracold atomic Fermi gases,” *Reviews of Modern Physics* **80**, 1215 (2008).
- [7] T. Esslinger, “Fermi-Hubbard Physics with Atoms in an Optical Lattice,” *Annual Review of Condensed Matter Physics* **1**, 129 (2010).
- [8] I. Bloch, J. Dalibard, and S. Nascimbène, “Quantum simulations with ultracold quantum gases,” *Nature Physics* **8**, 267 (2012).
- [9] C. Chin, R. Grimm, P. Julienne, and E. Tiesinga, “Feshbach resonances in ultracold gases,” *Reviews of Modern Physics* **82**, 1225 (2010).
- [10] C. A. Regal, M. Greiner, and D. S. Jin, “Observation of Resonance Condensation of Fermionic Atom Pairs,” *Physical Review Letters* **92**, 040403 (2004).
- [11] M. W. Zwierlein, C. A. Stan, C. H. Schunck, S. M. F. Raupach, A. J. Kerman, and W. Ketterle, “Condensation of Pairs of Fermionic Atoms near a Feshbach Resonance,” *Physical Review Letters* **92**, 120403 (2004).

## BIBLIOGRAPHY

---

- [12] M. W. Zwierlein, J. R. Abo-Shaeer, A. Schirotzek, C. H. Schunck, and W. Ketterle, “Vortices and superfluidity in a strongly interacting Fermi gas,” *Nature* **435**, 1047 (2005).
- [13] C. Becker, P. Soltan-Panahi, J. Kronjäger, S. Dörscher, K. Bongs, and K. Sengstock, “Ultracold quantum gases in triangular optical lattices,” *New Journal of Physics* **12**, 065025 (2010).
- [14] L. Tarruell, D. Greif, T. Uehlinger, G. Jotzu, and T. Esslinger, “Creating, moving and merging Dirac points with a Fermi gas in a tunable honeycomb lattice,” *Nature* **483**, 302 (2012).
- [15] S. Taie, H. Ozawa, T. Ichinose, T. Nishio, S. Nakajima, and Y. Takahashi, “Coherent driving and freezing of bosonic matter wave in an optical Lieb lattice,” *Science Advances* **1**, e1500854 (2015).
- [16] M. Greiner, O. Mandel, T. Esslinger, T. W. Hänsch, and I. Bloch, “Quantum phase transition from a superfluid to a Mott insulator in a gas of ultracold atoms,” *Nature* **415**, 39 (2002).
- [17] D. Jaksch and P. Zoller, “The cold atom Hubbard toolbox,” *Annals of Physics* **315**, 52 (2005).
- [18] L. Fallani, J. E. Lye, V. Guarrera, C. Fort, and M. Inguscio, “Ultracold Atoms in a Disordered Crystal of Light: Towards a Bose Glass,” *Physical Review Letters* **98**, 130404 (2007).
- [19] G. Roati, C. D’Errico, L. Fallani, M. Fattori, C. Fort, M. Zaccanti, G. Modugno, M. Modugno, and M. Inguscio, “Anderson localization of a non-interacting Bose–Einstein condensate,” *Nature* **453**, 895 (2008).
- [20] J. Billy, V. Josse, Z. Zuo, A. Bernard, B. Hambrecht, P. Lugan, D. Clément, L. Sanchez-Palencia, P. Bouyer, and A. Aspect, “Direct observation of Anderson localization of matter waves in a controlled disorder,” *Nature* **453**, 891 (2008).
- [21] S. S. Kondov, W. R. McGehee, J. J. Zirbel, and B. DeMarco, “Three-Dimensional Anderson Localization of Ultracold Matter,” *Science* **334**, 66 (2011).
- [22] K. Günter, T. Stöferle, H. Moritz, M. Köhl, and T. Esslinger, “Bose-Fermi Mixtures in a Three-Dimensional Optical Lattice,” *Physical Review Letters* **96**, 180402 (2006).

- 
- [23] S. Ospelkaus, C. Ospelkaus, O. Wille, M. Succo, P. Ernst, K. Sengstock, and K. Bongs, “Localization of Bosonic Atoms by Fermionic Impurities in a Three-Dimensional Optical Lattice,” *Physical Review Letters* **96**, 180403 (2006).
- [24] B. Gadway, D. Pertot, J. Reeves, M. Vogt, and D. Schneble, “Glassy Behavior in a Binary Atomic Mixture,” *Physical Review Letters* **107**, 145306 (2011).
- [25] R. Scelle, T. Rentrop, A. Trautmann, T. Schuster, and M. K. Oberthaler, “Motional Coherence of Fermions Immersed in a Bose Gas,” *Physical Review Letters* **111**, 070401 (2013).
- [26] D. Chen, C. Meldgin, and B. DeMarco, “Bath-induced band decay of a Hubbard lattice gas,” *Physical Review A* **90**, 013602 (2014).
- [27] D. Semmler, K. Byczuk, and W. Hofstetter, “Mott-Hubbard and Anderson metal-insulator transitions in correlated lattice fermions with binary disorder,” *Physical Review B* **81**, 115111 (2010).
- [28] D. A. Brue and J. M. Hutson, “Magnetically Tunable Feshbach Resonances in Ultracold Li-Yb Mixtures,” *Physical Review Letters* **108**, 043201 (2012).
- [29] S. Kato, S. Sugawa, K. Shibata, R. Yamamoto, and Y. Takahashi, “Control of Resonant Interaction between Electronic Ground and Excited States,” *Physical Review Letters* **110**, 173201 (2013).
- [30] S. Taie, S. Watanabe, T. Ichinose, and Y. Takahashi, “Feshbach-Resonance-Enhanced Coherent Atom-Molecule Conversion with Ultranarrow Photoassociation Resonance,” *Physical Review Letters* **116**, 043202 (2016).
- [31] S. Kotochigova, “Controlling interactions between highly magnetic atoms with Feshbach resonances,” *Reports on Progress in Physics* **77**, 093901 (2014).
- [32] M. Knap, A. Shashi, Y. Nishida, A. Imambekov, D. A. Abanin, and E. Demler, “Time-Dependent Impurity in Ultracold Fermions: Orthogonality Catastrophe and Beyond,” *Physical Review X* **2**, 041020 (2012).
- [33] K. Ohtaka and Y. Tanabe, “Theory of the soft-x-ray edge problem in simple metals: historical survey and recent developments,” *Reviews of Modern Physics* **62**, 929 (1990).

## BIBLIOGRAPHY

---

- [34] M. L. González-Martínez and J. M. Hutson, “Magnetically tunable Feshbach resonances in  $\text{Li} + \text{Yb}(^3P_J)$ ,” *Physical Review A* **88**, 020701 (2013).
- [35] T. Chen, C. Zhang, X. Li, J. Qian, and Y. Wang, “Anisotropy induced Feshbach resonances in mixture of  $^6\text{Li}(^2S) + ^{171}\text{Yb}(^3P_2)$ ,” *New Journal of Physics* **17**, 103036 (2015).
- [36] A. Khramov, A. Hansen, W. Dowd, R. J. Roy, C. Makrides, A. Petrov, S. Kotochigova, and S. Gupta, “Ultracold Heteronuclear Mixture of Ground and Excited State Atoms,” *Physical Review Letters* **112**, 033201 (2014).
- [37] W. Dowd, R. J. Roy, R. K. Shrestha, A. Petrov, C. Makrides, S. Kotochigova, and S. Gupta, “Magnetic field dependent interactions in an ultracold  $\text{Li}-\text{Yb}(^3P_2)$  mixture,” *New Journal of Physics* **17**, 055007 (2015).
- [38] A. Petrov, C. Makrides, and S. Kotochigova, “Magnetic control of ultra-cold  $^6\text{Li}$  and  $^{174}\text{Yb}(^3P_2)$  atom mixtures with Feshbach resonances,” *New Journal of Physics* **17**, 045010 (2015).
- [39] W. Ketterle, D. S. Durfee, and D. M. Stamper-kurn, , “Making, probing and understanding Bose-Einstein condensates,” Proceedings of the International School of Physics “Enrico Fermi,” Course CXL, 67, *IOP Press* (1999).
- [40] C. J. Pethick and H. Smith, “Bose–Einstein Condensation in Dilute Gases,” *Cambridge University Press* (2001).
- [41] D. A. Butts and D. S. Rokhsar, “Trapped Fermi gases,” *Physical Review A* **55**, 4346 (1997).
- [42] B. DeMarco, “Quantum Behavior of an Atomic Fermi Gas,” Ph.D. thesis, University of Colorado (2001).
- [43] W. Ketterle and M. W. Zwierlein, , “Making, probing and understanding ultracold Fermi gases,” Proceedings of the International School of Physics “Enrico Fermi,” Course CLXIV, 95, *IOP Press* (2008).
- [44] W. Zwerger, “Mott-Hubbard transition of cold atoms in optical lattices,” *Journal of Optics B: Quantum and Semiclassical Optics* **5**, S9 (2003).

- [45] F. Gerbier, A. Widera, S. Fölling, O. Mandel, T. Gericke, and I. Bloch, “Interference pattern and visibility of a Mott insulator,” *Physical Review A* **72**, 053606 (2005).
- [46] B. Capogrosso-Sansone, N. V. Prokof’ev, and B. V. Svistunov, “Phase diagram and thermodynamics of the three-dimensional Bose-Hubbard model,” *Physical Review B* **75**, 134302 (2007).
- [47] B. DeMarco, C. Lannert, S. Vishveshwara, and T.-C. Wei, “Structure and stability of Mott-insulator shells of bosons trapped in an optical lattice,” *Physical Review A* **71**, 063601 (2005).
- [48] S. Fölling, A. Widera, T. Müller, F. Gerbier, and I. Bloch, “Formation of Spatial Shell Structure in the Superfluid to Mott Insulator Transition,” *Physical Review Letters* **97**, 060403 (2006).
- [49] T. Köhler, K. Góral, and P. S. Julienne, “Production of cold molecules via magnetically tunable Feshbach resonances,” *Reviews of Modern Physics* **78**, 1311 (2006).
- [50] J. L. Bohn and P. S. Julienne, “Prospects for influencing scattering lengths with far-off-resonant light,” *Physical Review A* **56**, 1486 (1997).
- [51] N. Balakrishnan, V. Kharchenko, R. C. Forrey, and A. Dalgarno, “Complex scattering lengths in multi-channel atom–molecule collisions,” *Chemical Physics Letters* **280**, 5 (1997).
- [52] J. M. Hutson, “Feshbach resonances in ultracold atomic and molecular collisions: threshold behaviour and suppression of poles in scattering lengths,” *New Journal of Physics* **9**, 152 (2007).
- [53] M. H. Anderson, J. R. Ensher, M. R. Matthews, C. E. Wieman, and E. A. Cornell, “Observation of Bose-Einstein Condensation in a Dilute Atomic Vapor,” *Science* **269**, 198 (1995).
- [54] C. C. Bradley, C. A. Sackett, J. J. Tollett, and R. G. Hulet, “Evidence of Bose-Einstein Condensation in an Atomic Gas with Attractive Interactions,” *Physical Review Letters* **75**, 1687 (1995).
- [55] A. G. Truscott, K. E. Strecker, W. I. McAlexander, G. B. Partridge, and R. G. Hulet, “Observation of Fermi Pressure in a Gas of Trapped Atoms,” *Science* **291**, 2570 (2001).

## BIBLIOGRAPHY

---

- [56] S. Jochim, M. Bartenstein, A. Altmeyer, G. Hendl, S. Riedl, C. Chin, J. H. Denschlag, and R. Grimm, “Bose-Einstein Condensation of Molecules,” *Science* **302**, 2101 (2003).
- [57] M. Horikoshi, S. Nakajima, M. Ueda, and T. Mukaiyama, “Measurement of Universal Thermodynamic Functions for a Unitary Fermi Gas,” *Science* **327**, 442 (2010).
- [58] S. Nascimbène, N. Navon, K. J. Jiang, F. Chevy, and C. Salomon, “Exploring the thermodynamics of a universal Fermi gas,” *Nature* **463**, 1057 (2010).
- [59] M. J. H. Ku, A. T. Sommer, L. W. Cheuk, and M. W. Zwierlein, “Revealing the Superfluid Lambda Transition in the Universal Thermodynamics of a Unitary Fermi Gas,” *Science* **335**, 563 (2012).
- [60] I. Ferrier-Barbut, M. Delehaye, S. Laurent, A. T. Grier, M. Pierce, B. S. Rem, F. Chevy, and C. Salomon, “A mixture of Bose and Fermi superfluids,” *Science* **345**, 1035 (2014).
- [61] R. A. Hart, P. M. Duarte, T.-L. Yang, X. Liu, T. Paiva, E. Khatami, R. T. Scalettar, N. Trivedi, D. A. Huse, and R. G. Hulet, “Observation of antiferromagnetic correlations in the Hubbard model with ultracold atoms,” *Nature* **519**, 211 (2015).
- [62] A. Mazurenko, C. S. Chiu, G. Ji, M. F. Parsons, M. Kanász-Nagy, R. Schmidt, F. Grusdt, E. Demler, D. Greif, and M. Greiner, “Experimental realization of long-range antiferromagnet in the Hubbard model with ultracold atoms,” arXiv:1612.08436 (2016).
- [63] M. F. Parsons, F. Huber, A. Mazurenko, C. S. Chiu, W. Setiawan, K. Wooley-Brown, S. Blatt, and M. Greiner, “Site-Resolved Imaging of Fermionic  ${}^6\text{Li}$  in an Optical Lattice,” *Physical Review Letters* **114**, 213002 (2015).
- [64] A. Omran, M. Boll, T. A. Hilker, K. Kleinlein, G. Salomon, I. Bloch, and C. Gross, “Microscopic Observation of Pauli Blocking in Degenerate Fermionic Lattice Gases,” *Physical Review Letters* **115**, 263001 (2015).
- [65] C. J. Foot, “Atomic Physics,” *Oxford University Press* (2005).
- [66] C. J. Sansonetti, C. E. Simien, J. D. Gillaspay, J. N. Tan, S. M. Brewer, R. C. Brown, S. Wu, and J. V. Porto, “Absolute Transition Frequencies and Quantum

- Interference in a Frequency Comb Based Measurement of the  $^{6,7}\text{Li}$   $D$  Lines,” *Physical Review Letters* **107**, 023001 (2011).
- [67] W. I. McAlexander, E. R. I. Abraham, and R. G. Hulet, “Radiative lifetime of the  $2P$  state of lithium,” *Physical Review A* **54**, R5–R8 (1996).
- [68] E. Arimondo, M. Inguscio, and P. Violino, “Experimental determinations of the hyperfine structure in the alkali atoms,” *Reviews of Modern Physics* **49**, 31 (1977).
- [69] G. Zürn, T. Lompe, A. N. Wenz, S. Jochim, P. S. Julienne, and J. M. Hutson, “Precise Characterization of  $^6\text{Li}$  Feshbach Resonances Using Trap-Sideband-Resolved RF Spectroscopy of Weakly Bound Molecules,” *Physical Review Letters* **110**, 135301 (2013).
- [70] K. E. Strecker, G. B. Partridge, and R. G. Hulet, “Conversion of an Atomic Fermi Gas to a Long-Lived Molecular Bose Gas,” *Physical Review Letters* **91**, 080406 (2003).
- [71] Y. Takasu, K. Maki, K. Komori, T. Takano, K. Honda, M. Kumakura, T. Yabuzaki, and Y. Takahashi, “Spin-Singlet Bose-Einstein Condensation of Two-Electron Atoms,” *Physical Review Letters* **91**, 040404 (2003).
- [72] T. Fukuhara, Y. Takasu, M. Kumakura, and Y. Takahashi, “Degenerate Fermi Gases of Ytterbium,” *Physical Review Letters* **98**, 030401 (2007).
- [73] T. Fukuhara, S. Sugawa, and Y. Takahashi, “Bose-Einstein condensation of an ytterbium isotope,” *Physical Review A* **76**, 051604 (2007).
- [74] T. Fukuhara, S. Sugawa, Y. Takasu, and Y. Takahashi, “All-optical formation of quantum degenerate mixtures,” *Physical Review A* **79**, 021601 (2009).
- [75] S. Sugawa, R. Yamazaki, S. Taie, and Y. Takahashi, “Bose-Einstein condensate in gases of rare atomic species,” *Physical Review A* **84**, 011610 (2011).
- [76] S. Taie, Y. Takasu, S. Sugawa, R. Yamazaki, T. Tsujimoto, R. Murakami, and Y. Takahashi, “Realization of a  $\text{SU}(2)\times\text{SU}(6)$  System of Fermions in a Cold Atomic Gas,” *Physical Review Letters* **105**, 190401 (2010).
- [77] S. Sugawa, K. Inaba, S. Taie, R. Yamazaki, M. Yamashita, and Y. Takahashi, “Interaction and filling-induced quantum phases of dual Mott insulators of bosons and fermions,” *Nature Physics* **7**, 642 (2011).

## BIBLIOGRAPHY

---

- [78] S. Kato, K. Inaba, S. Sugawa, K. Shibata, R. Yamamoto, M. Yamashita, and Y. Takahashi, “Laser spectroscopic probing of coexisting superfluid and insulating states of an atomic Bose–Hubbard system,” *Nature Communications* **7**, 11341 (2016).
- [79] F. Scazza, C. Hofrichter, M. Höfer, P. C. De Groot, I. Bloch, and S. Fölling, “Observation of two-orbital spin-exchange interactions with ultracold  $SU(N)$ -symmetric fermions,” *Nature Physics* **10**, 779 (2014).
- [80] R. Zhang, Y. Cheng, H. Zhai, and P. Zhang, “Orbital Feshbach Resonance in Alkali-Earth Atoms,” *Physical Review Letters* **115**, 135301 (2015).
- [81] G. Pagano, M. Mancini, G. Cappellini, L. Livi, C. Sias, J. Catani, M. Inguscio, and L. Fallani, “Strongly Interacting Gas of Two-Electron Fermions at an Orbital Feshbach Resonance,” *Physical Review Letters* **115**, 265301 (2015).
- [82] M. Höfer, L. Riegger, F. Scazza, C. Hofrichter, D. R. Fernandes, M. M. Parish, J. Levinsen, I. Bloch, and S. Fölling, “Observation of an Orbital Interaction-Induced Feshbach Resonance in  $^{173}\text{Yb}$ ,” *Physical Review Letters* **115**, 265302 (2015).
- [83] D. Das, S. Barthwal, A. Banerjee, and V. Natarajan, “Absolute frequency measurements in Yb with 0.08 ppb uncertainty: Isotope shifts and hyperfine structure in the 399-nm  $^1S_0 \rightarrow ^1P_1$  line,” *Physical Review A* **72**, 032506 (2005).
- [84] K. Pandey, A. K. Singh, P. V. K. Kumar, M. V. Suryanarayana, and V. Natarajan, “Isotope shifts and hyperfine structure in the 555.8-nm  $^1S_0 \rightarrow ^3P_1$  line of Yb,” *Physical Review A* **80**, 022518 (2009).
- [85] C. W. Hoyt, Z. W. Barber, C. W. Oates, T. M. Fortier, S. A. Diddams, and L. Hollberg, “Observation and Absolute Frequency Measurements of the  $^1S_0$ - $^3P_0$  Optical Clock Transition in Neutral Ytterbium,” *Physical Review Letters* **95**, 083003 (2005).
- [86] A. Yamaguchi, S. Uetake, S. Kato, H. Ito, and Y. Takahashi, “High-resolution laser spectroscopy of a Bose–Einstein condensate using the ultranarrow magnetic quadrupole transition,” *New Journal of Physics* **12**, 103001 (2010).
- [87] M. Kitagawa, K. Enomoto, K. Kasa, Y. Takahashi, R. Ciuryło, P. Naidon, and P. S. Julienne, “Two-color photoassociation spectroscopy of ytterbium atoms and

- the precise determinations of  $s$ -wave scattering lengths,” *Physical Review A* **77**, 012719 (2008).
- [88] R. Ciuryło, E. Tiesinga, and P. S. Julienne, “Optical tuning of the scattering length of cold alkaline-earth-metal atoms,” *Physical Review A* **71**, 030701 (2005).
- [89] K. Enomoto, K. Kasa, M. Kitagawa, and Y. Takahashi, “Optical Feshbach Resonance Using the Intercombination Transition,” *Physical Review Letters* **101**, 203201 (2008).
- [90] R. Yamazaki, S. Taie, S. Sugawa, and Y. Takahashi, “Submicron Spatial Modulation of an Interatomic Interaction in a Bose-Einstein Condensate,” *Physical Review Letters* **105**, 050405 (2010).
- [91] R. Yamazaki, S. Taie, S. Sugawa, K. Enomoto, and Y. Takahashi, “Observation of a  $p$ -wave optical Feshbach resonance,” *Physical Review A* **87**, 010704 (2013).
- [92] A. Yamaguchi, S. Uetake, D. Hashimoto, J. M. Doyle, and Y. Takahashi, “Inelastic Collisions in Optically Trapped Ultracold Metastable Ytterbium,” *Physical Review Letters* **101**, 233002 (2008).
- [93] S. Uetake, R. Murakami, J. M. Doyle, and Y. Takahashi, “Spin-dependent collision of ultracold metastable atoms,” *Physical Review A* **86**, 032712 (2012).
- [94] K. Aikawa, A. Frisch, M. Mark, S. Baier, A. Rietzler, R. Grimm, and F. Ferlaino, “Bose-Einstein Condensation of Erbium,” *Physical Review Letters* **108**, 210401 (2012).
- [95] A. Frisch, M. Mark, K. Aikawa, F. Ferlaino, J. L. Bohn, C. Makrides, A. Petrov, and S. Kotochigova, “Quantum chaos in ultracold collisions of gas-phase erbium atoms,” *Nature* **507**, 475 (2014).
- [96] K. Baumann, N. Q. Burdick, M. Lu, and B. L. Lev, “Observation of low-field Fano-Feshbach resonances in ultracold gases of dysprosium,” *Physical Review A* **89**, 020701 (2014).
- [97] H. Hara, Y. Takasu, Y. Yamaoka, J. M. Doyle, and Y. Takahashi, “Quantum Degenerate Mixtures of Alkali and Alkaline-Earth-Like Atoms,” *Physical Review Letters* **106**, 205304 (2011).

## BIBLIOGRAPHY

---

- [98] R. Roy, A. Green, R. Bowler, and S. Gupta, “Two-Element Mixture of Bose and Fermi Superfluids,” arXiv:1607.03221 (2016).
- [99] M. Okano, “Simultaneous Magneto-Optical Trapping of Lithium and Ytterbium Atoms: Towards Production of Ultracold Polar Molecules,” Ph.D. thesis, Kyoto University (2009).
- [100] H. Hara, “Production of Quantum Degenerate Mixtures of Alkali and Alkaline-Earth-Like Atoms,” Ph.D. thesis, Kyoto University (2013).
- [101] A. H. Hansen, A. Y. Khramov, W. H. Dowd, A. O. Jamison, B. Plotkin-Swing, R. J. Roy, and S. Gupta, “Production of quantum-degenerate mixtures of ytterbium and lithium with controllable interspecies overlap,” *Physical Review A* **87**, 013615 (2013).
- [102] M. Okano, H. Hara, M. Muramatsu, K. Doi, S. Uetake, Y. Takasu, and Y. Takahashi, “Simultaneous magneto-optical trapping of lithium and ytterbium atoms towards production of ultracold polar molecules,” *Applied Physics B* **98**, 691 (2010).
- [103] C. A. Stan and W. Ketterle, “Multiple species atom source for laser-cooling experiments,” *Review of Scientific Instruments* **76**, 063113 (2005).
- [104] E. D. Black, “An introduction to Pound–Drever–Hall laser frequency stabilization,” *American Journal of Physics* **69**, 79 (2001).
- [105] T. W. Hänsch and B. Couillaud, “Laser frequency stabilization by polarization spectroscopy of a reflecting reference cavity,” *Optics Communications* **35**, 441 (1980).
- [106] S. Uetake, A. Yamaguchi, S. Kato, and Y. Takahashi, “High power narrow linewidth laser at 556 nm for magneto-optical trapping of ytterbium,” *Applied Physics B* **92**, 33 (2008).
- [107] H. Hara, H. Konishi, S. Nakajima, Y. Takasu, and Y. Takahashi, “A Three-Dimensional Optical Lattice of Ytterbium and Lithium Atomic Gas Mixture,” *Journal of the Physical Society of Japan* **83**, 014003 (2014).
- [108] T. Fukuhara, S. Sugawa, M. Sugimoto, S. Taie, and Y. Takahashi, “Mott insulator of ultracold alkaline-earth-metal-like atoms,” *Physical Review A* **79**, 041604 (2009).

- [109] J. H. Denschlag, J. E. Simsarian, H. Häffner, C. McKenzie, A. Browaeys, D. Cho, K. Helmerson, S. L. Rolston, and W. D. Phillips, “A Bose-Einstein condensate in an optical lattice,” *Journal of Physics B: Atomic, Molecular and Optical Physics* **35**, 3095 (2002).
- [110] S. Kato, “High-resolution laser spectroscopy of quantum degenerate Ytterbium atoms in an optical lattice,” Ph.D. thesis, Kyoto University (2012).
- [111] L. Ricci, M. Weidemüller, T. Esslinger, A. Hemmerich, C. Zimmermann, V. Vuletic, W. König, and T. W. Hänsch, “A compact grating-stabilized diode laser system for atomic physics,” *Optics Communications* **117**, 541 (1995).
- [112] K. G. Libbrecht and J. L. Hall, “A low-noise high-speed diode laser current controller,” *Review of Scientific Instruments* **64**, 2133 (1993).
- [113] P. D. Lett, W. D. Phillips, S. L. Rolston, C. E. Tanner, R. N. Watts, and C. I. Westbrook, “Optical molasses,” *Journal of the Optical Society of America B* **6**, 2084 (1989).
- [114] R. Grimm, M. Weidemüller, and Y. B. Ovchinnikov, “Optical dipole traps for neutral atoms,” *Advances in Atomic, Molecular, and Optical Physics* **42**, 95 (2000).
- [115] M. Houbiers, H. T. C. Stoof, W. I. McAlexander, and R. G. Hulet, “Elastic and inelastic collisions of  ${}^6\text{Li}$  atoms in magnetic and optical traps,” *Physical Review A* **57**, R1497 (1998).
- [116] S. Ospelkaus-Schwarzer, “Quantum Degenerate Fermi-Bose Mixtures of  ${}^{40}\text{K}$  and  ${}^{87}\text{Rb}$  in 3D Optical Lattices,” Ph.D. thesis, University of Hamburg (2006).
- [117] M. Repp, “Interspecies Feshbach Resonances in an Ultracold, Optically Trapped Bose-Fermi Mixture of Cesium and Lithium,” Ph.D. thesis, University of Heidelberg (2013).
- [118] F. Gerbier, A. Widera, S. Fölling, O. Mandel, T. Gericke, and I. Bloch, “Phase Coherence of an Atomic Mott Insulator,” *Physical Review Letters* **95**, 050404 (2005).
- [119] F. M. Spiegelhalder, A. Trenkwalder, D. Naik, G. Hendl, F. Schreck, and R. Grimm, “Collisional Stability of  ${}^{40}\text{K}$  Immersed in a Strongly Interacting Fermi Gas of  ${}^6\text{Li}$ ,” *Physical Review Letters* **103**, 223203 (2009).

## BIBLIOGRAPHY

---

- [120] H. Konishi, F. Schäfer, S. Ueda, and Y. Takahashi, “Collisional stability of localized  $\text{Yb}(^3\text{P}_2)$  atoms immersed in a Fermi sea of Li,” *New Journal of Physics* **18**, 103009 (2016).
- [121] F. Le Kien, P. Schneeweiss, and A. Rauschenbeutel, “Dynamical polarizability of atoms in arbitrary light fields: general theory and application to cesium,” *The European Physical Journal D* **67**, 92 (2013).
- [122] G. Refael and E. Demler, “Superfluid-insulator transition in Fermi-Bose mixtures and the orthogonality catastrophe,” *Physical Review B* **77**, 144511 (2008).
- [123] J. Goold, T. Fogarty, N. Lo Gullo, M. Paternostro, and T. Busch, “Orthogonality catastrophe as a consequence of qubit embedding in an ultracold Fermi gas,” *Physical Review A* **84**, 063632 (2011).
- [124] A. Sindona, J. Goold, N. Lo Gullo, S. Lorenzo, and F. Plastina, “Orthogonality Catastrophe and Decoherence in a Trapped-Fermion Environment,” *Physical Review Letters* **111**, 165303 (2013).
- [125] M. Cetina, M. Jag, R. S. Lous, J. T. M. Walraven, R. Grimm, R. S. Christensen, and G. M. Bruun, “Decoherence of Impurities in a Fermi Sea of Ultracold Atoms,” *Physical Review Letters* **115**, 135302 (2015).
- [126] M. Cetina, M. Jag, R. S. Lous, I. Fritsche, J. T. M. Walraven, R. Grimm, J. Levinson, M. M. Parish, R. Schmidt, M. Knap, and E. Demler, “Ultrafast many-body interferometry of impurities coupled to a Fermi sea,” *Science* **354**, 96 (2016).
- [127] E. Knill and R. Laflamme, “Power of One Bit of Quantum Information,” *Physical Review Letters* **81**, 5672 (1998).
- [128] Y. Nishida, “Phases of a bilayer Fermi gas,” *Physical Review A* **82**, 011605 (2010).
- [129] Y. Nishida and S. Tan, “Confinement-induced  $p$ -wave resonances from  $s$ -wave interactions,” *Physical Review A* **82**, 062713 (2010).
- [130] E. Malatsetxebarria, Z. Cai, U. Schollwöck, and M. A. Cazalilla, “Dissipative effects on the superfluid-to-insulator transition in mixed-dimensional optical lattices,” *Physical Review A* **88**, 063630 (2013).
- [131] E. Malatsetxebarria, F. M. Marchetti, and M. A. Cazalilla, “Phase equilibrium of binary mixtures in mixed dimensions,” *Physical Review A* **88**, 033604 (2013).

- [132] G. Lamporesi, J. Catani, G. Barontini, Y. Nishida, M. Inguscio, and F. Minardi, “Scattering in Mixed Dimensions with Ultracold Gases,” *Physical Review Letters* **104**, 153202 (2010).
- [133] E. Haller, M. J. Mark, R. Hart, J. G. Danzl, L. Reichsöllner, V. Melezhik, P. Schmelcher, and H.-C. Nägerl, “Confinement-Induced Resonances in Low-Dimensional Quantum Systems,” *Physical Review Letters* **104**, 153203 (2010).



## Acknowledgements

多くの方々のご協力の下、本論文をまとめあげることができました。ここで改めて皆様に感謝いたします。指導教官である高橋義朗教授には、修士課程入学時から6年間に渡りご指導頂きました。常に実験の細部に渡って非常に的確なアドバイスを頂いたおかげで、この博士論文を完成させることができました。ありがとうございました。

I would like to express my great gratitude to Dr. Florian Schäfer. We spent almost my entire doctoral years and all the works presented in this thesis were carried out with him. I cannot imagine the completion of this thesis without his considerable help. Danke schön!

実験に協力してくれた後輩達にも感謝します。植田信也君とは、光格子系の構築から非弾性衝突の測定まで、本研究の主要な部分を一緒に実験しました。植田君の協力によってここまでの成果を挙げることができました。また歴代のQ6で配属された4回生、足立景亮君、浅賀洋人君、佐藤浩司君、澤田あずきさん、小野滉貴君、八神智哉君、および留学生のAndreas Kell君は本研究のための新しい装置の作成や、データ取得などに協力してくれました。ありがとうございました。

本研究は修士の頃からの研究の発展です。修士時代の先輩方の指導が、現在の私の基礎となっています。高須洋介助教には長年の経験に基づいた有益なアドバイスを多く頂きました。中島秀太博士には実験の基礎から丁寧に指導頂きました。グループが変わった現在でも、冷却原子にとどまらない幅広い物理の知識で議論してくださり、大変勉強になっています。原秀明博士とは修士の頃の実験で最も多くの時間を共有しました。複雑な装置を丁寧に説明して頂いたおかげで、今ではそれを受け継いで実験を続けることができています。

その他の量子光学研究室のメンバーの皆さんにも、ミーティングや食事の際などに有意義な議論をして頂きました。皆さんの挙げる素晴らしい研究成果を間近で見ることができ、大変刺激を受けました。ありがとうございました。

最後にいつも温かく見守ってくれている家族に感謝いたします。

